

ABSTRACT

Title of Dissertation: DESIGN, FABRICATION, AND TESTING OF
A MICROSYSTEM FOR MONITORING
BACTERIAL QUORUM SENSING

Stephan Todorov Koev, Doctor of Philosophy,
2009

Directed By: Professor Reza Ghodssi, Department of
Electrical and Computer Engineering

Most pathogenic bacteria communicate with each other using signaling molecules. Their coordinated behavior, known as quorum sensing (QS), enables them to infect host organisms collectively and form drug-resistant biofilms. The study of bacterial signaling pathways may lead to discovery of new antimicrobials. Lab-on-a-chip technology can significantly accelerate the screening of candidate drugs that inhibit QS. This dissertation develops for the first time miniaturized sensors embedded in microfluidic channels to monitor the activity of an enzymatic pathway that produces signaling molecules. These devices can be used as building blocks of future high-throughput systems for drug discovery.

The sensors presented here are gold-coated microcantilevers, and they detect the aminoacid homocysteine, a byproduct of the bacterial signaling pathway. It binds to the gold surface, causing stress and cantilever displacement that is measured optically. Samples are synthesized using bacterial enzymes and tested with the

sensors. The minimal detected concentration of homocysteine is $1\mu\text{M}$. It is demonstrated that deactivation of the enzymes causes a change in the sensor response; this effect can be used for finding drugs that inhibit the enzyme.

The traditional method for measuring cantilever displacement requires an elaborate optical setup, and it can only test one device at a time. Two new methods are developed here to overcome these limitations. The first one uses a transparent cantilever which is also an optical waveguide. Light is coupled from the cantilever to a fixed output waveguide and measured with a photodetector. The cantilever displacement is determined from the change in output power. The change is approximately 0.7% per nanometer displacement. The minimal detectable displacement and surface stress are 6nm and 1.3 mN/m respectively.

The second measurement method uses a transparent cantilever that is close to a reflective substrate. When the device is imaged with an optical microscope, an interference pattern forms. The cantilever displacement is calculated from the lateral shift of the interference fringes. This shift is determined from images of the device using custom software. The response of multiple cantilevers is captured by translating the microscope stage. The minimal detectable displacement and surface stress are 1nm and 340 $\mu\text{N/m}$ respectively.

**DESIGN, FABRICATION, AND TESTING OF A MICROSYSTEM FOR
MONITORING BACTERIAL QUORUM SENSING**

By

Stephan Todorov Koev

Dissertation submitted to the Faculty of the Graduate School of the
University of Maryland, College Park, in partial fulfillment
of the requirements for the degree of
Doctor of Philosophy
2009

Advisory Committee:

Professor Reza Ghodssi, Chair
Professor William Bentley
Professor Christopher Davis
Professor Agis Iliadis
Professor Gary Rubloff

© Copyright by
Stephan Todorov Koev
2009

Dedication

To my parents, Irina and Todor, for their unconditional support.

Acknowledgments

First, I would like to thank my advisor Prof. Reza Ghodssi for his guidance and support over the past 5 years, as well as my Dissertation Committee: Prof. Christopher Davis, Prof. William Bentley, Prof. Agis Iliadis, and Prof. Gary Rubloff. I greatly appreciate the funding provided by the R.W. Deutsch Foundation, the Laboratory for Physical Sciences, and the National Science Foundation to make this research possible. Throughout the course of this work, I was fortunate to collaborate with many outstanding individuals. I am especially thankful to Prof. Gregory Payne, Dr. Hyunmin Yi, Dr. Rohan Fernandes, and Dr. Angela Lewandowski for their assistance with biology-related issues. Next, I would like to acknowledge my colleagues at the MEMS Sensors and Actuators Lab (MSAL), who have helped me in innumerable ways. Many thanks to Peter Dykstra, Nathan Siwak, and Mariana Meyer for reviewing this manuscript and to Jonathan McGee for insightful discussions. I greatly appreciate the professionalism of the cleanroom staff at both the University of Maryland Nanocenter and the Laboratory for Physical Sciences. Special thanks to Prof. James Ziegler and Prof. Samara Firebaugh at the US Naval Academy, who inspired me to pursue graduate school. Finally, I would like to thank my family and friends for providing relief when the going got tough.

Stephan Koev,

May 2009.

Table of Contents

Dedication.....	ii
Acknowledgments.....	iii
Table of Contents.....	iv
List of Tables	vi
List of Figures.....	vii
Chapter 1: Introduction.....	1
1.1 Background and Motivation	1
1.2 Summary of Accomplishments.....	3
1.2.1 Design and Fabrication of Waveguide Cantilever for Liquid Samples	3
1.2.2 Device and Method for Interferometric Displacement Measurements.	4
1.2.3 Detection of Enzymatically Produced Homocysteine	5
1.3 Literature Review.....	6
1.3.1 Bacterial Quorum Sensing.....	6
1.3.2 BioMEMS for Drug Discovery.....	11
1.3.3 BioMEMS Sensors.....	12
1.3.4 Microcantilever Sensors.....	15
1.4 Structure of Dissertation	24
Chapter 2: Theory of Operation and Design.....	25
2.1 Introduction.....	25
2.2 Waveguide Cantilever.....	25
2.2.1 Device Structure.....	25
2.2.2 Mechanical Sensitivity.....	28
2.2.3 Optical Sensitivity.....	31
2.2.4 Choice of Dimensions and Mask Layout.....	50
2.3 Interferometric Cantilever.....	51
2.3.1 Device Structure.....	51
2.3.2 Theory of Operation.....	53
2.3.3 Image Processing Algorithm.....	58
2.3.4 Measurement Error	59
2.3.5 Choice of Dimensions.....	62
2.4 Summary.....	63
Chapter 3: Fabrication.....	64
3.1 Introduction.....	64
3.2 Choice of Materials.....	64
3.3 Fabrication Process Flow	68
3.4 Optimization of Fabrication Process.....	73
3.5 Final Fabrication Parameters	83
3.6 Fabrication Results.....	85
3.7 Packaging.....	87
3.7.1 PDMS Layer Fabrication	87
3.7.2 Package Assembly	89
3.8 Summary.....	94

Chapter 4: Waveguide Cantilever Testing.....	95
4.1 Introduction.....	95
4.2 Experimental Setup.....	95
4.3 Optical Characterization.....	97
4.3.1 Loss Measurements.....	97
4.3.2 Power Drift.....	100
4.3.3 Optical Power vs. Tip Deflection.....	102
4.4 Detection of Homocysteine from Powder.....	104
4.4.1 Procedures.....	104
4.4.2 Detection Results.....	105
4.4.3 Interferometric Measurements.....	111
4.5 Detection of Enzymatically Produced Homocysteine.....	115
4.5.1 External Enzymatic Synthesis.....	115
4.5.2 Enzymatic Synthesis in Microfluidics.....	116
4.6 Discussion.....	120
4.7 Summary.....	123
Chapter 5: Interferometric Cantilever Testing.....	125
5.1 Introduction.....	125
5.2 Experimental Setup.....	125
5.3 Microscope Light Source.....	126
5.4 Measurement Precision.....	132
5.5 Response to pH Variation.....	134
5.6 Detection of Homocysteine from Powder.....	137
5.6.1 Procedures.....	138
5.6.2 Detection Results.....	139
5.7 Detection of Enzymatically Produced Homocysteine.....	142
5.7.1 Batch Reactor Samples.....	143
5.7.2 Flow Reactor Samples.....	143
5.7.3 Detection Results.....	144
5.8 Discussion.....	146
5.9 Summary.....	147
Chapter 6: Conclusion.....	149
6.1 Summary.....	149
6.1.1 Waveguide Cantilever.....	150
6.1.2 Interferometric Cantilever.....	150
6.1.3 Comparison of Devices.....	151
6.2 Future Work.....	152
6.2.1 Microfluidic System.....	152
6.2.2 Applications beyond Quorum Sensing.....	153
6.2.3 Integration of Optoelectronics.....	154
6.2.4 Interferometric Cantilever Arrays.....	156
6.2.5 Sensitivity Enhancement.....	158
6.3 Conclusion.....	159
Appendix A: MATLAB Script for Fringe Shift Measurement.....	161
References.....	163

List of Tables

Table 2.1: Definitions of variables.....	29
Table 2.2: Young’s modulus and thicknesses of cantilever materials in this work (other materials commonly used for cantilevers are given for comparison). These are representative values obtained from literature.....	29
Table 2.3: Dimensions of waveguide cantilever device. Parameters critical to the performance are listed in bold.....	51
Table 3.1: Fabrication process flow of waveguide cantilever. The device cross sections are given along the dashed line in the mask layout.....	70
Table 3.2: Fabrication process flow of interferometric cantilever. The device cross sections are given along the dashed line in the mask layout.....	71
Table 3.3: Contributions to curvature in metal coated SU-8 cantilevers.....	83
Table 3.4: Summary of final fabrication parameters. The corresponding process steps from Table 3.1 and Table 3.2 are specified. All bakes are performed on a hotplate. .	84
Table 3.5: SU-8 process parameters for mold wafer fabrication.	88
Table 4.1: Summary of results from homocysteine detection experiments and estimated surface stress.....	121
Table 5.1: Coherence characteristics of different light sources that can be used for microscope illumination. The coherence lengths are adjusted for the refractive index of water (1.33).....	128
Table 5.2: Average and standard deviation of 10 fringe shift measurements performed with and without microscope refocusing and stage motion.....	133
Table 5.3: Summary of results from homocysteine detection experiments performed with interferometric cantilever.....	146

List of Figures

Figure 1.1: Biosynthetic pathway of AI-2. Adapted from ref. [37].	9
Figure 1.2: Schematic of the “optical lever” readout. Reproduced from ref. [27].	17
Figure 1.3: Schematic of cantilever with integrated waveguide readout reported by Zinoviev <i>et al.</i> Reproduced from ref. [32].	19
Figure 1.4: SEM of cantilever with integrated waveguide readout reported by Pruessner <i>et al.</i> Reproduced from ref. [31].	20
Figure 1.5: Schematic of cantilever with integrated waveguide readout reported by Nordstrom <i>et al.</i> Reproduced from ref. [33].	21
Figure 1.6: Schematic (a) and micrographs (b, c) of microbridge resonators with on chip interference cavity. Reproduced from ref. [91].	23
Figure 2.1: Schematic (3D) of a waveguide cantilever before the addition of the microfluidic channel.	26
Figure 2.2: a) Cross section along waveguide cantilever embedded in microfluidic channel. b) Top down view of SU-8 layout. c) Top down view of fluid channel layout. The XYZ coordinate systems used for the mechanical and optical analysis later are shown.	27
Figure 2.3: Schematic of light coupling from cantilever into output waveguide across gap.	33
Figure 2.4: Graphical solutions of the transcendental equation for a planar waveguide for (a) TE and (b) TM modes.	34
Figure 2.5: Contour plot of the electric field x-component of the fundamental TE mode in a) the output waveguide and b) the cantilever tip. Red corresponds to high values and blue to low values.	37
Figure 2.6: Contour plot of the electric field x-component of the fundamental TE mode in the gold-covered part of the cantilever. Red corresponds to high values and blue to low values.	39
Figure 2.7: Vertical electric field distribution in a) cantilever tip and b) output waveguide.	40
Figure 2.8: Theoretical coupling coefficient as a function of cantilever displacement for a gap of 2 μm . a) Raw values b) Normalized.	43

Figure 2.9: Theoretical coupling coefficient as a function of cantilever displacement for a gap of 4 μm . a) Raw values b) Normalized.....	43
Figure 2.10: Schematic of light coupling from tilted cantilever into output waveguide.	44
Figure 2.11: Theoretical coupling coefficient for a cantilever length of 100 μm and propagation gap of a) 2 μm b) 4 μm	45
Figure 2.12: Theoretical coupling coefficient and sensitivity for a cantilever with 2 μm propagation gap (based on the Gaussian model without tilt).	48
Figure 2.13: Theoretical coupling coefficient, sensitivity, and ratio of the two for a cantilever with 2 μm propagation gap (based on the Gaussian model without tilt). ..	50
Figure 2.14: Schematic (3D) of an interferometric cantilever before the addition of the microfluidic channel. The layer thicknesses are labeled.....	52
Figure 2.15: a) Cross section of interferometric cantilever inside microfluidic channel. b) Top down view of SU-8 layout. c) Top down view of fluid channels layout. The same XYZ coordinate system is used as for the waveguide cantilever.	52
Figure 2.16: Interference cavity formed between transparent cantilever and reflective substrate.	53
Figure 2.17: Microscope image of an interferometric cantilever immersed in water.	54
Figure 2.18: Measured intensity profile from a cantilever image (solid line) and curve fit (dashed line). The fit has $R^2 = 0.94$	56
Figure 2.19: Geometry used for calculating cantilever displacement from horizontal fringe shift.....	57
Figure 2.20: Initial and final images of a cantilever displaced downward due to change in solution pH (imaged in liquid). The interference fringes move to the right. The regions of interest 1-4 are selected by the user with the mouse.	59
Figure 2.21: Estimated measurement error resulting from three different types of slope approximation.....	62
Figure 3.1: Side view micrograph of a stoichiometric Si_3N_4 test beam. The dashed curve parallel to the cantilever is part of a circle with radius 470 μm	66
Figure 3.2: Side view micrograph of a Si-rich SiN test beam. A straight dashed line is drawn parallel to the cantilever.....	67
Figure 3.3: Microscope image of SU-8 pattern fabricated with test mask.	74

Figure 3.4: Microscope image of cantilever fabricated by RIE (imaged in water). The SiO ₂ layer under the cantilever is removed by BOE (buffered oxide etchant). The surrounding structures are slightly undercut.....	76
Figure 3.5: Microscope images of cantilevers released with DRIE from the back side (imaged in water). a) Cantilever severely deformed downward b) Cantilever broken off.....	78
Figure 3.6: Microscope images of cantilevers fabricated by direct SU-8 exposure with the SiO ₂ layer removed under the beam (imaged in water). a) Cantilever was originally coated with gold, which was removed after release. b) Cantilever was never coated with gold.....	79
Figure 3.7: Microscope image of cantilever with gold layer on the bottom (imaged in water). The SiO ₂ layer is removed under the beam.	80
Figure 3.8: Monochromatic microscope image of 120 μm long cantilevers coated with 15 nm Au by thermal evaporation using a 15nm Cr adhesion layer (imaged in water). Both the input and output waveguides are released in this device. The cantilever tip height is estimated to be 10 μm by counting the number of interference fringes.	81
Figure 3.9: Monochromatic microscope image of 80 μm long cantilever coated with 15 nm Au by thermal evaporation without Cr adhesion layer (imaged in water). The tip height estimated by fringe counting is 1.5 μm.	82
Figure 3.10: a) SEM (Scanning Electron Microscope) image of propagation gap between cantilever and output waveguide. b) SEM image zoomed in on cantilever tip.	85
Figure 3.11: Monochromatic optical microscope images of fabricated devices (imaged in water). a) Waveguide cantilever b) Interferometric cantilever.....	86
Figure 3.12: a) Cross section schematic of packaged cantilever chip along waveguide. b) Cross section schematic of packaged cantilever chip along fluidic channel. c) Top-down schematic of PDMS layer.	90
Figure 3.13: a) Photograph of fully packaged waveguide cantilever chip (top down view). b) Monochromatic microscope image of cantilever inside micro fluidic channel filled with water (top down view). The image was taken through the packaging materials.	91
Figure 3.14: a) Layout of fluidic channels. b) Cross section schematic of packaged device along a channel. c) Top down photograph of fully packaged chip (width is 2.5 cm).	92
Figure 3.15: Microscope images of cantilevers inside fluidic channels taken at a) low and b) high magnification.	93

Figure 4.1: a) Block diagram of testing setup. b) Side view photograph of XYZ stages (without a device under test).....	96
Figure 4.2: a) Perspective view photograph of XYZ stages with device under test (DUT). b) Microscope image of laser light coupled from input fiber into on-chip waveguide.	97
Figure 4.3: Optical loss mechanisms in waveguide cantilever sensor.....	98
Figure 4.4: Scattered light intensity along a waveguide measured from a camera image of the waveguide.	99
Figure 4.5: Optical power drift of XYZ stages with set screws left untightened and fibers positioned at a minimal distance ($\sim 5 \mu\text{m}$) from the waveguide facets. Regression trendline and equation included.	101
Figure 4.6: Optical power drift of XYZ stages with set screws tightened and input fiber positioned far ($\sim 30 \mu\text{m}$) from the waveguide facet. Regression trendline and equation included.	102
Figure 4.7: Measured and theoretical output power as a function of cantilever vertical offset from output waveguide. The cantilever is $140 \mu\text{m}$ long and it is measured in air after drying.....	103
Figure 4.8: Response of a waveguide cantilever to 10 mM homocysteine sample. The cantilever length, initial tip height, and propagation gap are $140 \mu\text{m}$, $2.2 \mu\text{m}$, and $4 \mu\text{m}$ respectively.....	106
Figure 4.9: Response of a waveguide cantilever to 5mM homocysteine sample followed by DI water and hydrochloric acid. The cantilever length, initial tip height, and propagation gap are $110 \mu\text{m}$, $2.2 \mu\text{m}$, and $2 \mu\text{m}$ respectively.....	107
Figure 4.10: Response of a waveguide cantilever to homocysteine samples followed by cleaning with 1% w/w hydrochloric acid. The cantilever length, initial tip height, and propagation gap are $110 \mu\text{m}$, $2.2 \mu\text{m}$, and $4 \mu\text{m}$ respectively.....	108
Figure 4.11: Response of a waveguide cantilever to increasing concentrations of homocysteine. The cantilever length, initial tip height, and propagation gap are $70 \mu\text{m}$, $0.75 \mu\text{m}$, and $2 \mu\text{m}$ respectively.	109
Figure 4.12: Measured (dots) and theoretical (line) displacement of a cantilever vs. relative increase in optical power. The cantilever length, initial tip height, and propagation gap are $140 \mu\text{m}$, $2.2 \mu\text{m}$, and $2 \mu\text{m}$ respectively. It is tested in 5 mM homocysteine solution.	111
Figure 4.13: Optical output power of a waveguide cantilever and displacement measured by interferometry in response to homocysteine samples. The cantilever	

length, initial tip height, and propagation gap are 120 μm , 2.48 μm , and 2 μm respectively.	112
Figure 4.14: Optical output power of a waveguide cantilever and displacement measured by interferometry in response to dilute hydrochloric acid samples. The cantilever length, initial tip height, and propagation gap are 120 μm , 2.48 μm , and 2 μm respectively.....	113
Figure 4.15: Measured and theoretical displacement versus relative power increase of a waveguide cantilever. The measured values are obtained from the homocysteine (HC) and pH experiment data shown in Figure 4.13 and Figure 4.14.....	114
Figure 4.16: Response of a waveguide cantilever to a homocysteine sample synthesized by the bacterial quorum sensing enzymes. The sample was prepared externally to the device. The cantilever length, initial tip height, and propagation gap are 110 μm , 2.2 μm , and 4 μm respectively.	116
Figure 4.17: Photograph showing HLPT-CM enzymatic nanoparticles adsorbed on Tygon tubing inner wall. The tubing has inner diameter of 380 μm and outer diameter of 2.31 mm.	118
Figure 4.18: Response of a waveguide cantilever to SAH introduction; the input tubing is functionalized with Pfs and LuxS enzymes. The cantilever length, initial tip height, and propagation gap are 110 μm , 2.2 μm , and 2 μm respectively.....	119
Figure 4.19: Response of an optical cantilever to SAH introduction; there are no enzymes in the tubing. The cantilever length, initial tip height, and propagation gap are 110 μm , 2.2 μm , and 2 μm respectively.	120
Figure 5.1: Block diagram of testing setup used to characterize interferometric cantilever sensor.....	126
Figure 5.2: Custom-made laser illumination source with rotating diffusive disk.....	129
Figure 5.3: Image of a MEMS sample taken with laser illumination. a) The light is temporally and spatially coherent. b) The light is decohered spatially by passing it through the rotating disk.	130
Figure 5.4: Measured intensity profile from cantilever images obtained with laser or LED illumination at 40X optical magnification.	131
Figure 5.5: Measured intensity profiles from cantilever images obtained with different settings of the microscope's aperture diaphragm at 40X optical magnification.....	132
Figure 5.6: Measured displacements of cantilevers exposed to samples with different pH. All devices have a nominal length of 120 μm	136

Figure 5.7: Measured displacements of 30 cantilevers exposed to a pH of 2.56 (unpackaged device). All devices have a nominal length of 110 μm	137
Figure 5.8: Response of an interferometric cantilever to 1mM homocysteine sample.	139
Figure 5.9: Responses of 5 identical interferometric cantilevers to 1mM homocysteine solutions. The samples are introduced at time 0.	140
Figure 5.10: Responses of 5 identical interferometric cantilevers to homocysteine solutions with varying concentrations. The samples are introduced at time 0.	141
Figure 5.11: Responses of an interferometric cantilever to 1 mM homocysteine solution after repeated cleaning. The sample is introduced at time 0.	142
Figure 5.12: Interferometric cantilever displacement measured in response to different samples either 5 or 10 min after sample injection. Large displacement signifies high homocysteine concentration.	145
Figure 6.1: Possible scheme for integration of optical source and detector with the waveguide cantilever sensor at the chip level.	155
Figure 6.2: Possible scheme for providing optical sources and detectors for the waveguide cantilever sensor at the package level.	156
Figure 6.3: a) Fluorescent micrograph of a conventional protein microarray (source: www.arrayit.com). b) Hypothetical bright-field micrograph of a future interferometric cantilever array.	157

Chapter 1: Introduction

1.1 Background and Motivation

The field of BioMEMS (Bio-micro-electro-mechanical-systems) has attracted increasing attention in recent years [1-4]. It evolved from semiconductor technology to create miniaturized tools for biomedical applications. The terms Lab on a Chip [5-7], Micro Total Analysis System [8-10], and microfluidics [11-13] are often used interchangeably with BioMEMS (although, strictly speaking, they have somewhat different connotations). Due to the use of batch fabrication methods, BioMEMS components typically have low cost, small size, high density, and excellent reproducibility. They offer unprecedented opportunities for conducting multiple parallel experiments with small sample volumes and for making ultraportable medical equipment. BioMEMS technology can be applied to variety of fields, including fundamental biological studies (genomics, proteomics, immunology, cytology, histology); clinical diagnostics (point of care testing, high throughput screening); therapeutics (smart implants, drug delivery); and environmental monitoring (food and water quality control, biohazard detection). The goal of this dissertation is to develop BioMEMS tools to aid in antimicrobial drug discovery.

Bacterial infections pose a major threat to human health. The resistance of bacteria to conventional antibiotics is increasing due to genetic mutations [14, 15]. The process of discovering new antibiotics is slow and expensive. On average, the development of a new drug costs approximately \$400 million and takes 15 years [16]. First, genomic data and bioinformatics methods are used to identify possible drug

targets [17]. Then, large libraries of compounds are synthesized combinatorially and their effect on the target is tested *in vitro* prior to clinical trials [18, 19]. The experiments are currently performed with macroscale laboratory equipment using robotic dispensers and well plates; this approach requires relatively large sample volumes and operates in a serial fashion. Lab-on-a-chip technology could facilitate and significantly speed up the pre-clinical phase of drug discovery by performing multiple experiments in parallel with very small sample volumes [11, 20].

This dissertation develops a BioMEMS platform which consists of gold-coated microcantilever sensors embedded in microfluidic channels. It can be used to test the effect of a new type of drugs that suppress bacterial quorum sensing. Most bacteria communicate with each other and coordinate their behavior using signaling molecules [21]. They become pathogenic and form a drug-resistant biofilm only when they sense they have reached a sufficient population (quorum) to overrun the host's immune system [22]. While traditional antibiotics target protein synthesis in bacteria, there are efforts to discover new drugs that target their communications instead [23, 24]. This type of attack would degrade the bacteria's pathogenicity and biofilm forming properties, making them much more susceptible to the immune system and to medical treatment.

Bacterial enzymes that synthesize signaling molecules have been isolated and used *in vitro* [25, 26]. In the present research, these enzymes are immobilized in the microfluidics, and one of their products, homocysteine, is detected with the cantilever sensor. The output of the sensor can be used to determine if the enzymatic activity is inhibited by a given compound. The presented BioMEMS platform can be readily

scaled up to test large numbers of candidate drugs in parallel. By selecting an appropriate sensor coating, the device can potentially be used for many other applications beyond drug screening, including immunoassays and DNA hybridization assays.

1.2 Summary of Accomplishments

The main contribution of this dissertation is the development of two readout methods for microcantilever sensors. These devices are miniature beams coated with a selective surface layer; when analyte molecules bind to the coating, stress is generated and the cantilever deflects. Although there have been numerous demonstrations of cantilever sensors [27-30], the measurement of beam deflection (i.e. readout) remains problematic. It typically requires an elaborate free-space optical setup, and it can only be performed on one device at a time. Therefore, although very large numbers of cantilever are fabricated on a single chip, they are not usable for high-throughput screening or portable detection due to the limitations of the displacement measurement setup. In this dissertation, two different methods for displacement measurement are developed that overcome the shortcoming of the traditional approach: the waveguide cantilever and the interferometric cantilever. The detection of homocysteine produced by bacterial enzymes is demonstrated with both methods.

1.2.1 Design and Fabrication of Waveguide Cantilever for Liquid Samples

The first readout method is based on a device with integrated optical waveguides. The cantilever is formed by releasing the tip of an input waveguide from the substrate. It is coupled to an output waveguide across a small gap. As the cantilever

moves up or down, the power of light transmitted from the input to the output waveguide changes and serves as an indication of the cantilever displacement. This measurement requires an external laser to launch light into the on-chip waveguides and an external photodiode to collect it. However, these components are much smaller in size and cost than the traditional free-space optical setup. As a result, the integrated waveguide readout can lead to low-cost, portable cantilever sensors with minimal off-chip complexity or large arrays of cantilever sensors for high-throughput detection.

The idea of the waveguide cantilever has been demonstrated before for measurements in air [31-33] but not in liquid. The majority of chemical and biological samples are in the solution state; therefore, the capability of the sensor to operate in liquid is significant for biomedical applications. This dissertation reports for the first time a waveguide cantilever used for detection in liquid samples. A new device was designed that combines the cantilever sensor with a microfluidic channel. The sensitivity of the cantilever was modeled theoretically and experimentally verified. A customized fabrication process was developed to realize devices with sufficiently high sensitivity. The bulk of the process development consisted of reducing the residual stress in the materials in order to control out-of-plane beam curvature.

1.2.2 Device and Method for Interferometric Displacement Measurements

The second cantilever readout method is based on using a device with a built-in interference cavity. The device consists of a sloped transparent beam over a reflective substrate. When it is imaged with an optical microscope, an interference pattern is

formed by light reflected off the cantilever and light reflected off the substrate. The number and position of interference fringes depends on the distance of the cantilever from the substrate. The cantilever vertical displacement is found by extracting the horizontal fringe shift from digital images and multiplying it by the cantilever slope. Multiple cantilevers are rapidly read out with a single microscope by translating the stage to image each device before and after sample injection. A software algorithm was developed to automate the fringe shift measurements. This readout method is not applicable to portable cantilever sensors due to the requirement for an optical microscope; however, it is well-suited for high-throughput measurements of large cantilever arrays. It is also fully compatible with liquid samples.

The idea of the interferometric cantilever device and measurement method described here is new. It was conceived during the course of this dissertation research, and there were no demonstrations of it in prior literature. The device fabrication process and microfluidic packaging are similar to that of the waveguide cantilever described above.

1.2.3 Detection of Enzymatically Produced Homocysteine

One of the products of the bacterial quorum sensing enzymes, homocysteine, contains a thiol group. It has been shown that thiol compounds assemble on gold surfaces and create compressive stress. Both the waveguide and interferometric cantilevers have gold surfaces and are therefore capable of detecting the binding of homocysteine. The presence of this substance can be used as an indication of the enzymatic activity and by extension the effectiveness of candidate drugs that aim to inhibit the enzyme.

This dissertation demonstrates the detection of homocysteine from two different sources with both cantilever readout methods. First, samples prepared from commercially available homocysteine powder were tested. The cantilevers were shown to have a concentration-dependent response. Next, bacterial enzymes were assembled in microfluidics and used to synthesize homocysteine *in situ*. It was demonstrated that active enzymes led to significant cantilever bending, while denatured enzymes cause no measurable response.

1.3 Literature Review

This section reviews related work to establish the context of the dissertation. First, more background is provided on bacterial quorum sensing (QS) and the potential benefits of drugs that inhibit it. Next, examples of using BioMEMS for drug discovery applications other than QS inhibition are reviewed. Then, the different types of BioMEMS sensors are discussed, and the advantages of microcantilevers are highlighted. Finally, the traditional methods for cantilever displacement measurement are presented to emphasize the novelty of the two methods developed in this dissertation.

1.3.1 Bacterial Quorum Sensing

Most bacteria exist in the form of synergetic biofilms rather than isolated organisms [34]. The biofilm is a colony of cells embedded in a protective polysaccharide matrix secreted by the cells. It has been shown that the physiology of bacteria living in a biofilm is very different from that of isolated cells of the same species. The biofilm is much more resistant to antibiotics and bactericidal agents, probably due to the diffusion limitations imposed by the extracellular matrix on

incoming drug molecules [35, 36]. Also, bacterial colonies tend to produce more toxins that can rapidly kill the host organism [22].

The formation of biofilms is coordinated by a process known as quorum sensing [21, 37]. Each bacterium secretes small signaling molecules (known as autoinducers), which can be taken up by its neighbors. When the concentration of autoinducers in the environment exceeds some threshold, the genes encoding biofilm-like behavior start to be expressed. The threshold may vary considerably with conditions and is not well understood yet.

Quorum sensing and biofilm formation have tremendous social implications. According to the National Institutes of Health, biofilms account for more than 80% of microbial infections in the body [38]. They are especially common on implanted device surfaces, such as catheters, stents, pacemakers, and artificial joints [39]. Due to the increased resistance to drugs, a fully formed biofilm typically cannot be removed by conventional antibiotics, and surgical intervention is required [38]. Interestingly, biofilms also impact industrial equipment such as heat exchangers, water tanks, and ship hulls by causing increased corrosion and viscous drag [40]. Therefore, the prevention of the biofilm formation is important for a wide range of applications. The idea of drugs that inhibit quorum sensing has emerged recently [23, 24, 41]. This type of drugs should greatly reduce the severity of infections and make the bacteria more susceptible to immune clearance or treatment with conventional antibiotics.

There are several kinds of quorum sensing pathways and signaling molecules in different bacteria. However, it has been shown that a molecule called AI-2

(autoinducer-2) is common to many clinically relevant bacterial species [21, 25, 37, 42]. Drugs that inhibit the AI-2 signaling pathway are therefore particularly attractive since they can potentially be applied to a wide range of infectious diseases. A collaborative project was initiated at the University of Maryland to study this pathway using lab-on-a-chip technology¹. Several parallel approaches are being investigated, targeting either the AI-2 synthesis or uptake mechanisms. The present dissertation research was conducted as part of that broader project, and it was focused on developing a sensor to monitor the activity of AI-2 producing enzymes.

A simplified version of the AI-2 synthesis pathway is shown in Figure 1.1. It consists of two enzymes: Pfs and LuxS. The first enzyme converts the precursor SAH (S-adenosyl homocysteine) into SRH (S-ribosyl homocysteine) and adenine. The second enzyme converts SRH into AI-2 and homocysteine. Drugs that suppress quorum sensing may target either enzyme. The microcantilever sensor described in this dissertation is aimed at detecting the homocysteine by means of its high affinity for gold surfaces. There are no surface coatings currently available that can selectively bind SRH, adenine, or AI-2 molecules. Nevertheless, the presence of homocysteine is a sufficient indication of the activity of the AI-2 synthesis pathway as a whole.

¹ The principal investigators in this project are the following University of Maryland professors: W. E. Bentley (BIOE), G. F. Payne (UMBI), R. Ghodssi (ECE), G. W. Rubloff (MSE), and A. Nan (School of Pharmacy).

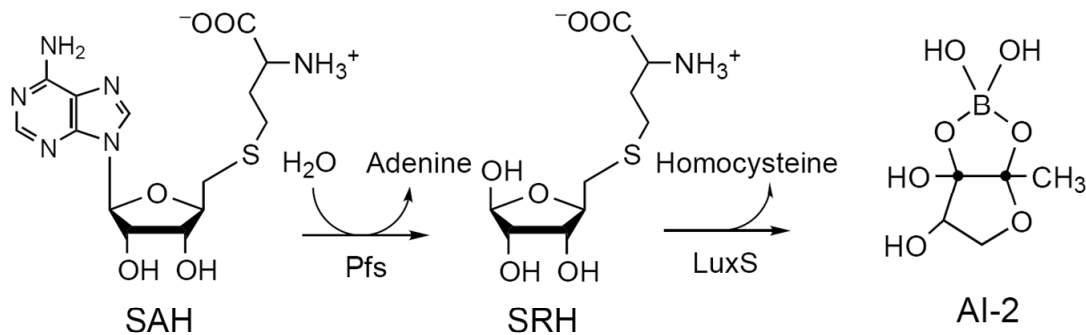


Figure 1.1: Biosynthetic pathway of AI-2. Adapted from ref. [37].

Modified Pfs and LuxS enzymes were isolated by my collaborators Lewandowski *et al.* [43, 44] and Fernandes *et al.* [26, 45] from genetically engineered *E. Coli* bacteria. The modifications included a tyrosine functional group, which allows the enzymes to be covalently bound to the polysaccharide chitosan. Lewandowski *et al.* immobilized the enzymes on microfabricated chips with deposited chitosan films and demonstrated that they retain catalytic activity after the binding. Fernandes *et al.* attached the enzymes to chitosan-coated magnetic nanoparticles and used them to synthesize AI-2 directly at cell surfaces. These results set the stage for reproducing the AI-2 synthesis pathway in a BioMEMS environment. Next, Luo *et al.* used the same immobilization approach to assemble Pfs on chitosan-coated electrodes within microfluidic channels and to synthesize SRH [46, 47]. The reaction kinetics was characterized, illustrating the effects of flow rate and nonspecific enzyme attachment on the conversion rate.

The work of my collaborators described here shows that significant progress has been made towards studying the AI-2 pathway on chip. However, in all of these examples, the detection of the reaction products was performed externally. Samples were collected and analyzed by HPLC (high performance liquid chromatography) or

tested with cells-based assays². Both of these approaches are very slow and labor intensive, and they are only feasible for a small number of samples. For the purposes of high-throughput screening of quorum sensing inhibitors, it is necessary to incorporate the detection mechanism on chip. This is precisely the role of the present dissertation research. The microcantilever sensors developed here are embedded within the fluidic channels, and they can be used to detect multiple samples in parallel.

To the best of my knowledge, there is currently only one other research group applying BioMEMS technology to the problem of bacterial quorum sensing [48, 49]. Ehrlich *et al.* recognize that biofilms are responsible for chronic infections of many implants. They envision a smart implant, which detects the onset of biofilm formation and releases antibiotics to kill the bacteria before the film is fully formed. The device has not been demonstrated, but the proposed design consists of a BioMEMS sensor for detecting bacterial signaling molecules and gated reservoirs for drug delivery. The sensor is based on a cantilever viscometer. The bacterial autoinducers bind to an engineered receptor protein, and an enzymatic reaction is initiated that decreases the viscosity of the fluid inside the device. This viscosity change is sensed by the cantilever, and the drug release is triggered. It should be noted that the design of Ehrlich *et al.* is substantially different from the work described in this dissertation. First, a different quorum sensing pathway is explored that is based on a peptide signaling molecule instead of AI-2. Second, instead of inhibiting bacterial

² The assay is a culture of *V. Harveyi* “reporter” cells that emit bioluminescence when they detect AI-2. The luminescence is measured with a spectrophotometer.

communication, the authors aim to use it as a timing signal for drug release. Third, the cantilever sensor is used to detect a different effect (viscosity change as opposed to surface binding) in a different sensing mode (dynamic and static mode operation are discussed in Section 1.3.3).

1.3.2 BioMEMS for Drug Discovery

A variety of BioMEMS tools are being developed for drug discovery application beyond quorum sensing inhibition. There are successful demonstrations of devices that synthesize chemical compounds combinatorially [50, 51], test compounds on living bacterial cells [52], sort cells according to surface receptors [53], identify proteins[54], and assay enzyme activity [55].

BioMEMS have a number of advantages compared to conventional laboratory techniques based on well plates and robotic dispensers. First, they have much smaller sample volumes (nL compared to mL), which minimizes the use of valuable reagents and speeds up diffusion-limited reactions. Second, the samples are enclosed in channels, preventing them from evaporating. Third, the devices inherently have a small footprint, enabling massively parallel operation with low fabrication costs. Fourth, various sensors can potentially be integrated in close proximity to the sample, providing information with high spatial and temporal resolution. For these reasons, BioMEMS are being developed for all aspects of the drug discovery process: target identification, compound generation, lead identification, and lead optimization [7, 11, 13, 20, 56-59]. Most of this work has a different scope than the present dissertation, which is primarily aimed at developing an on-chip sensor for high-throughput detection. The next section reviews the main types of BioMEMS sensors

commonly reported in literature. Although they were usually developed for other applications, they can readily be adapted to the needs of drug discovery.

1.3.3 BioMEMS Sensors

A myriad of miniaturized biochemical sensors with different detection principles and device structures have been demonstrated [3, 8, 59, 60]. In general, they contain a selective coating (either biomolecular or synthetic) with an affinity for a given analyte; the binding of the analyte to the coating is detected by optical, electrochemical, capacitive, acoustic, or mechanical means. Each of these transduction mechanisms has different advantages and limitations, and the optimal choice depends largely on the application. Some types of BioMEMS sensors are simply miniaturized versions of conventional laboratory instruments (e.g. optical, electrochemical, and capacitive measurement tools). Others are unique to the lab-on-a-chip domain and have no macroscale counterparts (e.g. acoustic and mechanical sensors).

Optical biosensors typically operate in the fluorescence detection mode. The target molecules are tagged with a fluorescent label (fluorophore). The sample is illuminated with an excitation signal and the scattered (or transmitted) light is captured and analyzed. Since the fluorophore causes a characteristic frequency shift in the collected light, its presence can be determined from the light's spectral components. This technique is based on the well-established fields of fluorescent microscopy and DNA spotted arrays, and it has been implemented in BioMEMS devices by a number of authors [61-64]. Fluorescent detection has very high sensitivity, and even single molecule detection has been reported [65]. Its major

limitation, however, is the need to label the target molecules with a fluorophore. This greatly increases sample preparation times. Additionally, labeled target species are no longer in their intrinsic state and may have different properties from their unlabeled counterparts. This concern is especially valid for proteins with complex structures [66].

Another optical detection technique exploited for BioMEMS sensors is surface plasmon resonance (SPR) [67, 68]. A plasmon wave is excited by coupling light along a metal surface at a specific angle with a prism. The binding of biomolecules to the metal surface is detected by the change in the critical coupling angle. The advantage of SPR detection is that it does not require the target molecules to be labeled. However, it requires a bulky optical coupling and measurement setup that poses significant challenges for miniaturization and parallel operation.

Electrochemical (also called amperometric or voltammetric) sensors measure electrical currents to detect biochemical events [69, 70]. Their application is typically limited to detection of specific molecules that undergo reduction or oxidation reactions and result in net current flow. This method can be extended to other molecules if they are tagged with redox labels [71]. The labels then undergo the necessary electrochemical reactions for detection. However, as in the case of fluorescent labeling, redox labeling complicates sample preparation and affects the properties of the biomolecules being tagged.

Capacitive sensors measure the changes in capacitance of an electrode to which target molecules bind [72, 73]. The capacitance variations are caused by the dielectric properties of the added molecules or by their net charge. This method can be readily

implemented on the microscale by field effect transistors (FET), which are simple and highly sensitive charge detectors. The resulting devices are called CHEMFETs [74]. Another advantage of these biosensors is that they enable label-free detection of the target molecule. However, capacitive biosensors require extensive calibration and are prone to drift noise. Since the capacitance changes with solution properties (e. g. pH, temperature, and ion concentration) care must be taken to separate these secondary effects from biomolecular binding events.

Acoustic transduction is also utilized by some BioMEMS sensors for label-free detection. In surface acoustic wave (SAW) sensors [75, 76], a SAW wave is generated by a piezoelectric film, which is covered by a patterned metal layer. The propagation of the acoustic wave is influenced by the binding of biomolecules on the metal surface due to the change in acoustic impedance. This change is measured electrically, and the biomolecules are detected. This method, however, typically uses a large footprint (a few mm) to ensure that the acoustic wave is appreciably affected by the sample. Scaling the devices down in size negatively impacts their sensitivity. For this reason, SAW sensors may not be favorable for miniaturized sensor arrays on a chip. Another biosensing transduction technique which may be considered acoustic is the quartz crystal microbalance (QCM) [77, 78]. In these devices, the target molecules bind to the surface of a resonant piezoelectric crystal and reduce its resonant frequency due to the increased mass. Traditional QCMs are cut out of quartz crystals and are not compatible with MEMS batch fabrication. Therefore, their potential for arrayed operation is limited. Thin film piezoelectric resonators have also

been developed that are batch fabrication compatible [79], but they have lower sensitivity than their bulk crystal counterparts.

Micromechanical biosensors use micromachined structures such as cantilever beams or membranes to which the analyte molecules bind. There are two detection mechanisms for this type of sensors: static (bending) and dynamic (resonant). In static mode [80-82], the microstructure is displaced due to the surface stress exerted by the binding molecules. In dynamic mode [83-85], the frequency response of the structure is changed due to the added mass, the modified mechanical spring constant, or the damping characteristics of the analyte. To obtain the dynamic response, the structure is actuated, and its displacement as a function of time or frequency is measured. The key advantages of micromechanical biosensors are that they allow for label-free detection and are fully compatible with MEMS batch microfabrication. Although some of the other technologies reviewed earlier are also label-free (e. g. SAW, QCM, and SPR), they are not as suitable for miniaturization and arrayed operation. While other types of sensors usually are negatively impacted by being scaled down, micromechanical devices actually benefit in sensitivity due to the increase of surface to volume ratio. The next section reviews microcantilevers, which are the most common form of micromechanical sensors.

1.3.4 Microcantilever Sensors

1.3.4.1 Applications of Cantilever Sensors

Microcantilever sensors have been adapted for a wide variety of biological and chemical applications by selecting an appropriate coating layer [27-30]. Dynamic mode detection is normally limited to gas-phase samples, while static mode can be

readily used for both gases and liquids. Although the dynamic mode has been demonstrated with liquid samples, it suffers from high viscous damping and reduced sensitivity [27, 86].

Dynamic mode cantilevers have been employed for detecting humidity [87], alcohol vapor [88], mercury vapor [89, 90], DMMP (dimethyl methylphosphonate)[91], and airborne virus particles [83]. Static mode devices coated with DNA strands or proteins have been used to detect DNA hybridization [81, 82, 92-94], binding of antigens to antibodies [30, 95-97], and binding of substrates to enzymes [98, 99]. The static mode cantilever has been found more suitable for biological applications due to its ability to operate in liquid, which is the natural environment of biomolecules. For this reason, the sensors developed in this dissertation are of the static type.

1.3.4.2 Common Readout Methods

Despite the promise of microcantilever sensors for arrayed operation, most demonstrations to date have been performed with single devices. This is largely due to the limitations of available methods for measuring cantilever displacement in both static and dynamic modes. The measurement typically employs an external optical setup which requires precise alignment and can only be used for one device at a time. Therefore, the potential of cantilever sensors for high throughput detection is practically limited by the characteristics of the readout method.

The most common method for displacement measurement is the “optical lever” approach, which was adapted from the field of Atomic Force Microscopy [29, 92, 93, 100-102]. A focused laser beam is reflected off the cantilever surface, and captured

by a PSD (Position Sensitive Detector) as shown in Figure 1.2. The cantilever displacement causes movement of the laser spot on the PSD and a change in its output voltage.

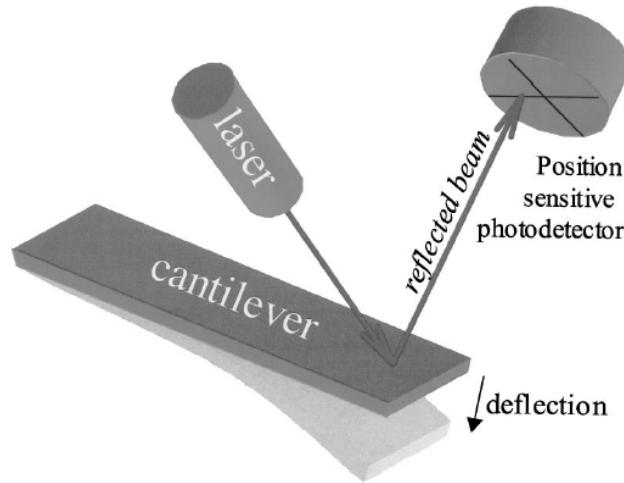


Figure 1.2: Schematic of the “optical lever” readout. Reproduced from ref. [27].

This method is very sensitive, but it requires elaborate free-space optics with precise alignment of the laser beam to the device under test. Moreover, the ratio of PSD signal to cantilever displacement depends on the exact position of the laser spot on the cantilever. This ratio is unimportant for resonant frequency measurements, but it greatly impacts static mode operation. For example, a change in PSD output due to slight laser misalignment can be misinterpreted as cantilever bending. Since the alignment cannot be perfectly reproduced, the laser must be kept aligned to the cantilever throughout the static mode experiment. This precludes parallel measurements. If a cantilever array is exposed to a sample, the response of only one device can be captured. Custom-made arrays of lasers and PSD’s for measuring several cantilevers in parallel have been demonstrated [93, 101, 102]. However, this approach leads to greatly increased instrumentation complexity and difficulty of

alignment. It is not feasible to increase the number of lasers much further, while the number of cantilever on a chip can easily be in the hundreds or even thousands.

Another common method for measuring cantilever response involves the integration of on-chip displacement sensors. This approach not only allows multiple devices to be measured in parallel, but also simplifies the external measurement setup. The built-in sensors can be piezoresistive [103, 104], piezoelectric [90, 105], capacitive [106, 107], or transistor-based [95]. Unfortunately, all of these technologies greatly increase the fabrication complexity and cost of the cantilevers, which should be simple, cheap and disposable. For cantilever arrays, multiple electrical connections must be made from the sensors to off-chip components, complicating the packaging. Moreover, the resolution of the integrated displacement sensors is considerably lower than that of the PSD-based method described above, and they suffer from increased signal drifts. The output from the sensors is an electrical signal; converting that into actual displacement requires calibration, which may change from device to device. Therefore, comparing the results from multiple cantilevers may be problematic. The integrated sensor readout may be appropriate for applications where portability is essential while the sensitivity, repeatability, and cost are not primary concerns.

1.3.4.3 Waveguide Readout

As explained in Section 1.2.1, a new readout approach based on integrated optical waveguides has been demonstrated by several groups [31-33]. It addresses many of the limitations of the traditional displacement measurement methods. It reduces the complexity of the external setup; at the same time, the waveguide cantilevers are

simpler to fabricate and potentially more sensitive than the devices with integrated displacement sensors discussed above. Each of the published demonstrations of this new readout method is briefly reviewed here.

Zinoviev *et al.* report a waveguide cantilever operating in dynamic mode that is illustrated in Figure 1.3 [32]. The input and output waveguides consist of a Si_3N_4 core on top of a SiO_2 cladding layer, while the cantilever is composed of a SiO_2 core with air cladding.

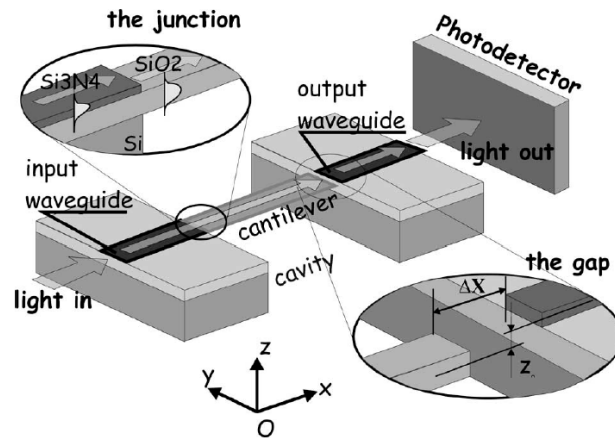


Figure 1.3: Schematic of cantilever with integrated waveguide readout reported by Zinoviev *et al.* Reproduced from ref. [32]

The device was actuated with a piezoelectric shaker, and the resonant frequency was measured from the spectrum of the photodetector output signal. The authors claim that the sensitivity of this readout in the dynamic mode is close to that of the PSD-based approach. Static mode operation was not reported, and the device was not tested in liquid. Also, the cantilever did not include a surface coating for detecting particular analytes. The authors point out the use of multiple layers could lead to excessive beam bending due to residual stress effects. They fabricate the cantilever from a single SiO_2 layer without a coating in order to keep it flat.

Pruessner *et al.* demonstrated another waveguide cantilever in dynamic mode [31]. The device was realized in the InP material system, making it theoretically possible to fabricate the light source on chip. In this work, the cantilever was an in-plane structure instead of the more typical out-of-plane design (Figure 1.4). It was electrostatically actuated by lateral electrodes in order to measure its resonant frequency from the optical output signal. The same design was further developed by Siwak *et al.* [88]. It was coated with the organic semiconductor pentacene on the top surface and used for detecting alcohol vapor. This device is ineligible for static mode detection due to its in-plane design (there is no available method for applying a coating to the sidewall of the beam, where it is needed to cause bending). Operation in liquid was not attempted.

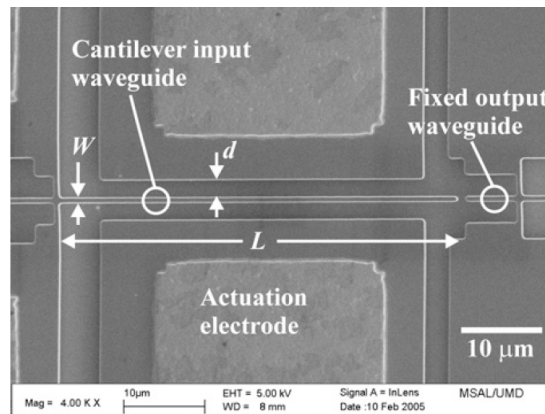


Figure 1.4: SEM of cantilever with integrated waveguide readout reported by Pruessner *et al.* Reproduced from ref. [31].

Nordstrom *et al.* reported the first waveguide cantilever for static mode detection [33, 108]. The waveguides consist of an SU-8 core and a modified SU-8 cladding, and the cantilever is an air-clad SU-8 core. Figure 1.5 shows a schematic of the design. It did not include any surface coating layer for detecting analytes, possibly due to concerns of excessive residual stress (as in the work of Zinoviev *et al.*

discussed above). The device was tested only in air by deflecting the cantilever tip with a microprobe while measuring the output optical power. The authors calculate the theoretical performance in liquid but do not test it experimentally. The minimal detectable displacement in air was found to be 45 nm, which corresponds to a surface stress of 0.2 N/m. It was concluded that this level of sensitivity is not sufficient for typical biochemical detection experiments, and that further improvement is necessary.

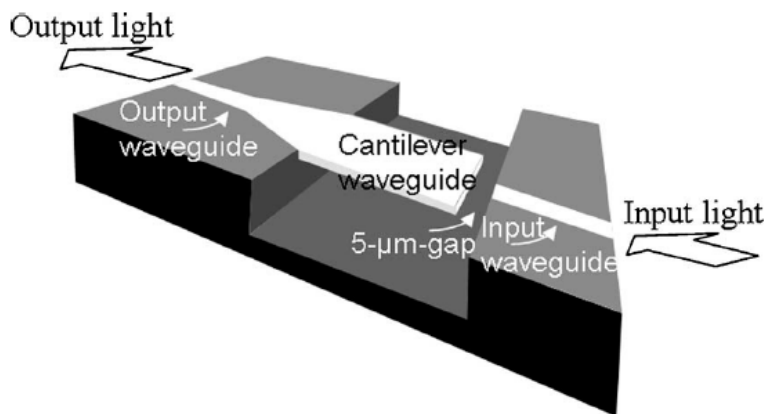


Figure 1.5: Schematic of cantilever with integrated waveguide readout reported by Nordstrom *et al.* Reproduced from ref. [33].

In summary, none of the previous demonstration of the waveguide cantilever was performed in liquid. Two of them were used in the dynamic mode, and one in the static mode. The static mode device did not have a coating layer for detecting particular analytes, and its sensitivity was too low for typical applications. In contrast, the waveguide cantilever developed in this dissertation was demonstrated to be fully compatible with liquids. It has much higher sensitivity than the device reported by Nordstrom *et al.*, and it includes a gold coating made possible by improved residual stress control during fabrication. Although the gold layer here serves only for detection of homocysteine, it can be functionalized with thiol-labeled probe biomolecules and used for many other applications [27, 29, 30].

1.3.4.4 Interferometric Readout

The interferometric readout method described in Section 1.2.2 is new to this dissertation and has not been previously demonstrated. Although it still requires an external measurement setup (a microscope with a digital camera), the alignment tolerance is greatly relaxed compared to the PSD-based method. This allows the microscope to be moved between cantilevers to image an entire array before and after introducing a sample. Therefore, the response of the whole array to the sample can be captured with a single reader. The interferometric cantilever is much simpler to fabricate than the devices with integrated displacement sensors, and it has no electrical connections. It is also more sensitive and does not require any sensor calibration. This section reviews several other interferometric techniques used to measure beam displacement and explains their differences from the method developed in this dissertation.

Stievater *et al.* reported microbridge resonators with on-chip interference cavities as shown in Figure 1.6 [91]. The doubly clamped beam is illuminated normally with light from an optical fiber, and the reflected light is collected with the same fiber. Vertical displacement of the beam changes the cavity length and therefore the reflected light power. The authors used this effect to measure the resonant frequency of the beams from the modulated reflection signal. A similar approach was demonstrated by Svitelskiy *et al.* for nanoscale bridges [109]. However, this method is not eligible for static mode detection due to light intensity drifts. Any small change in laser output power or fiber placement, for example, can be misinterpreted as beam displacement. Moreover, the method requires a bridge instead of a cantilever in order

to form a uniform interference cavity (bridges are much stiffer and less sensitive than cantilevers). The approach reported in this dissertation is based on analyzing the interference pattern of the cavity instead of taking power measurements. Therefore, it is immune to intensity drifts and uses a non-uniform cavity formed by a cantilever.

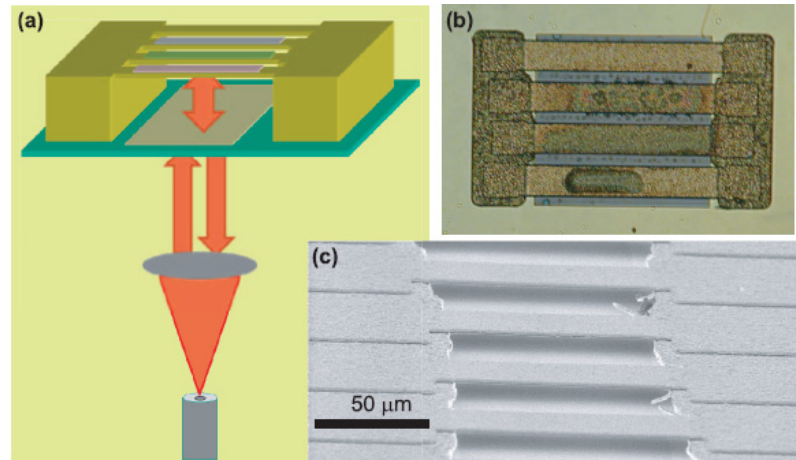


Figure 1.6: Schematic (a) and micrographs (b, c) of microbridge resonators with on chip interference cavity. Reproduced from ref. [91].

Another interferometric technique has been used previously for measuring static cantilever displacement. It is based on optical profilers, which are specialized microscopes with interferometric objectives [94, 110, 111]. However, the cost of these tools is normally 10 times higher than that of a conventional optical microscope. The profiler approach also has some technical limitations. First, it requires custom modifications to enable measurements through liquid [111]. Second, the interference cavity is external to the chip since it is formed between the cantilever surface and a reference mirror in the objective. This means that the measurement is greatly affected by stage vibrations and changes in the refractive index of the medium. In contrast, the interference cavity in this dissertation is formed between the cantilever and the

substrate. Due to its short length and mechanical stability, it is much more immune to refractive index fluctuations and stage vibrations.

1.4 Structure of Dissertation

Chapter 1 has introduced the background and motivation of this research. Chapter 2 describes in detail the theory of operation and design considerations for both the waveguide cantilever and interferometric cantilever. The optical and mechanical sensitivity are discussed, and the procedure for analyzing the interference images is explained. Chapter 3 describes the fabrication and packaging processes for both devices. Chapters 4 and 5 present the testing procedures and results for the waveguide and interferometric cantilever, respectively. The devices are used to detect homocysteine samples obtained from commercially available powder or synthesized by the bacterial quorum sensing enzymes. Finally, Chapter 6 summarizes this dissertation and suggests possible further work.

Chapter 2: Theory of Operation and Design

2.1 Introduction

As discussed in Chapter 1, this dissertation develops two different types of microcantilever sensors suitable for high-throughput studies of bacterial quorum sensing. The first type contains integrated optical waveguides, and the second type makes use of an on-chip interference cavity that is imaged with an external microscope. Both kinds of sensors are embedded in microfluidic channels for sample delivery. This chapter presents in detail the theory of operation and design considerations for each device.

2.2 Waveguide Cantilever

2.2.1 Device Structure

The waveguide cantilever sensor consists of SU-8 polymer optical waveguides with a SiO₂ bottom cladding layer on a Si substrate. A schematic of the device with the relevant layer thickness labels is shown in Figure 2.1. The cantilever is a section of the input waveguide (IWG) that is released from the SiO₂ surface and is coated with a thin gold layer. It faces the output waveguide (OWG) across a small gap, and it is slightly curled up due to residual stress gradient in the SU-8. The effect of this curvature on the optical coupling and sensitivity is discussed in Section 2.2.3, and the fabrication process used to tune the residual stress is described in Chapter 3. The attachment of analytes to the gold surface causes the cantilever to bend further up or down from its initial position. To detect this bending, light is coupled to and from the

on-chip waveguides via optical fibers mounted on XYZ positioning stages (the testing setup is described in Chapter 4). The cantilever's displacement changes the power of light coupled to the output waveguide, which is measured with an external photodetector.

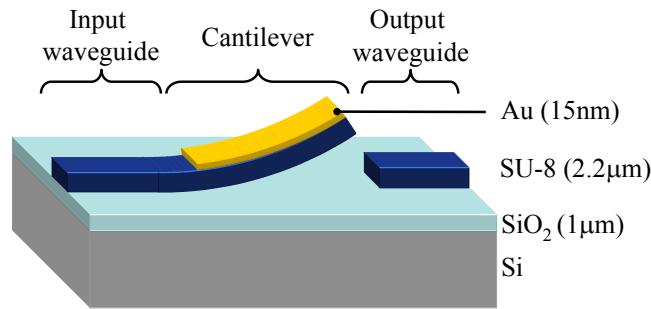


Figure 2.1: Schematic (3D) of a waveguide cantilever before the addition of the microfluidic channel.

The SU-8/SiO₂ waveguide system has been demonstrated previously for fabrication of various BioMEMS optical sensors [64, 112]. It was chosen here due to its low propagation loss, low residual stress (which minimizes the cantilever curvature), and the availability of equipment for SU-8 fabrication. Most authors use a Pyrex substrate to form the SU-8 waveguides. Here, a single-crystal silicon substrate was chosen to allow for cleaving. This results in smooth waveguide facets that facilitate the optical coupling to external fibers.

The cantilever is embedded in a microfluidic channel to enable detection of liquid samples with small volumes. The channel is formed by a molded PDMS polymer layer placed on top of the cantilever chip as shown in Figure 2.2a. The channel is perpendicular to the waveguides. The PDMS layer is secured in place by an external compression package, and the channel is connected to external tubing via steel capillaries (the packaging is described in Chapter 3). Figure 2.2b shows a top-down

view of the SU-8 layer to illustrate how a fluidic seal is formed. Tether structures are used to block the fluidic leakage paths parallel to the waveguide.

The use of molded PDMS for creating microfluidic channels is very common [113, 114], but it has not been demonstrated before with cantilever sensors. Most cantilever studies in liquid have been performed in macroscale flow cells or Petri dishes rather than microfluidic environments. The reason for choosing the PDMS channel approach here is its compatibility with more complicated microfluidic networks that incorporate pneumatic valves and pumps [113]. Therefore, the device developed in this dissertation can be readily integrated within a larger lab-on-a-chip system.

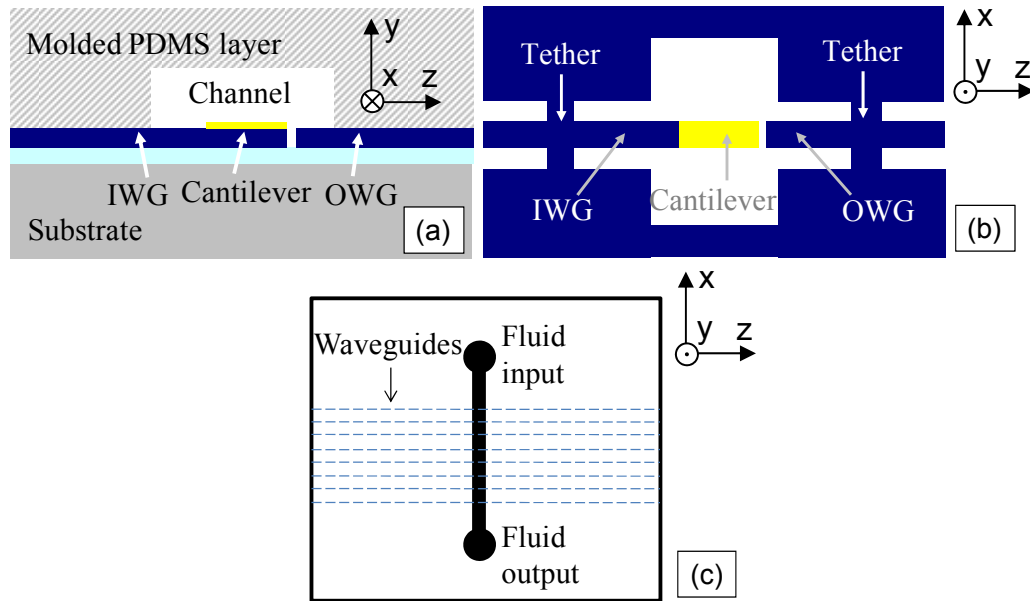


Figure 2.2: a) Cross section along waveguide cantilever embedded in microfluidic channel. b) Top down view of SU-8 layout. c) Top down view of fluid channel layout. The XYZ coordinate systems used for the mechanical and optical analysis later are shown.

The optical waveguide has cladding materials with different refractive indices along its length: SiO_2 ($n = 1.5$), PDMS ($n = 1.4$), and water ($n = 1.33$). In all cases, the refractive index of the SU-8 core ($n = 1.6$) is higher than that of the cladding, and

the waveguiding condition is satisfied. There is an increased propagation loss in the tethers due to lateral light leakage from the waveguide and in the gold layer due to its imaginary refractive index. Due to the short length of these lossy regions, the total optical loss through them is acceptable. The propagation loss in the waveguides is discussed in Section 2.2.3.6, and the final dimensions of the device are given in Section 2.2.4.

2.2.2 Mechanical Sensitivity

The mechanical sensitivity of the cantilever is defined here as the vertical tip displacement Δt per unit surface stress $\Delta\sigma_s$. This quantity is given by the Stoney formula (Equation 2.1) [115]. The relevant variables are defined in Table 2.1. The cantilever in this work is composed of two layers, SU-8 and gold, with different Young's moduli (E). It has been shown that Equation 2.1 can be used for a composite cantilever by replacing E with the effective Young's modulus [116]. E_{eff} is given by Equation 2.2, where E_i and I_i are the Young's modulus and the moment of inertia of each layer for N layers. However, using the material properties and thicknesses given in Table 2.2, it can be shown that $E_{eff} \approx E_{SU-8}$ in this work, i.e. the effect of the gold is negligible.

$$\text{Equation 2.1} \quad \frac{\partial t}{\partial \sigma_s} = 3 \frac{(1-\nu)}{E} \left(\frac{L}{H} \right)^2$$

$$\text{Equation 2.2} \quad E_{eff} = \frac{\sum_{i=1}^N E_i I_i}{I}$$

Table 2.1: Definitions of variables

Symbol	Definition
L	Cantilever length
H	Cantilever thickness
W	Cantilever width
I	Moment of inertia about cantilever's neutral axis ($I = WH^3/12$)
E	Young's modulus
ν	Poisson's ratio
t	Height of cantilever tip above substrate
$d(z)$	Height of cantilever at point z along cantilever axis
σ_s	Surface stress caused by binding of analytes
$\frac{\partial \sigma_r}{\partial y}$	Residual stress gradient in cantilever material
k	Cantilever curvature

Table 2.2: Young's modulus and thicknesses of cantilever materials in this work (other materials commonly used for cantilevers are given for comparison). These are representative values obtained from literature.

Material	E (GPa)	ν	Thickness in device (nm)
SU-8	2	0.22	2000
Au	78	0.44	15
Si ₃ N ₄	270	0.27	-
SiO ₂	70	0.17	-
Si	150	0.17	-

Equation 2.1 shows that the mechanical sensitivity depends on the material stiffness, the beam thickness, and the beam length. The stiffness of SU-8 is quite low. Its Young's modulus is 2 orders of magnitude lower than other materials commonly used for cantilever fabrication (Table 2.2), and it is therefore favorable for high

mechanical sensitivity. The sensitivity is maximized by choosing the minimal thickness of SU-8 that could be fabricated in house (approximately 2.2 μm). The length of the cantilever is limited by the upward curvature and optical coupling considerations to approximately 150 μm as discussed next.

Cantilevers with a residual stress gradient assume a parabolic bending profile shown by Equation 2.3 [117, 118]. The resulting cantilever tip height is given by Equation 2.4, where k is the curvature.

$$\text{Equation 2.3} \quad d(z) = \frac{(1-\nu)}{2E} \left(\frac{\partial \sigma_r}{\partial y} \right) (z - z_0)^2 = \frac{k}{2} (z - z_0)^2$$

$$\text{Equation 2.4} \quad t = \frac{(1-\nu)}{2E} \left(\frac{\partial \sigma_r}{\partial y} \right) L^2 = \frac{k}{2} L^2$$

Since the output waveguide is fixed to the substrate, the tip height t represents the vertical misalignment between the input and output waveguides. To allow for adequate optical coupling (Section 2.2.3.4), the value of t should be less than the waveguide thickness (2.2 μm). Due to the fabrication constraints described in Chapter 3, the minimal curvature of the cantilever is about 0.23 mm^{-1} ; therefore, the cantilever length is limited to approximately 140 μm (even though longer devices would have higher mechanical sensitivity). The final cantilever dimensions are given in Section 2.2.4 after the discussion of optical sensitivity.

It should be noted that the Stoney formula (Equation 2.1) is based on idealized beam theory and is only an approximation. More accurate equations have been derived to predict cantilever displacement due to surface stress [115, 119], but that level of accuracy is not needed in the present case. Sader *et al.* showed that the error resulting from the Stoney equation is less than 10% if the ratio of cantilever length to

width is larger than 2.5 [119] (this condition is fulfilled here). Since there is potentially larger error due to deviations in material property values, Equation 2.1 was deemed acceptable for this design.

2.2.3 Optical Sensitivity

The optical sensitivity of the device is defined here as the change in optical transmission per unit cantilever displacement. To determine this quantity, it is necessary to express the power of light received at the output as a function of cantilever displacement. This requires knowledge of the waveguide mode shapes. First, an analytical model is used here to show the functional form of the modes and the transmission coefficient. Next, finite element simulations are performed to find the exact mode shapes and also to calculate the waveguide propagation loss. Using these mode shapes and considering the effects of free-space divergence, the transmission coefficient and the optical sensitivity of the device are determined. Finally, the sources of noise and the maximization of signal to noise ratio are discussed.

2.2.3.1 Analytical Model

This section describes the optical modes using an approximate analytical model of rectangular waveguides [120]. Although the model is less accurate than the finite element simulations performed later, it gives insight into the functional form of the waveguide modes. Following the coordinate system in Figure 2.2, the rectangular waveguide supports two types of modes: E_x^{mn} (the primary component of the E field is in the x direction) and E_y^{mn} (the primary component of the E field is in the y direction). These modes are also called TE (transverse electric) and TM (transverse

magnetic) respectively; m and n are mode orders in the x and y directions. The electric field is approximated by Equation 2.5 for E_x^{mn} modes and by Equation 2.6 for E_y^{mn} modes, where β is the propagation constant.

$$\text{Equation 2.5} \quad E_x^{mn}(x, y, z) = E_{x0} F_x^m(x) G_x^n(y) \exp(-j\beta_x^{mn} z)$$

$$\text{Equation 2.6} \quad E_y^{mn}(x, y, z) = E_{y0} F_y^m(x) G_y^n(y) \exp(-j\beta_y^{mn} z)$$

The functions $F^m(x)$ and $G^n(y)$ are the horizontal and vertical mode profiles, respectively, and can be obtained by solving a set of equations subject to the waveguide's boundary conditions [120]. Importantly, according to the functional forms above, the horizontal mode profiles are independent of y and the vertical mode profiles are independent of x .

The modal shapes in the cantilever and output waveguide are closely matched if the cantilever is straight. When it bends due to residual stress gradient or surface stress, its modes shift by t in the y direction³ but not in the x direction. Therefore, only the vertical mode profiles become significantly mismatched; the horizontal mode profiles remain matched and do not affect the change in coupling. Based on this simplification, the coupling coefficient (or transmission coefficient) from the cantilever to the output waveguide is given by Equation 2.7 [120] and illustrated in Figure 2.3.

$$\text{Equation 2.7} \quad C(t) = \frac{\left(\int G_2(y-t) G_3^*(y) dy \right)^2}{\int G_1(y) G_1^*(y) dy \int G_3(y) G_3^*(y) dy}$$

³ Strictly speaking, the cantilever displacement causes both shifting and tilting of the mode. Here we assume that the tilt is negligible. The effect of tilt is shown in Section 2.2.3.5.

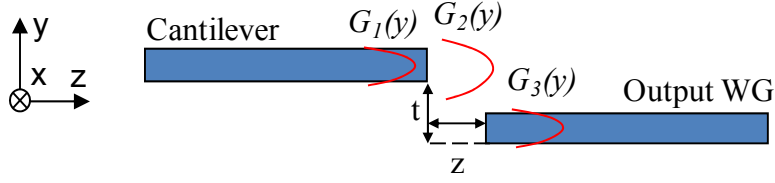


Figure 2.3: Schematic of light coupling from cantilever into output waveguide across gap

Here, $C(t)$ is the ratio of power captured by output waveguide to power leaving the cantilever with tip height t . $G_1(y)$ is the mode shape exiting the cantilever, $G_2(y)$ is the broadened mode shape that arrives at output waveguide, and $G_3(y)$ is the mode shape of the output waveguide. G_1 is different from G_2 due to the mode divergence upon propagation through free space. The beam actually diverges in both the x and y directions, and $F(x)$ also broadens. However, this horizontal divergence is small because the waveguide's width-to-thickness ratio is large; as a result, the horizontal mode profiles remain closely matched and do not appreciably affect the optical coupling.

Since only the vertical mode shapes are of interest here, a planar waveguide model can be used instead of the rectangular waveguide model to further simplify the analysis [120]. The planar model assumes that the waveguide width is infinite and there is no lateral confinement of the light. The vertical mode shapes have the form given by Equation 2.8, where H is the waveguide thickness and the parameters a_{1-4} and b_{1-3} can be found by matching the electromagnetic boundary conditions

$$\text{Equation 2.8} \quad G(y) = \begin{cases} a_1 \exp(b_1 y) & \text{for } (-\infty < y < 0); \\ a_2 \cos(b_2 y) + a_3 \sin(b_2 y) & \text{for } (0 < y < H); \\ a_4 \exp(-b_3 y) & \text{for } (H < y < \infty). \end{cases}$$

Matching the boundary conditions requires the solution of a transcendental equation, which takes into account the waveguide geometry and material refractive indices. It is solved graphically as shown in Figure 2.4 for a planar waveguide with a 2.2 μm thick SU-8 core ($n = 1.6$), SiO_2 cladding on the bottom ($n = 1.5$), and water cladding on the top ($n = 1.33$). The optical wavelength is 635 nm. The x-coordinates of the crossings of the blue and red lines in the plots are the effective mode indices (n_{eff}). The corresponding propagation constants are given by $\beta = 2\pi n_{eff} / \lambda_0$. The effective mode indices can be used to find the unknown parameters in Equation 2.8 [120]; however, this step is omitted since $G(y)$ will be found by the more precise FEM method later in Section 2.2.3.2. The graphical solution is used here only to find the number of modes.

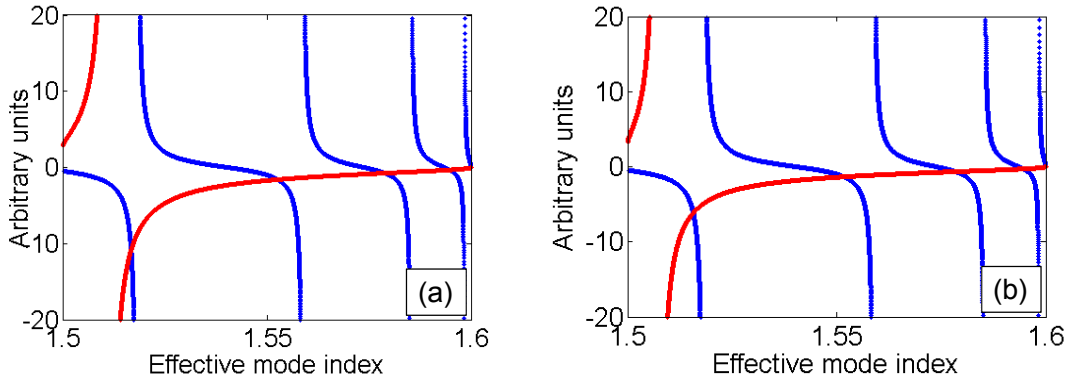


Figure 2.4: Graphical solutions of the transcendental equation for a planar waveguide for (a) TE and (b) TM modes.

There are 4 solutions in each plot in Figure 2.4. Therefore the waveguide supports 4 TE and 4 TM vertical mode shapes. Each mode has a different shape (Equation 2.8) and transmission coefficient (Equation 2.7). The distribution of power among the modes is random since it depends on scattering from waveguide defects. We assume that most of the power is in the fundamental TE and TM modes, and the contributions

of the other modes to the transmission coefficient are negligible. This assumption is partly justified by the fact that higher order modes are less confined to the core and have higher propagation and coupling losses [121]. It can be shown that if the SU-8 thickness is reduced below 570 nm, the waveguide would support only one vertical mode. The use of a single mode waveguide would result in a more accurate prediction of the transmission coefficient. However, the minimal achievable SU-8 thickness is approximately 2 μm due to fabrication constraints, and multimode operation cannot be avoided.

2.2.3.2 Finite Element Model

A finite element simulation of the waveguide was performed in COMSOL Multiphysics software to obtain the vertical mode shapes. The RF perpendicular hybrid-mode waves module was used with the wavelength set to 635nm. The mode profiles were later exported from COMSOL into MATLAB and integrated numerically to obtain the transmission coefficient (Equation 2.7). As discussed previously, only the fundamental TE and TM modes are considered since they are expected to carry most of the power.

Figure 2.2 shows that the layer structure changes at different positions along the waveguide. It consists of one or more of the following layers: Si, SiO₂, SU-8, gold, water, and PDMS. The mode shape depends on the local waveguide cross section. The transmission coefficient is determined by the mode shapes at the tip of the cantilever and at the adjacent end of the output waveguide. Although the entire length of the cantilever is shown to be covered by gold in the schematic, the tip of the fabricated device is actually free of gold. A region of length $\approx 5 \mu\text{m}$ at the tip is left

without gold coating to make sure that facet is not obstructed (this is discussed further in Chapter 3). Therefore, the simulation of the cantilever mode does not include the gold coating.

Figure 2.5 shows the simulated electric field distribution of the fundamental TE mode (E_x^{00}) in the output waveguide and the cantilever. The waveguide geometry and material properties used for the simulation are also indicated in the plots. Note that this geometry is slightly different from the structure of the actual device in order to reduce the amount of computer memory needed for the simulation. For example, the waveguide width in Figure 2.5 is 10 μm , while the width of the fabricated waveguide is 20 μm . Since the cantilever width is much larger than the thickness (by a factor of 10), the lateral dimensions should not affect the vertical mode profile significantly. Also, the thickness of the Si here is limited to 4 μm , while the fabricated device has a 500 μm thick substrate. Since the light does not penetrate appreciably into the Si, the exact thickness of the substrate is insignificant.

The refractive indices of each material used in the simulation are values commonly reported in literature. The Si layer also has conductivity in addition to the refractive index. This is not the electrical conductivity; rather, it is an equivalent conductivity that accounts for the optical loss in the material. According to [122], the absorption coefficient of Si at 635 nm is $0.3 \mu\text{m}^{-1}$. It can be shown that this leads to a complex refractive index of $n = 3.42 - 0.015j$ and an equivalent conductivity of 2.7

kS/m. As a result of the Si absorbance⁴, the effective index of the waveguide modes is also complex and they have some propagation loss. This will be calculated in Section 2.2.3.6.

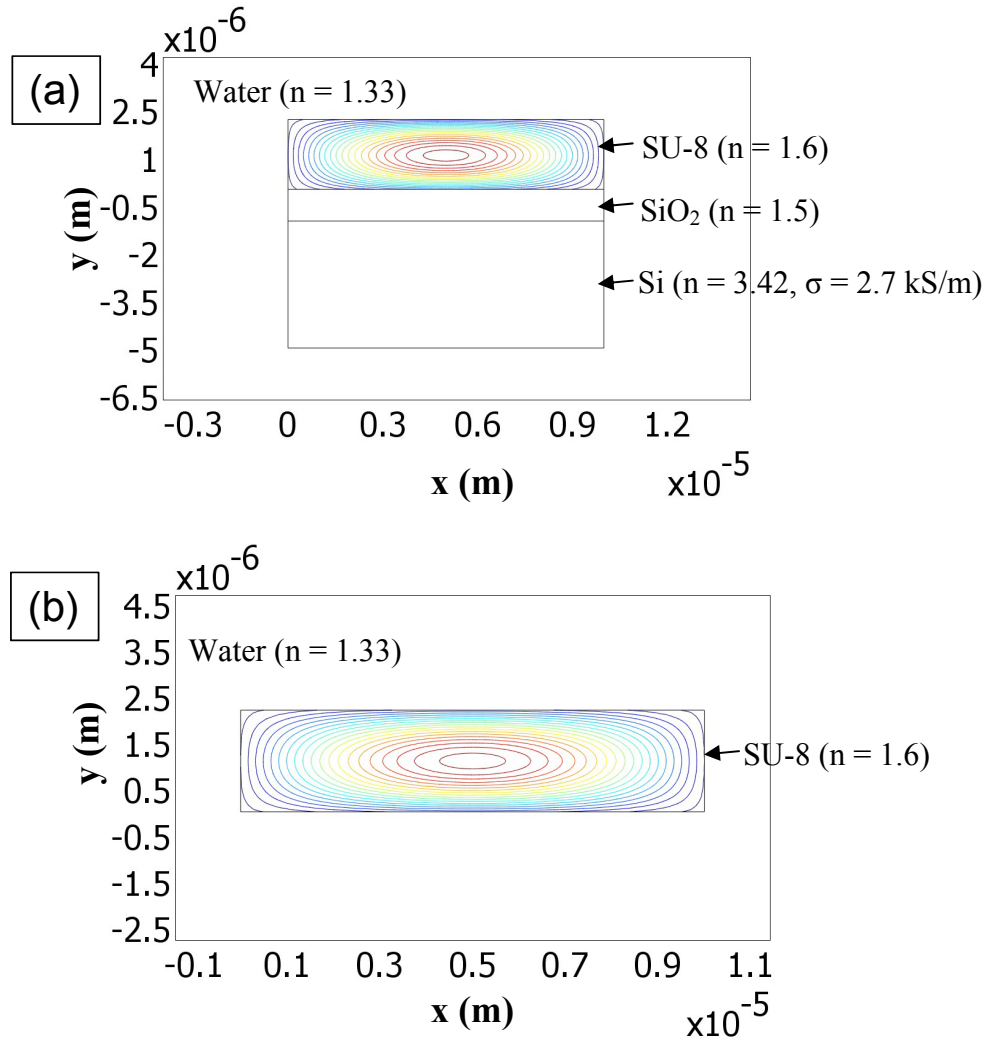


Figure 2.5: Contour plot of the electric field x-component of the fundamental TE mode in a) the output waveguide and b) the cantilever tip. Red corresponds to high values and blue to low values.

⁴ Water also has some optical absorbance. However, the section of waveguide covered by water is very short (only the length inside the microfluidic channel) and the total loss caused by water was found to be negligible even by a worst-case estimate.

The real parts of the mode indices found by the simulation (Figure 2.5a) are very close to those found by the planar waveguide model (Figure 2.4). The simulation yields $n_{eff} = 1.5946 - 1.5 \times 10^{-9}j$ and $n_{eff} = 1.5944 - 3.6 \times 10^{-9}j$ for the fundamental TE and TM modes respectively; the planar waveguide model yields $n_{eff} = 1.5947$ and $n_{eff} = 1.5946$ (the analytical model cannot account for loss mechanisms and gives only the real part of the index). This close agreement suggests that the lateral structure of the waveguide has little effect on the vertical mode profile.

The sections of the waveguide covered by PDMS ($n = 1.4$) and by gold were also simulated. The PDMS-covered part has essentially the same mode shapes and effective mode indices as the water-covered part (Figure 2.5a), and the results are not shown here. The gold covered-part also has similar mode shapes and real part of the effective index. However, the imaginary part of the index is considerably increased due to the attenuation of light in the metal. This leads to increased propagation loss, which will be discussed later in Section 2.2.3.6. Figure 2.6 shows the simulated electric field distribution of the fundamental TE mode in the gold-covered part of the cantilever. The complex refractive index of gold given in the figure was obtained from [123]. The simulation yields an effective mode index of $1.5939 - 4.2 \times 10^{-6}j$. Note that the gold layer thickness in the simulated geometry is increased to 100 nm in order to increase the element size and reduce the amount of computer memory required (the gold thickness in the fabricated device is only 10 nm). As a result, the simulation probably overestimates the complex part of the mode index.

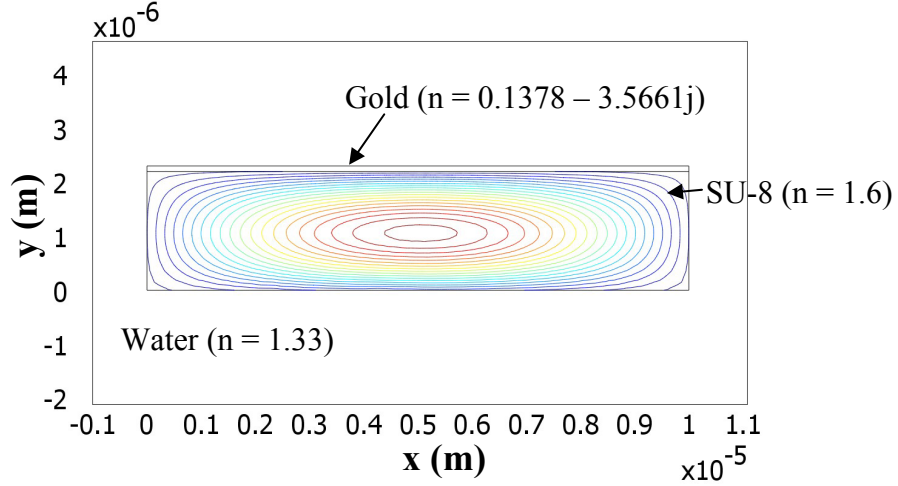


Figure 2.6: Contour plot of the electric field x-component of the fundamental TE mode in the gold-covered part of the cantilever. Red corresponds to high values and blue to low values.

The vertical modes shapes of the cantilever tip and output waveguide were exported from COMSOL and plotted in Figure 2.7. The figure shows the fundamental TE (E_x^{00}) and TM (E_y^{00}) modes are almost identical; therefore the transmission coefficient is the same for both polarizations. Furthermore, the figure shows that the modes can be approximated with a Gaussian given by $E = \exp(-(y - \mu)^2 / \omega_0^2)$. Here, $\mu = 1.1 \mu\text{m}$ is position of the waveguide's core center, and $\omega_0 = 0.9 \mu\text{m}$ is the beam waist. The Gaussian approximation allows the beam divergence and transmission coefficient (Equation 2.7) to be found analytically. Both the approximate analytical and exact numerical solutions are performed in the following sections, and the results are compared.

Although only the E^{00} mode are shown in Figure 2.7, the other E^{m0} modes were found to have almost the same vertical shape (as predicted by Equation 2.5 and Equation 2.6). Therefore, they have the same transmission coefficient. For the sake of simplicity, we refer to all the E^{m0} modes as fundamental. As discussed previously in

Section 2.2.3.1, the higher order modes (i.e. E^{mn} where $n > 0$) and their transmission coefficients are not analyzed here since E^{m0} carry most of the power.

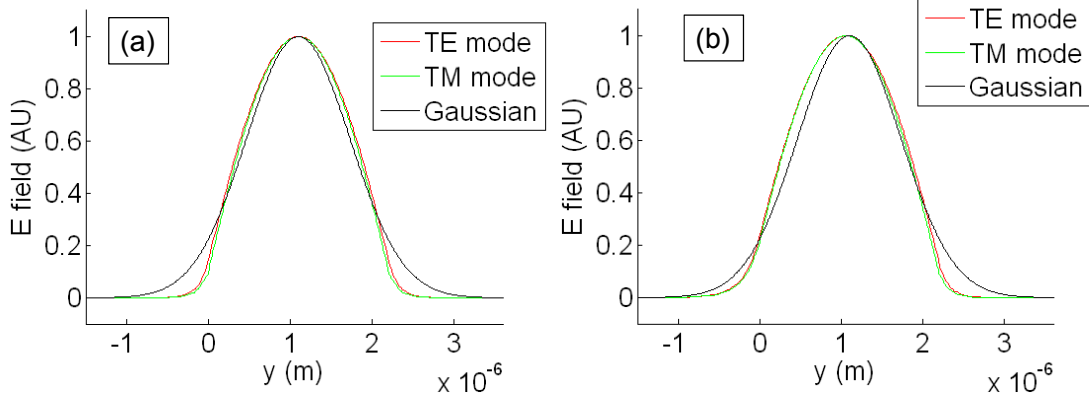


Figure 2.7: Vertical electric field distribution in a) cantilever tip and b) output waveguide.

2.2.3.3 Divergence in Gap

As the mode exits the cantilever tip and propagates to the output waveguide in unguided medium, it diverges (Figure 2.3). To find the transmission coefficient, it is necessary to solve for the broadened mode shape $G_2(y)$. Here, this is performed both by an analytical and a numerical method.

The analytical approach assumes that the mode shapes are approximately Gaussian (Figure 2.7). The propagation of a Gaussian beam is described by the following well-known equation [124]:

$$\text{Equation 2.9} \quad E(y, z) = E_0 \sqrt{\frac{2}{\pi}} \frac{\omega_0}{\omega(z)} \exp\left(-\frac{y^2}{\omega^2(z)}\right) \exp\left(-j\left[\phi_0 - \phi(z) + \frac{ky^2}{2R(z)}\right]\right)$$

The beam waist $\omega(z)$ is given by Equation 2.10, where ω_0 is the initial beam waist, i.e. the waist of the guided mode.

Equation 2.10
$$\omega(z) = \omega_0 \sqrt{1 + \left(\frac{z\lambda}{\pi\omega_0^2} \right)^2}$$

The numerical approach is based on Fourier optics and is implemented in a MATLAB program. It takes the exact mode shapes exported from COMSOL (Figure 2.7) rather than the Gaussian approximation. The method is described by Equation 2.11 and Equation 2.12, which were formulated by Chen *et al.* [125]. First, the Fourier transform of the mode profile is obtained. This essentially decomposes the beam into a set of uniform plane waves. To obtain a plane wave propagated by some distance z , it is multiplied by the phase factor $\exp(jkmz)$ where $k = 2\pi/\lambda$ and $m = (1 - p^2 - q^2)^{1/2}$. Then, the inverse Fourier transform is performed to obtain the propagated beam from its plane wave components (Equation 2.12).

Equation 2.11
$$A(p, q) = \left(\frac{k}{2\pi} \right)^2 \int \int_{-\infty}^{+\infty} E(x, y, 0) \exp[-jk(px + qy)] dx dy$$

Equation 2.12
$$E(x, y, z) = \int \int_{-\infty}^{+\infty} A(p, q) \exp(jkmz) \exp[jk(px + qy)] dp dq$$

2.2.3.4 Coupling Coefficient

The coupling coefficient as a function of cantilever displacement is found by performing the overlap integral in Equation 2.7 either analytically (Gaussian approximation) or numerically (exact mode shapes). The analytical solution is expanded in the next section to account for cantilever tilt in addition to vertical displacement.

The Gaussian approximations of the cantilever mode ($G_1(y)$) and the output waveguide mode ($G_3(y)$) have a beam waist ω_0 . The propagated cantilever mode

$(G_2(y))$ has a waist $B\omega_0$ where B is a broadening factor found by Equation 2.10.

Using these expressions, Equation 2.7 simplifies to:

$$\text{Equation 2.13} \quad C(t) = \frac{2B}{B^2 + 1} \exp\left(-\frac{2t^2}{\omega_0^2(1+B^2)}\right)$$

Therefore, the coupling function is a Gaussian with waist $\omega_0\sqrt{(1+B^2)}/2$. The divergence of the cantilever mode in the gap leads to broadening of the coupling function and therefore reducing the sensitivity to cantilever displacement. Therefore, it is desirable to use the shortest possible gap between the cantilever and the output waveguide. Due to the resolution of the lithography process, the minimal gap was found to be $\sim 2 \mu\text{m}$. Device with gaps of $2 \mu\text{m}$ or $4 \mu\text{m}$ were included on the mask (the latter leads to a higher fabrication yield at the expense of slightly reduced sensitivity). The theoretical waist of the coupling function is $0.9 \mu\text{m}$, $0.93 \mu\text{m}$, and $1.02 \mu\text{m}$ for gaps of $0 \mu\text{m}$, $2 \mu\text{m}$, and $4 \mu\text{m}$ respectively. Therefore, the effect of even the longer gaps is small.

The numerical solution uses the exact mode shapes $G_1(y)$ and $G_3(y)$ exported from COMSOL instead of the Gaussian approximations. The propagated mode $G_2(y)$ is obtained from the Fourier method described previously, and the coupling coefficient as a function of cantilever displacement (Equation 2.7) is calculated by numerical integration in MATLAB. Figure 2.8 and Figure 2.9 show the results for propagation gaps of $2 \mu\text{m}$ and $4 \mu\text{m}$ respectively. The results from the analytical method (Equation 2.13) are also included for comparison. The ‘‘a’’ plots show that the coupling function maxima found by the two methods differ somewhat. However, the ‘‘b’’ plots (normalized values) show that the shapes of the analytical and numerical

coupling functions are very close. The cantilever's sensitivity to displacement depends on the coupling profile rather than the peak value. Therefore, the Gaussian approximation can be legitimately used to model the cantilever's optical sensitivity.

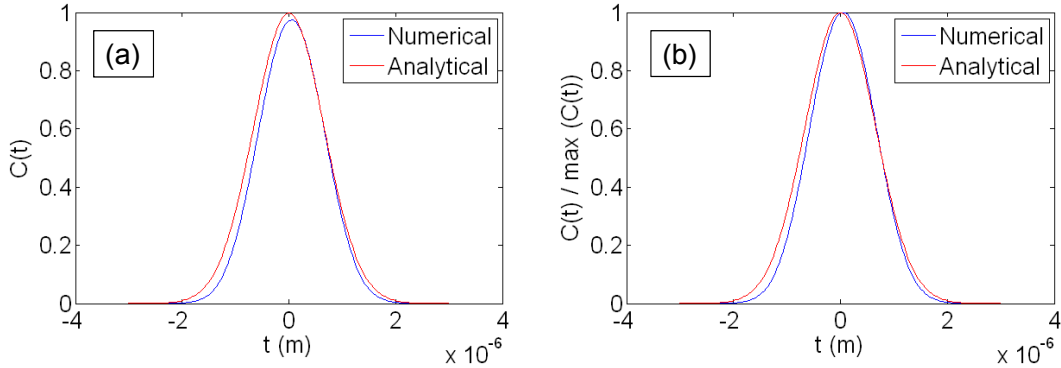


Figure 2.8: Theoretical coupling coefficient as a function of cantilever displacement for a gap of 2 μm . a) Raw values b) Normalized.

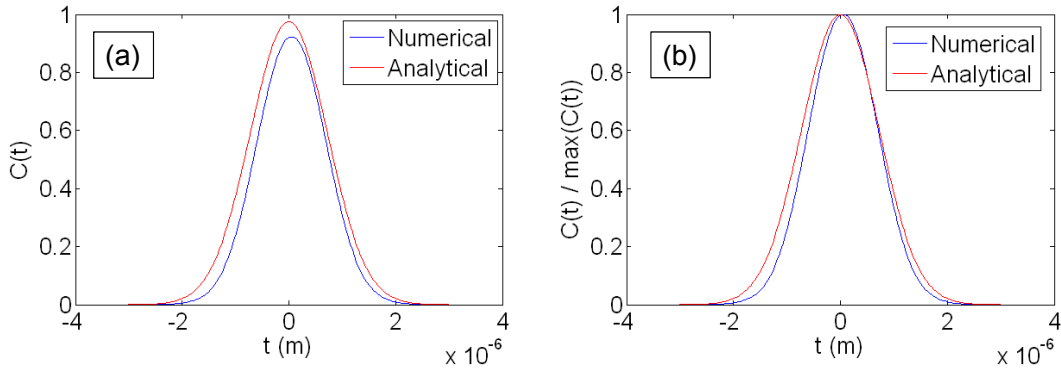


Figure 2.9: Theoretical coupling coefficient as a function of cantilever displacement for a gap of 4 μm . a) Raw values b) Normalized.

Note that the coupling coefficient is an even function of t . Therefore, the position of the cantilever cannot be uniquely determined from the output optical power. The same power change could result from either a positive or negative offset. For this reason, the cantilever in this design is constrained to be above the output waveguide (Figure 2.1), making t always positive. This eliminates the sign ambiguity; an increase in output power can be interpreted as downward cantilever displacement (decrease in t) and vice versa.

2.2.3.5 Effect of Tilt on Coupling Coefficient

The foregoing analysis assumes that the cantilever deflection causes only a vertical shift in the position of the mode. In reality, there is also an angular shift as illustrated in Figure 2.10 due to the cantilever bending. The tilt angle can be found from the profile of the cantilever (Equation 2.3) to be $\theta = \tan^{-1}(2t/L)$. This section analyzes the effect of tilt on the coupling coefficient. For the sake of simplicity, only the Gaussian (analytical) model is used here. The previous section showed that it gives essentially the same results as the numerical model for the no-tilt case.

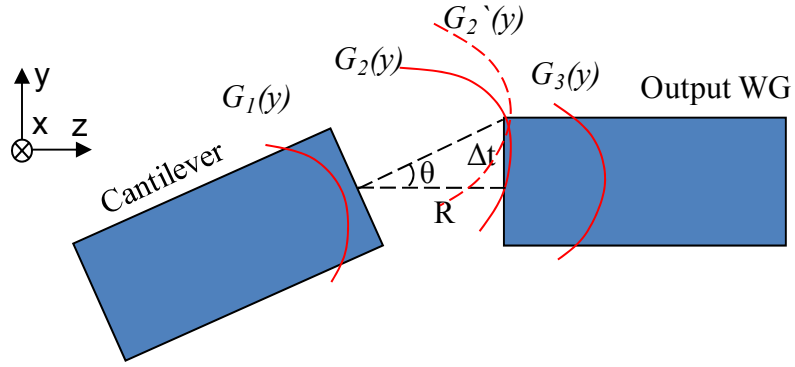


Figure 2.10: Schematic of light coupling from tilted cantilever into output waveguide.

The introduction of tilt has two main consequences. First, there is an additional vertical displacement of the mode $G_2(y)$. Inspection of Figure 2.10 reveals that this displacement is $\Delta t = R \tan(\theta)$, where R is the gap between the cantilever and the output waveguide. The total vertical displacement of the mode becomes $t' = t + \Delta t$. The second consequence of the tilt is that it adds a phase shift that depends on the y position. The mode becomes $G_2'(y) = G_2(y) \exp(-j\beta y \sin \theta)$ where β is the propagation constant in the unguided medium. The resulting coupling coefficient is given by Equation 2.14. Here ω_0 and B are the mode waist and broadening factor as defined previously, and C_0 is a constant. If we make the

substitution $g = \beta\omega_0^2 B^2 \sin(\theta)$ and normalize the coupling coefficient to its peak value, it simplifies to Equation 2.15.

$$\text{Equation 2.14} \quad C(t') = C_0 \int_{-\infty}^{\infty} \exp\left(-\frac{(y-t')^2}{\omega_0^2 B^2}\right) \exp(-j\beta y \sin \theta) \exp\left(-\frac{y^2}{\omega_0^2}\right) dy$$

$$\text{Equation 2.15} \quad C(t') = \exp\left(-2 \frac{t'^2 - \left(\frac{2t' - jg}{2\sqrt{1+B^2}}\right)^2}{\omega_0^2 B^2}\right)$$

Equation 2.11 was evaluated in MATLAB and plotted in Figure 2.11 for the two different values of the propagation gap and a cantilever length of 100 μm . The results of the no-tilt calculation are included for comparison. The effect of the tilt is more apparent in the case of the larger gap. However, it can be concluded that in both cases the tilt does not change the coupling coefficient appreciably. For this reason, it will not be considered in subsequent optical sensitivity calculations.

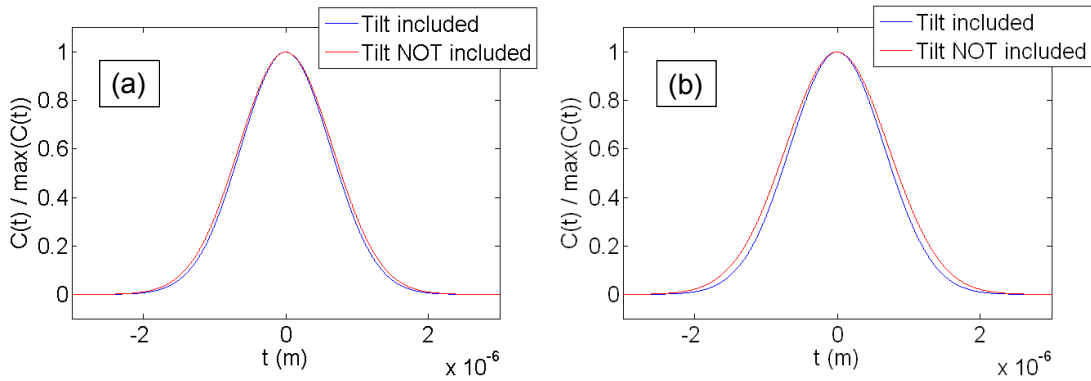


Figure 2.11: Theoretical coupling coefficient for a cantilever length of 100 μm and propagation gap of a) 2 μm b) 4 μm .

2.2.3.6 Propagation Loss

The total power arriving at the device output must be above the noise threshold of the photodetector, which is on the order of several pW. The laser power is approximately 1mW. Therefore, a total loss of 90 dB can be tolerated, including on-chip propagation loss and fiber-to-chip coupling loss.

The propagation loss is estimated here using the results of the finite element modal analysis described earlier. This model only accounts for one loss mechanism: absorbance of the light in the silicon or the gold layer. The actual propagation loss may be dominated by surface roughness and waveguide defects. However the model cannot take these effects into account and assumes that the waveguides are perfectly smooth. Nevertheless, the results give insight into the required thickness of the SiO₂ bottom cladding layer used to isolate the SU-8 core from the lossy Si substrate.

The COMSOL finite element simulation of the waveguide yields a complex mode index. The attenuation coefficient is given by Equation 2.16 where k is the imaginary part of the index and λ_0 is the free space wavelength (635 nm). The propagation loss in dB/cm can be found from Equation 2.17.

$$\text{Equation 2.16} \quad \alpha = \frac{4\pi k}{\lambda_0}$$

$$\text{Equation 2.17} \quad \alpha_{dB} = \frac{\alpha \log_{10} e}{10}$$

For a SiO₂ layer thickness of 200 nm, the simulation gives $k = 4.2 \times 10^{-5}$ and propagation loss of 36 dB/cm for the fundamental TE mode. This value is clearly too high, considering that the total waveguide length (input and output) is 2 cm and that

there are many other loss mechanisms. Increasing the SiO₂ thickness to 1 μm gives $k = 1.5 \times 10^{-9}$ and propagation loss of only 0.0013 dB/cm (the mode was shown in Figure 2.5a). In this case, the waveguide is completely isolated from the Si substrate and there is no need to increase the cladding thickness further. As discussed previously, the actual propagation loss may be much higher due to waveguide roughness but that should not depend on cladding thickness. The gold-coated section of the waveguide (Figure 2.5b) has $k = 4.2 \times 10^{-6}$ and corresponding theoretical propagation loss of 3.6 dB/cm. However, this region is quite short compared to the waveguide length (200 μm compared to 1 cm) and should have a small contribution to the total loss.

The other sources of optical loss in the device such as fiber-to-chip coupling and modal mismatch between different parts of the waveguide are not modeled here. The reason for this is that there are no parameters in the device design that can be readily adjusted to reduce such losses. The total optical loss is measured experimentally and reported in Chapter 4.

2.2.3.7 Sensitivity and Signal to Noise Ratio

The optical sensitivity of the cantilever is the change in coupling coefficient per unit tip displacement. For small displacements, this quantity is equal to the derivative of $C(t)$. The actual measured change in output power depends on the optical loss through the device, which can vary considerably (as discussed in the previous section). However, the shape of the sensitivity helps determine the optimal initial tip

height of the cantilever without knowing the loss. The beam curvature and length can be controlled during fabrication to obtain that height.

Figure 2.12 shows the normalized coupling coefficient and the absolute value of its derivative. The sensitivity has a maximum near $t = 700 \text{ nm}$. Intuition suggests that the cantilever's initial position should be at the sensitivity peak. However, the measurement noise also increases with output power. Therefore, the optimal initial position is not necessarily the sensitivity maximum and depends on the sources of noise.

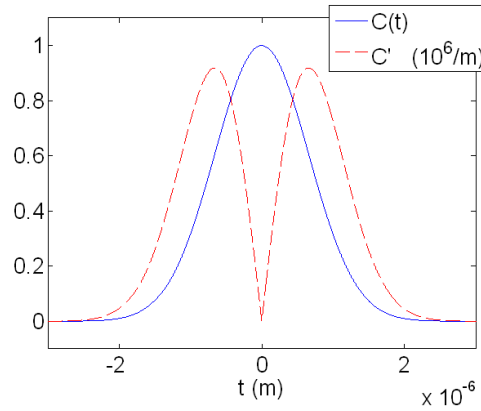


Figure 2.12: Theoretical coupling coefficient and sensitivity for a cantilever with $2 \mu\text{m}$ propagation gap (based on the Gaussian model without tilt).

In the work by Zinoviev et al., the main source of noise is considered to be shot noise in the photodetector [32]. In the present dissertation, the optical cantilever operates in the static mode and the detector has low bandwidth (1 Hz); consequently, the detector noise is very low. Instead, the main source of noise is the mechanical drift of the XYZ positioning stages that hold the fibers facing the input and output waveguides. The power at the detector can be expressed by Equation 2.18, where T is a fiber-to-waveguide coupling coefficient combined for both input and output, and the coefficient α accounts for the on-chip propagation loss. Changes in output power are

caused either by the cantilever motion or by fiber-to-waveguide drift since P_{in} and α are fixed (Equation 2.19). This shows that decreasing the coupling coefficient $C(t)$ also decreases the drift noise. The signal to noise ratio (SNR) is approximated by Equation 2.20, assuming that the fiber drift is the dominant source of noise. In that case, SNR is proportional to C'/C .

Equation 2.18 $P_{out} = P_{in}TC(t)\alpha$

Equation 2.19 $\Delta P_{out} = \Delta P_{cant} + \Delta P_{drift} = P_{in}\Delta C(t)T\alpha + P_{in}C(t)\Delta T\alpha$

Equation 2.20 $SNR \approx \frac{\Delta P_{cant}}{\Delta P_{drift}} = \frac{\Delta C}{C(t)} \frac{T}{\Delta T} = \left(\frac{dC}{dt} \frac{1}{C(t)} \right) \frac{T}{\Delta T} \Delta t$

The ratio C'/C is plotted in Figure 2.13 for a cantilever with 2 μm propagation gap. The same model is used here to calculate the coupling coefficient as in Figure 2.13, but only values for $t > 0$ are shown. The plotted ratio C'/C increases monotonically with cantilever tip height, while C (and the output power) decreases.

Therefore, SNR can be improved by increasing the height until drift noise becomes comparable to detector noise. The optimal offset depends on the contributions of each noise source and has not been determined exactly. I chose a target cantilever offset of 2.2 μm . Experimentally, I found that increasing the offset beyond 2.5 μm decreases the displacement signal too much, and the effects of stray light coupling and detector noise become significant. As explained in Section 2.2, the offset of 2.2 μm corresponds to a cantilever length of 140 μm (assuming curvature of 0.23 mm^{-1}).

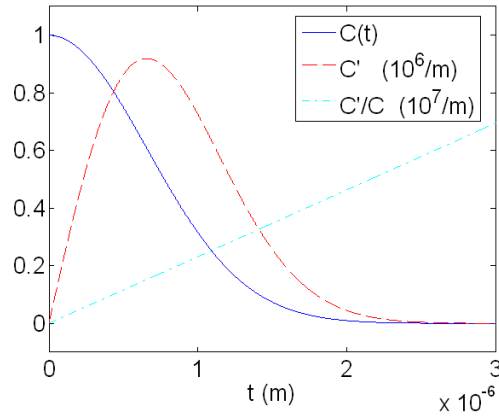


Figure 2.13: Theoretical coupling coefficient, sensitivity, and ratio of the two for a cantilever with 2 μm propagation gap (based on the Gaussian model without tilt).

2.2.4 Choice of Dimensions and Mask Layout

The final device dimensions are shown in Table 2.3. Critical parameters chosen by modeling or by fabrication of test structures are bolded, and their respective design considerations are listed. The rest of the parameters are not critical to the device performance. They did not require optimization and were chosen by intuition.

The device is fabricated with 4 lithography masks. These are the SU-8 mask, the release mask (defines the cantilever length), the Au mask (defines the gold pattern on top of the waveguide), and the PDMS molding masks (define the channel patterns). Representative layouts are shown in Chapter 3.

Note that the fabrication process developed here (Chapter 3) allows for adjustment of the cantilever length while using the same mask set. This is accomplished by performing a double exposure with the release mask and shifting the mask between exposures. The ability to change length is essential. It was shown before that the initial position of the cantilever greatly impacts sensitivity (Figure 2.13), and that it depends on the beam length and curvature (Equation 2.4). Since the curvature is difficult to control, the cantilever position can be fine-tuned by changing

the length. During the course of this research, beams with length ranging from 70 μm to 140 μm were fabricated.

Table 2.3: Dimensions of waveguide cantilever device. Parameters critical to the performance are listed in bold.

Parameter	Value	Value set by	Considerations
Cantilever length	70 - 140 μm	Release mask shifting	Optical/mechanical sensitivity modeling
Cantilever/waveguide width	20 μm	SU-8 mask	
Cantilever-to-waveguide gap	2 or 4 μm	SU-8 mask	Optical sensitivity modeling
Length of gold coating	200 μm	Gold mask	
Layer thickness		Fabrication process	
- SU-8	2.2 μm		Optical/mechanical sensitivity modeling
- Au	15 nm		Beam curvature experiments (Chapter 3)
- SiO₂	1 μm		Propagation loss modeling
- PDMS	2 - 5 mm		
Fluidic channel		PDMS molding mask	
- length	1 - 2 cm		
- width	500 μm		
- depth	100 μm		
Spacing between waveguides	1 mm	SU-8 mask	
Length of waveguides	1 cm	All masks, cleaving	
Dimensions of die	2 cm x 2 cm	All masks, cleaving	
Number of die per wafer	6	All masks	
Number of cantilevers per die	8	All masks	
Waveguide tether width	2	SU-8 mask	

2.3 Interferometric Cantilever

2.3.1 Device Structure

The structure of the interferometric cantilever is very similar to that of the waveguide device described above. It also consists of a curved gold-coated SU-8 beam on a Si substrate as shown in Figure 2.14. The same fabrication process is used to control the residual stress gradient and curvature as in the case of the waveguide cantilever. Due to the small gold thickness, the cantilever is transparent to visible light. This allows the formation of an interference pattern as explained later.

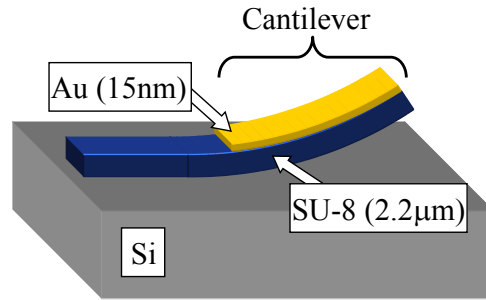


Figure 2.14: Schematic (3D) of an interferometric cantilever before the addition of the microfluidic channel. The layer thicknesses are labeled.

There are only two differences between the structure of the interferometric cantilever and that of the device described in Section 2.2. First, the interferometric cantilever does not have waveguides. For this reason, the bottom SiO_2 cladding layer is eliminated (Figure 2.15a), and the SU-8 layout is modified (Figure 2.15b). Second, each interferometric cantilever on the chip is embedded inside an individual fluidic channel that runs parallel to the cantilever (Figure 2.15c). This allows each device to be exposed to a different liquid sample simultaneously.

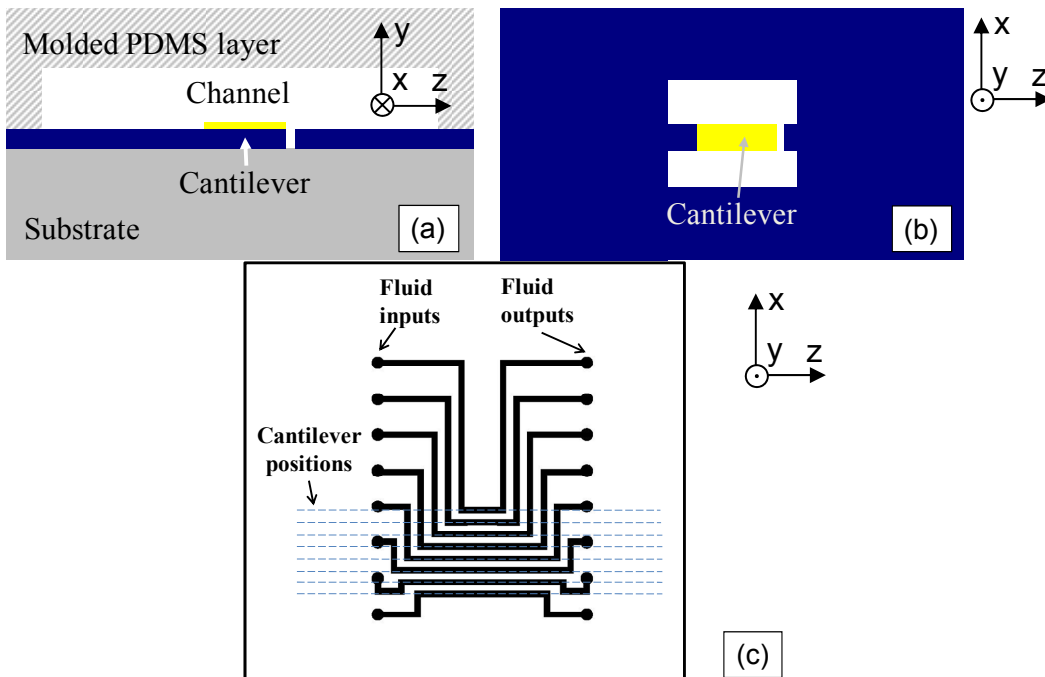


Figure 2.15: a) Cross section of interferometric cantilever inside microfluidic channel. b) Top down view of SU-8 layout. c) Top down view of fluid channels layout. The same XYZ coordinate system is used as for the waveguide cantilever.

Due to the similarities between the two devices, most of the lithographic masks for the waveguide cantilever are also used for fabrication of the interferometric cantilever. An additional SU-8 mask is introduced to modify the SU-8 layout, and the PDMS molding mask used to define the fluidic channels is replaced.

2.3.2 Theory of Operation

As in the case of the waveguide-based device discussed previously, the interferometric cantilever deflects from its initial position due to the attachment of analytes. Its mechanical sensitivity, i.e. the displacement per unit surface stress, is the same as that of the waveguide cantilever and can be found using the equations in Section 2.2.2. However, the method of measuring the displacement is quite different, and it is explained next.

Figure 2.16 illustrates the formation of the interference pattern when the cantilever is imaged with an optical microscope. An incident light beam from the microscope illuminator is partly reflected by the cantilever top and bottom surfaces, producing a beam with intensity I_1 . The incident beam also passes through the cantilever and reflects off the substrate, producing a beam with intensity I_2 .

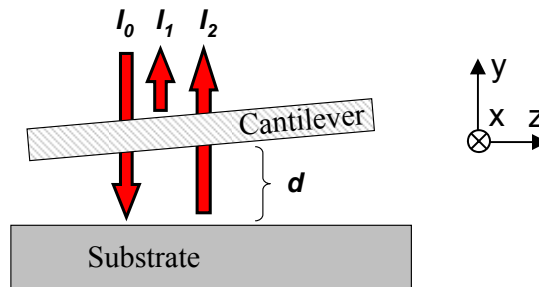


Figure 2.16: Interference cavity formed between transparent cantilever and reflective substrate.

The phase difference between beams **1** and **2** is given by $\phi = 4\pi dn/\lambda + \phi_o$, where d is the distance between the cantilever and the substrate, λ is the optical wavelength,

n is the refractive index, and ϕ_o is a constant. The combined intensity of the reflected beams is given by Equation 2.21.

$$\text{Equation 2.21} \quad I_{refl} = I_1 + I_2 + 2\sqrt{I_1 I_2} \cos(\phi) = I_1 + I_2 + 2\sqrt{I_1 I_2} \cos\left(\frac{4\pi d n}{\lambda} + \phi_o\right)$$

Since the cantilever has an upward slope, the distance d increases continuously at points along the cantilever. Therefore, I_{refl} goes through consecutive interference maxima and minima, producing an interference pattern along the cantilever as shown in Figure 2.17. Here, each dark band is an interference minimum, and each bright band is an interference maximum. The width of the bands changes along the cantilever due to its increasing slope. The cantilever slope is largest near the tip; hence, the the bands are most closely spaced there.

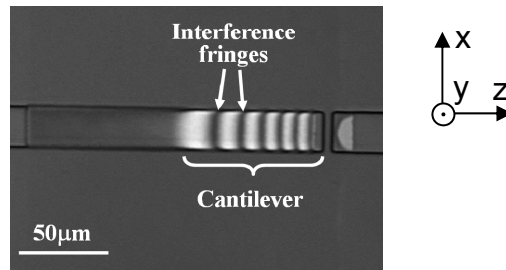


Figure 2.17: Microscope image of an interferometric cantilever immersed in water.

In order to obtain high interference contrast, the microscope light source must have a narrow spectral linewidth. White light sources would create a continuum of interference patterns, flattening the image intensity. In this work, we use a solid state laser with nominal wavelength of 660nm as the microscope light source. The laser beam is spatially decohered as described in Chapter 5 to avoid producing a speckle pattern on the image. Sources with somewhat broader spectra, such as LEDs and filtered incandescent lightbulbs, also produce visible interference patterns. However, their interference contrast is lower than the one obtained with the laser.

Changes in the interference pattern can be used to find the cantilever vertical displacement upon detection of a sample. Counting the number of fringes (either minima or maxima) gives a rough estimate of the cantilever tip height. Equation 2.21 suggests that each fringe corresponds to an elevation of $\lambda/2n = 248$ nm, assuming that $n = 1.33$ (water) and $\lambda = 660$ nm. The tip height is approximately equal to the number of fringes multiplied by 248 nm; similarly, large displacements can be estimated by multiplying the change in number of fringes by 248 nm. The maximum measurement error corresponds to ± 1 fringe.

A more precise determination of the displacement requires a model of the expected cantilever height profile. Cantilevers bent due to residual stress gradient or surface stress should have a parabolic profile of the form $d(z) = a(z-z_0)^2$ [118], where z_0 is the position of the cantilever base. Combining this expression with Equation 2.21 suggests that the intensity along the cantilever has the form given by Equation 2.22.

Equation 2.22 $I_{refl}(z) = A + B \cos(Cz^2 + Dz + E)$

Figure 2.18 shows the measured image intensity along a cantilever and a least squares curve fit based on Equation 2.22. Overall, the fit agrees well with the measured data ($R^2 = 0.94$), suggesting that the cantilever indeed has a parabolic profile. The intensity envelope of the measured data is affected by the nonuniformity of the microscope illumination, and it deviates considerably from the fit (which assumes uniform illumination). However, the spacing between the interference fringes is determined mainly by the cantilever height profile and is consistent with the fit.

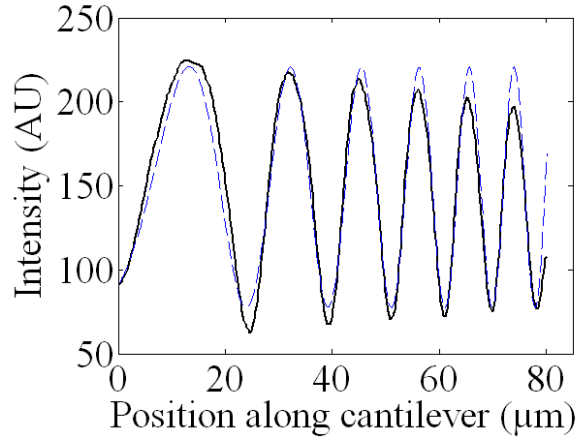


Figure 2.18: Measured intensity profile from a cantilever image (solid line) and curve fit (dashed line). The fit has $R^2 = 0.94$.

Theoretically, curve fitting can be used for extracting cantilever displacement with much better resolution than the simple fringe counting. However, in practice it has two drawbacks. First, it is difficult to automate because it requires an initial guess. Second, it can introduce appreciable error due to changes in the intensity envelopes of image taken before and after sample detection. I developed another method for measuring small displacements which is more suitable for automation and less sensitive to nonuniform illumination. It is based on measuring the horizontal fringe shift that occurs when the cantilever is vertically displaced.

Figure 2.19 illustrates a cantilever with an initial height profile $C_1(z)$ that undergoes displacement into final profile $C_2(z)$. The horizontal dashed lines represent heights that fulfill the phase conditions for interference fringes. The schematic shows that the downward displacement of the cantilever causes the fringes on the microscope image to move to the right. For example, the fringe of order m moves horizontally by Δz . The vertical displacement labeled Δd_1 is equal to $\Delta z \cdot \tan(\theta)$. This expression is obtained by considering the right triangle formed by the three red lines

in Figure 2.19. Assuming the cantilever has a parabolic height profile and the height is much smaller than its length (L), the displacement at the tip is given by Equation 2.23.

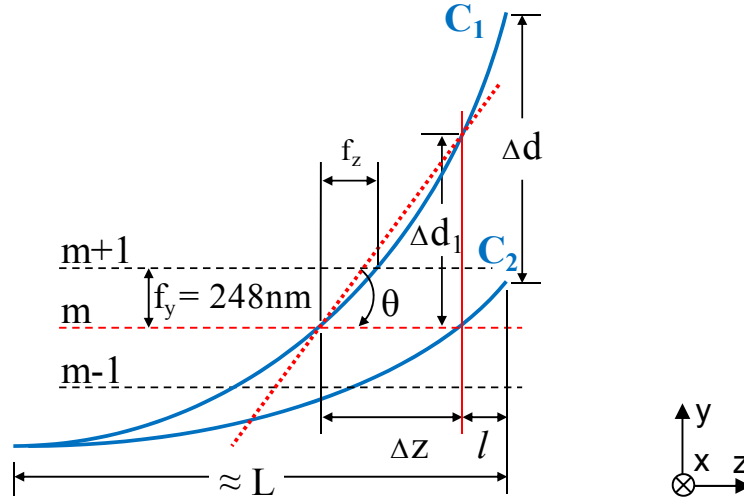


Figure 2.19: Geometry used for calculating cantilever displacement from horizontal fringe shift

$$\text{Equation 2.23} \quad \Delta d = \Delta d_1 \frac{L^2}{(L-l)^2} = \Delta z \tan(\theta) \frac{L^2}{(L-l)^2} \approx \Delta z \frac{f_y}{f_z} \frac{L^2}{(L-l)^2}$$

The fringe shift (Δz) and the distance of the fringe from the cantilever tip (l) are measured from the initial and final images of the cantilever by an automated algorithm as described later. The local slope $\tan(\theta)$ cannot be measured directly, but it is approximated by the ratio of the vertical spacing to the horizontal spacing between the fringes on the initial cantilever image, i.e. $\tan(\theta) \approx f_y/f_z$. The error resulting from this approximation will be addressed in Section 2.3.4. Therefore, the cantilever vertical displacement can be determined based on parameters measured from the microscope images.

2.3.3 Image Processing Algorithm

To enable rapid measurement of cantilever displacement from the interference images, an automated procedure is necessary for extracting the fringe shift. This is performed by a custom MATLAB program with a graphical user interface. The user selects two regions of interest (ROI) with the mouse on each image as shown in Figure 2.20. ROI 1 and 2 contain the fringe whose shift is to be found. An interference minimum is selected here (dark band), but a maximum can also be used. We know that the fringe in ROI 2 is the shifted version of that in ROI 1 because they are both fifth order (they are fifth to the right from the cantilever base). ROI 3 contains an adjacent fringe, which serves for finding the fringe spacing and cantilever slope in the initial image. Note that the fringe in ROI 3 is no longer present in the final image since it has moved too far to the right. One can think of it as “falling off” the cantilever. ROI 4 is an alignment feature which enables registration of the images. Although the ROIs are defined manually by the user, the procedure does not require precise selection and takes only a few seconds. The high-precision measurement is achieved by the algorithm described next.

First, the final image is registered to the initial image since the cantilever may be in a different position within each image due to microscope stage translation. The registration is performed by a well-known method based on the normalized cross-correlation function [126]. Briefly, the coordinates of maximum cross-correlation of ROI 4 (alignment feature) with the initial image are found. This gives the offset that must be applied to the final image to align it with the initial image. The image registration approach is also used for measuring the distance between fringes. The

peak cross-correlation between ROI 1 and ROI 2 is found, yielding the fringe shift from initial to final image (Δz). Similarly, the peak cross-correlation between ROI 1 and ROI 3 gives the fringe spacing in the initial image (f_z). Finally, the position of the fringe in ROI 2 is found by a peak-detection function and is used to determine the distance of the fringe from the cantilever tip (l). The described algorithm provides all the parameters needed in Equation 2.23 to calculate cantilever displacement.

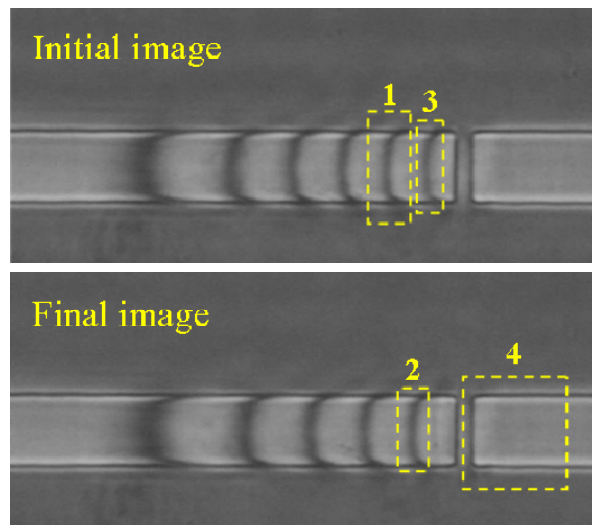


Figure 2.20: Initial and final images of a cantilever displaced downward due to change in solution pH (imaged in liquid). The interference fringes move to the right. The regions of interest 1-4 are selected by the user with the mouse.

2.3.4 Measurement Error

The error in the interferometric measurements of cantilever displacement can be divided into random and systematic components. The random error is due to uncontrollable variations in the measurement setup, such as small changes in microscope focusing and sample positioning, camera noise, and wavelength fluctuations. The systematic error is mainly due to the slope approximation used in Equation 2.23. The random error affects the precision of measurements, and the systematic error affects the accuracy.

2.3.4.1 Random Error (Precision)

We assume that the random error caused by laser wavelength fluctuations is negligible (this assumption is justified later in Section 5.4). This effectively means that the vertical fringe spacing f_y is fixed. By taking the partial derivatives of the expression in Equation 2.23 with respect to Δz , f_z , and l , it can be shown that the error in Δz contributes most to the displacement error. The measurement error for these 3 variables is similar, but the partial derivative with respect to Δz is much larger than the other two. Therefore, the random error in cantilever displacement is mainly caused by fringe shift measurement error.

One source of Δz error is the quantization of the image. Fringe shifts are detected in increments of 1 pixel. Therefore, there is a measurement uncertainty of ± 0.5 pixels. Another source of Δz error is the change in microscope focus, which can slightly stretch the image and create an apparent fringe shift. Finally, translation of the microscope stage also causes error in Δz . Although the final image is registered to the initial image in software, the illumination of the sample is not perfectly uniform. This means that motion of the stage changes the intensity envelope of the interference pattern and somewhat affects the fringe shift measurement. The effects of this error will be investigated in Section 5.4.

2.3.4.2 Systematic Error (Accuracy)

The largest source of systematic error in the interferometric displacement measurements is the slope approximation in Equation 2.23. The amount of error depends on the cantilever profile, the position of the fringe being tracked, and the final displacement. There is no convenient closed form expression for this error, so I

calculated it for a representative cantilever geometry. Figure 2.21 shows the results for three different types of slope approximations. The dashed line is obtained by using the spacing between the fringe being tracked and its lower order neighbor to find the slope (i.e. fringes $m-1$ and m in Figure 2.19). This leads to a considerable underestimate of the displacement. The solid line is obtained by taking the spacing between the fringe being tracked and its higher order neighbor (m and $m+1$). This slope approximation is a significant improvement over the previous case, and it was the one used for all the measurements reported here. It leads to an overestimate for small displacements and an underestimate for larger displacements; the error is less than 6% of the displacement throughout the range shown.

The dotted line in Figure 2.21 represents a further improvement in slope approximation, which reduces the error to less than 1.6% of displacement. Here, the initial cantilever curvature is estimated by counting the number of interference fringes (i.e. estimating the tip height). This curvature and the spacing between fringe m and its closest neighbors can be used to calculate the slope anywhere on the cantilever. The measured fringe shift is divided into small increments; the displacement is then calculated as a sum of the products of these increments with the local slope. Using this method, the measurement accuracy is greatly increased even for a poor curvature estimate. The result in Figure 2.21 is based on a worst-case error of 248 nm in the fringe counting estimate of tip height. This result can be improved further by a better curvature estimate, which is possible with curve fitting as discussed in Section 2.3.2.

Although the third slope approximation method is the most accurate, it requires more user input than the others: measuring one more fringe spacing and counting the

number of fringes. This somewhat slows down the image processing. For this reason, I chose the second method for all of the experiments reported in Chapter 5.

The accuracy of displacement measurements is slightly affected by other factors in addition to the slope approximation, such as the accuracy of the laser wavelength and the refractive index of the liquid. In our calculations, we assume that the free space wavelength is 660nm (datasheet value) and the refractive index is 1.33 (textbook value for water). To minimize the systematic error, these values can be measured independently with relatively common laboratory instruments. This is particularly important if the refractive index difference between the sample and the reference liquid is large.

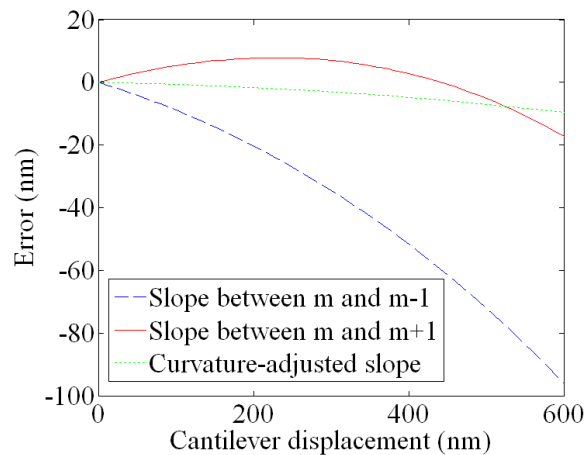


Figure 2.21: Estimated measurement error resulting from three different types of slope approximation.

2.3.5 Choice of Dimensions

The choice of dimensions of the interferometric cantilever is guided by many of the same considerations as the waveguide cantilever device described in Section 2.2.4. The main difference is that it does not have a coupling coefficient as a function of displacement and an optical sensitivity. Instead, the preferred initial position of the

cantilever is determined by the density of the interference pattern, which depends on the tip slope. If the cantilever is too flat, the interference fringes are broad and difficult to locate. If it is too steep, the interference fringes are closely spaced and the resolution of displacement measurements is reduced (in addition, the cantilever may extend beyond the depth of focus of the microscope). Initial experiments suggested that slopes between 0.02 and 0.04 are optimal. The tip slope is can be expressed from Equation 2.4 as kL , where k is the curvature and L is the cantilever length. The typical value of k is on the order of 0.3 mm^{-1} (Chapter 3); therefore lengths ranging from 70 to $140 \text{ }\mu\text{m}$ can be used.

Due to the design similarities between the two types of devices, most of the waveguide cantilever lithographic masks were re-used for the interferometric cantilever. Therefore, the dimensions listed in Table 2.3 are common to both devices. As explained previously in Section 2.2.4, the cantilever length is set by the alignment of one of the masks and can be varied between fabrication runs.

2.4 Summary

This chapter has presented the theory behind the optical cantilever and the interferometric cantilever sensors. The principle of operation was explained, and the governing equations were given. The mechanical sensitivity, the coupling coefficient as a function of displacement, the optical sensitivity, the signal-to-noise ratio, and the expected measurement error for the devices were discussed. Based on this analysis, the final choices of device dimensions were explained.

Chapter 3: Fabrication

3.1 Introduction

This chapter presents the fabrication and packaging procedures for both the interferometric cantilever and the waveguide cantilever. As discussed in the previous chapter, the structures of the two devices share many similarities. For this reason, their fabrication processes are almost the same and are described concurrently here. The bulk of the fabrication development consisted of minimizing the residual stress gradient in order to reduce the cantilever curvature. The curvature plays a significant role in the operation of both types of devices. An acceptable stress gradient was obtained after trying two different materials and tuning the processing conditions empirically.

3.2 Choice of Materials

The material used for fabricating the cantilevers must meet several requirements. First, it must be transparent to in order to enable low optical losses. Second, its refractive index must be higher than that of the cladding to enable waveguiding by total internal reflection (this requirement applies to the waveguide-based device only). Third, it must have a low residual stress gradient to allow for small beam curvature as discussed in Chapter 2. There are very few materials compatible with MEMS fabrication that satisfy these requirements. Considering the available fabrication facilities at UMD at the time of this research, there were only two possibilities: Si_3N_4 and the polymer SU-8.

My original choice of material was Si_3N_4 . It is used commonly for the fabrication of both cantilevers [85] and waveguides [127]. After fabrication of test devices, however, I found out that the Si_3N_4 properties vary considerably depending on its composition. There are essentially two types of nitride: stoichiometric and Si rich. The former has a ratio of Si to N as given by the chemical formula (3 to 4); the latter has a slightly higher content of Si. The stoichiometric nitride is typically used for waveguides, while the Si-rich composition is preferred for mechanical structures.

Stoichiometric Si_3N_4 has very low optical loss, and I successfully fabricated test waveguides from it. Unfortunately, its residual stress gradient is high and leads to large upward cantilever curvature. Figure 3.1 shows a side view of a beam of stoichiometric Si_3N_4 . This image was obtained by breaking off a test cantilever with a micropositioning probe and turning it on its side. The radius of curvature was determined to be $470\ \mu\text{m}$ by drawing a circle concentric with the cantilever. This corresponds to a curvature of $2.1\ \text{mm}^{-1}$ and stress gradient of $760\ \text{TPa/m}$ (from Equation 2.3), which agrees with values reported in literature [128]. This excessive curvature would cause a $100\ \mu\text{m}$ long cantilever to be offset by approximately $11\ \mu\text{m}$ from the output waveguide, preventing any light from coupling to the output.

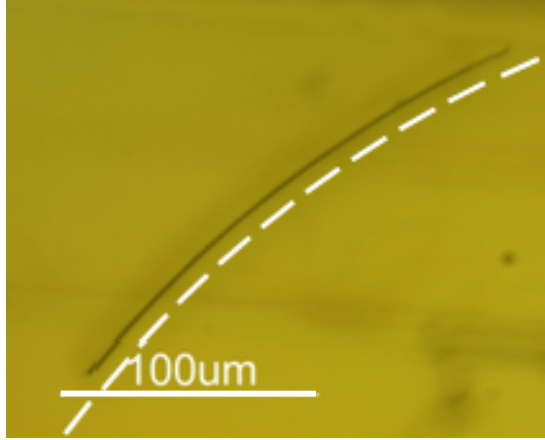


Figure 3.1: Side view micrograph of a stoichiometric Si_3N_4 test beam. The dashed curve parallel to the cantilever is part of a circle with radius $470 \mu\text{m}$.

I attempted to reduce the curvature of the stoichiometric Si_3N_4 by depositing a layer of SiO_2 on top (using e-beam evaporation). This material has compressive surface stress; it should, in principle, cancel the stress gradient in the Si_3N_4 if the correct thickness is chosen. However, in practice, the required thickness could not be found exactly due to large variations of the stress between fabrication runs. As a result, the curvature was reduced only slightly and remained an order of magnitude above the acceptable value.

Si-rich nitride has very low residual stress and stress gradient. While the typical residual stress value for the stoichiometric material is on the order of 1.2 GPa [127, 128], it can be reduced to only 30 MPa for the Si-rich composition [129]. Figure 3.2 shows a side view of a beam made from Si-rich nitride (this image was obtained using the same method as in Figure 3.1). The dashed line indicates that the beam is almost perfectly straight and this material meets the requirement for low curvature. However, the test waveguides fabricated from Si-rich nitride could not propagate any measurable light. This result is consistent with reports of the high optical extinction

coefficient of the material in the visible range [130]. Therefore, the Si-rich composition fails to meet the requirement for low optical loss.

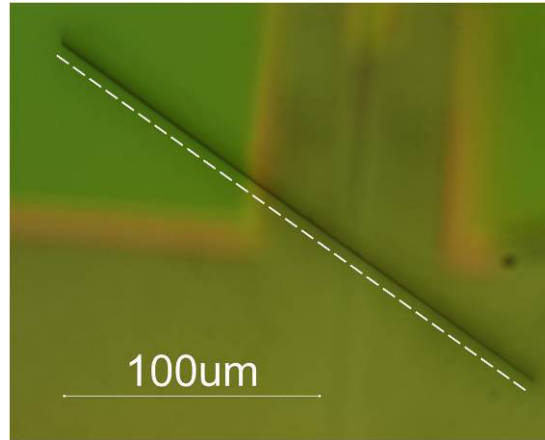


Figure 3.2: Side view micrograph of a Si-rich SiN test beam. A straight dashed line is drawn parallel to the cantilever.

It may be possible to fine tune the composition of the Si_3N_4 to achieve an acceptable balance between optical and mechanical properties. However, that requires a CVD tool (chemical vapor deposition) in order to perform multiple trial-and-error nitride depositions. At the time of this research, such a tool was not available at UMD. The Si_3N_4 films were deposited by external vendors; therefore, it would be prohibitively slow and expensive to obtain multiple different nitride compositions.

The polymer SU-8 was found to be a much better choice for fabricating both types of devices. It is reported to have a very low stress gradient on the order of 14 MPa/m [131] compared to 760 TPa/m measured for stoichiometric Si_3N_4 above. In addition, it is highly transparent and appropriate for low-loss waveguides [64, 112]. Importantly, adjusting the process parameters in order to change the mechanical properties does not significantly affect the optical loss. Since SU-8 is deposited by common fabrication equipment, the processing conditions can be optimized in-house without the need for external vendors.

Another advantage of SU-8 is that it has a low Young's modulus. According to the equations in Section 2.2.2 and material properties in Table 2.2, SU-8 cantilevers can be made much thicker than Si_3N_4 cantilevers while preserving the same mechanical sensitivity. The increased thickness leads to increased misalignment tolerance between the cantilever and the output waveguide because the beam waist and coupling function are broadened (Equation 2.13). This in turn relaxes the requirement for low residual stress gradient.

3.3 Fabrication Process Flow

The fabrication process of the waveguide cantilever is described in Table 3.1, and that of the interferometric cantilever in Table 3.2. The description is qualitative and does not include process parameters. These values will be listed in Section 3.5 after a discussion of fabrication optimization in Section 3.4. The PDMS layer molding and the packaging procedures will be addressed in Section 3.7.










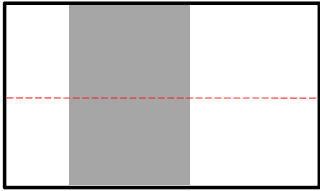

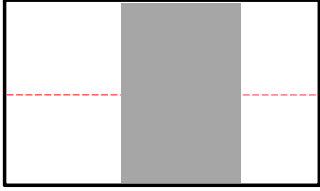




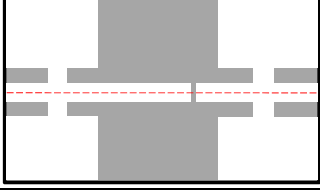

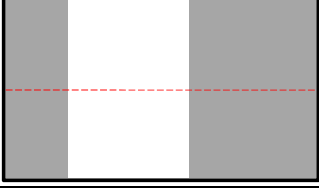

The two tables show the mask layouts at each lithography step and specify the corresponding photoresist polarity. Both masks used for the waveguide cantilever are chrome due to the requirement for small gap between input and output waveguides and optical-quality sidewalls. Although there are three mask patterns total in Table 3.1, steps 4 and 9 are performed with the same mask aligned differently. Therefore, only two masks were needed. For the fabrication of the interference cantilever, the same two chrome masks are used, and a low-cost low-resolution transparency mask is added to modify the SU-8 layout. The SU-8 is exposed consecutively with a chrome mask and a transparency mask; the equivalent mask pattern is shown in step 9 in Table 3.2.

In addition to the SU-8 layout, there are two other distinctions between the fabrication processes of the devices. First, the interferometric cantilever does not include a SiO₂ layer. Second, the alignment of the gold definition mask is biased differently as described next.

The alignment error of the contact lithography system used is on the order of 2 μm. If the gold mask is aligned to the edge of the cantilever, it is possible to “overshoot” due to alignment error and cover the cantilever facet with gold, causing excessive optical loss. For this reason, the alignment in the case of the waveguide device is biased to the left by approximately 5 μm as shown in Table 3.1, step 10. This leaves the facet of the cantilever free of gold even if there is alignment error to the right. In the case of the interferometric device, the cantilever tip should be covered by gold to facilitate interference fringe tracking. This device is not used as a waveguide, and covering its facet with gold is permissible. For this reason, the alignment is biased by several μm to the right as shown in Table 3.2, step 10.




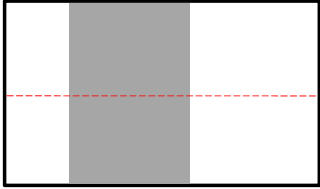
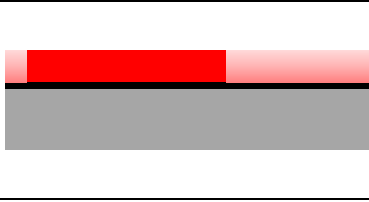
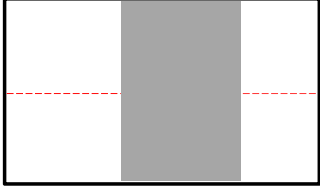
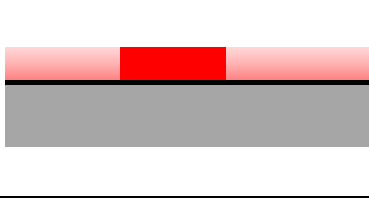



Note that the cantilever length in both fabrication processes is defined by the masks shift between steps 4 and 5. This allows the length to be varied between fabrication runs while using the same mask set. As discussed in Chapter 2, the cantilever length is one of the most significant design parameters since it impacts both mechanical and optical sensitivity.

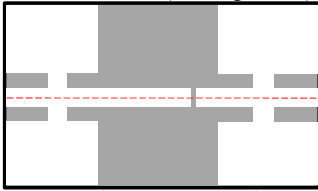
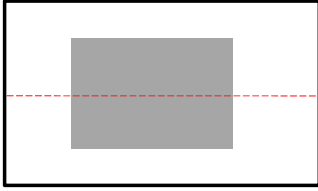
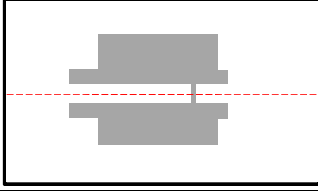

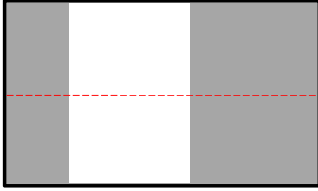




Table 3.1: Fabrication process flow of waveguide cantilever. The device cross sections are given along the dashed line in the mask layout.

Material legend:  Si  SiO ₂  Cr  SU-8  Au  Photoresist		
Step	Mask layout	Device cross section
1) Start with 4" Si wafer with 1 μm thick thermal oxide.		
2) Deposit Cr release layer (30 nm thick).		
3) Deposit Shipley 1813 photoresist.		
4) Expose with "release mask" (positive photoresist).		
5) Shift mask to the right and expose again. Overlap between exposures defines cantilever length.		
6) Develop photoresist.		
7) Etch Cr layer. Strip photoresist. Piranha clean (15sec).		
8) Deposit 2.2 μm thick SU-8 layer.		
9) Expose SU-8 (negative photoresist). During alignment, make sure the cantilever tip is over Cr release layer. Develop and hard bake.		
10) Deposit Shipley 1813 (positive photoresist). Pattern with "gold mask". Bias alignment to the left to make sure cantilever tip is covered. Etch exposed Cr.		

11) Deposit gold layer (15 nm thick).		
12) Perform lift off in acetone to pattern gold layer.		
13) Release cantilever by soaking in Cr etchant.		

Table 3.2: Fabrication process flow of interferometric cantilever. The device cross sections are given along the dashed line in the mask layout.

Material legend: Si SiO ₂ Cr SU-8 Au Photoresist		
Step	Mask outline	Device cross section
1) Start with 4" Si wafer.		
2) Deposit Cr release layer (30 nm thick).		
3) Deposit Shipley 1813 photoresist.		
4) Expose with "release mask" (positive photoresist).		
5) Shift mask to the right and expose again. Overlap between exposures defines cantilever length.		
6) Develop photoresist.		
7) Etch Cr layer. Strip photoresist. Piranha clean (15sec).		
8) Deposit 2.2 μm thick SU-8 layer.		

<p>9) Expose SU-8 (negative photoresist) consecutively with chrome and transparency masks. During alignment, make sure the cantilever tip is over Cr release layer. Develop and hard bake.</p>	<p>Chrome mask (1st exposure)</p>  <p>Transparency mask (2nd exp.)</p>  <p>Equivalent layout</p> 	
<p>10) Deposit Shipley 1813 (positive photoresist). Pattern with “gold mask”. Bias alignment to the right to make sure cantilever tip is not covered. Etch exposed Cr.</p>		
<p>11) Deposit gold layer (15 nm thick).</p>		
<p>12) Perform lift off in acetone to pattern gold layer.</p>		
<p>13) Release cantilever by soaking in Cr etchant.</p>		

After release, the Si wafer is cleaved into 6 individual chips, each containing 8 cantilevers. The cleaving was chosen over saw dicing since it produces smoother waveguide facets. The chips are kept wet during the cleaving and are stored in DI water afterwards until packaging. Allowing them to dry causes stiction to the

substrate. The preparation of the PDMS fluidic layer and the package assembly are described in Section 3.7.

3.4 Optimization of Fabrication Process

The process development was guided by two main considerations: resolution of the SU-8 pattern and reduction of the cantilever curvature. First, a test mask was used to explore the minimal achievable feature size in SU-8. These results were used for the choosing the gap between the cantilever and the output waveguide in the final mask design.

Figure 3.3 shows the SU-8 test pattern. It consists of 5 rectangles with varying gaps between them. The gaps defined on the mask range from 1 μm to 6 μm . It can be seen that the 1 μm and 2 μm gaps are not resolved in the fabricated pattern. The 4 μm and 6 μm gaps are resolved, but their sizes are reduced to 2 μm and 4 μm respectively. This narrowing is probably due to diffraction during lithography and lateral diffusion of the photoactivated SU-8 crosslinkers. Accordingly, the propagation gap between the cantilever and the output waveguide on the final mask was chosen to be either 4 μm (high-sensitivity design) or 6 μm (high-yield design). The actual dimensions used in the optical sensitivity calculations in Section 2.2.3 are 2 μm and 4 μm due to the narrowing effect.

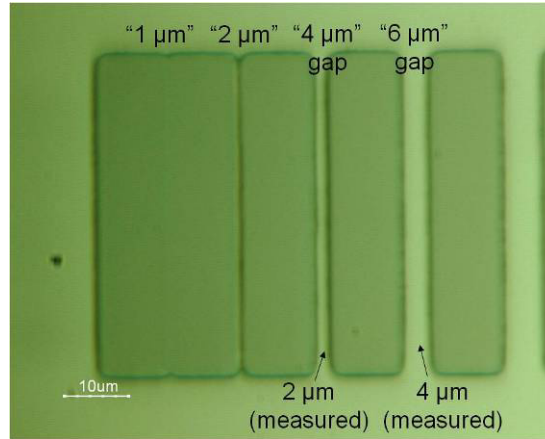


Figure 3.3: Microscope image of SU-8 pattern fabricated with test mask.

The results shown in Figure 3.3 are for an exposure dose of 200 mJ/cm^2 (measured at the 365nm wavelength). It was observed that increasing the dose further narrows the gap. For example, at a dose of 300 mJ/cm^2 , even the 4 μm gap was not resolved. Also, the sidewall roughness of the SU-8 was significantly increased, which would result in higher propagation losses due to scattering. For these reasons, the dose in subsequent fabrication runs was limited to 200 mJ/cm^2 .

Once the resolution constraints were understood, the process was optimized to reduce the cantilever curvature. Here, the curvature measurements could not be performed by breaking the beam and turning it on its side as in Figure 3.1. The SU-8 beams tend to deform plastically before breaking, leading to unreliable curvature readings. Instead, the cantilever tip height was determined by depth measuring microscopy or by counting the interference fringes in the image as described in Section 2.3.2 (the waveguide cantilever also has an interference pattern). The curvature and residual stress gradient were calculated from the tip height using Equation 2.4.

The residual stress in SU-8 is caused mainly by thermal coefficient of expansion (CTE) mismatch between the substrate and the film [132]. The CTE of SU-8 is approximately $2 \times 10^{-6} \text{ }^\circ\text{C}^{-1}$, and that of Si is on the order of $50 \times 10^{-6} \text{ }^\circ\text{C}^{-1}$. The SU-8 is crosslinked during the post-exposure bake at 95°C and is then cooled to room temperature. Since the SU-8 shrinks more than the substrate, it experiences tensile residual stress.

The residual stress gradient results from a cross-linking gradient [133]. Highly crosslinked regions of the SU-8 have a lower CTE and therefore lower residual stress than weakly crosslinked SU-8. The crosslinking gradient in the film is caused by a combination of exposure dose gradient and temperature gradient during processing. The exposure light intensity is higher near the top surface of the film, promoting higher crosslink density there. In contrast, the baking temperature tends to be higher at the bottom surface of the film contacting the substrate and accelerates the crosslinking there. As a result, the dose gradient and the temperature gradient create downward and upward cantilever bending, respectively. The former can be reduced by increasing the exposure dose sufficiently to saturate the concentration of photoinitiated crosslinkers throughout the thickness of the film; the latter can be minimized by baking in an oven instead of on a hotplate to create a more uniform temperature profile.

SU-8 beams with very small curvature on the order of $1 \times 10^{-2} \text{ mm}^{-1}$ [133] or even $4 \times 10^{-6} \text{ mm}^{-1}$ [131] have been achieved by minimizing the dose and temperature variations. However these demonstrations did not include a metal layer on top and were measured in air. In the present dissertation, the beam is coated with a gold layer

for binding of analytes and is immersed in liquid. As a result, the stress gradient is greatly increased due to several effects discussed next.

Initially, the SU-8 layer was patterned by RIE (reactive ion etching) instead of direct exposure in order to reuse the lithography mask designed for the Si_3N_4 fabrication. Since SU-8 is a negative photoresist, a mask of opposite polarity would be required for the direct exposure. A 200 nm thick gold layer was patterned on top of a blanket-exposed and cured SU-8 using positive photoresist, and it was used as an etch mask for RIE. The resulting cantilevers had excellent resolution, but they experienced large downward curvature. This curvature was not caused by the presence of the gold layer since the devices did not straighten after etching it off. The SiO_2 layer under the cantilevers was removed in an attempt to accommodate the curvature and prevent the cantilever tips from touching the substrate. However, the SiO_2 thickness ($1\mu\text{m}$) was not sufficient to achieve that. Figure 3.4 shows a cantilever fabricated in this manner with the gold purposely removed after RIE. The interference fringes indicate that the beam has a convex shape, i.e. it goes up and then down. This is due to the cantilever tip touching the substrate.

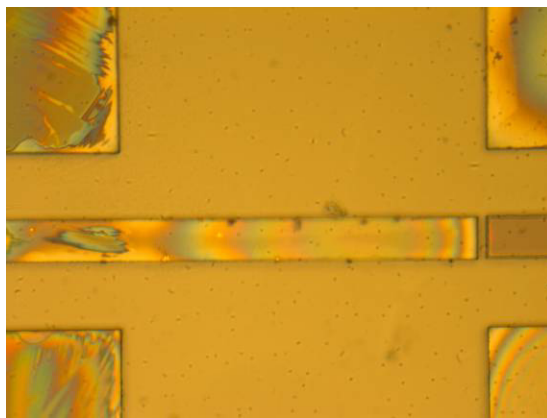


Figure 3.4: Microscope image of cantilever fabricated by RIE (imaged in water). The SiO_2 layer under the cantilever is removed by BOE (buffered oxide etchant). The surrounding structures are slightly undercut.

Multiple fabrication runs with varied SU-8 exposure and bake parameters gave similar results. The curvature direction was still downward, and the cantilever tips were touching the substrate. At this point, the fabrication process was modified to accommodate downward curvature rather than trying to reverse its direction. Increasing the SiO₂ layer thickness was not a viable option due to its high residual stress, which can cause wafer bow. Instead, the substrate under the cantilever was completely removed by DRIE (deep reactive ion etching) from the back side of the wafer. For this procedure, a photoresist pattern was defined on the back side and aligned with the front using an infrared microscope.

The DRIE approach resulted in severe deformation or breaking of the cantilevers. The removal of the substrate allows the beams to be bent down by almost a 90° due to fluidic and stiction forces during fabrication. Figure 3.5 illustrates the problem. In (a), the cantilever has severe downward curvature resulting from plastic deformation; its tip appears black in the image due to its large slope. In (b), the cantilever is completely broken off. The DRIE approach also has several other limitations in addition to the beam deformation. It cannot be used for the interferometric cantilever, which requires a reflective surface under the beam. Furthermore, it greatly increases the fabrication cost and complicates the packaging. Consequently, this approach was abandoned and the attempts to make cantilevers with reduced curvature were resumed.

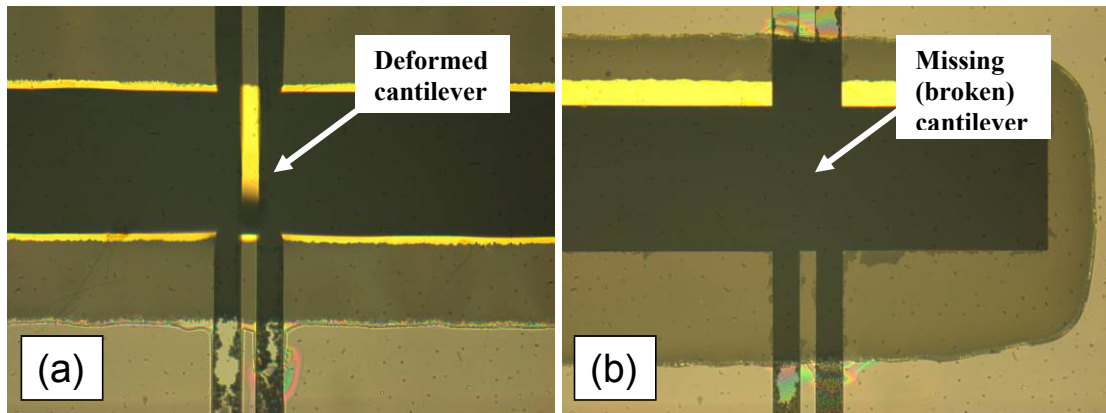


Figure 3.5: Microscope images of cantilevers released with DRIE from the back side (imaged in water). a) Cantilever severely deformed downward b) Cantilever broken off.

There is a possibility that the SU-8 etching process may heat up the film and contribute to the residual stress gradient. For this reason, a new lithographic mask with negative polarity was designed, and direct exposure was used to pattern the SU-8 instead of RIE. The gold layer was deposited after SU-8 development and hard bake. Cantilevers fabricated with this method still had a downward curvature (even after the gold was etched off). Figure 3.6a shows such a device; the interference fringes suggest that the tip of the cantilever is touching the substrate. Interestingly, devices fabricated by direct SU-8 exposure without gold deposition step were very straight as shown in Figure 3.6b. Here, there is only one visible interference fringe, suggesting that the beam bending is less than 250 nm (the fringe counting measurements were explained in Section 2.3.2).

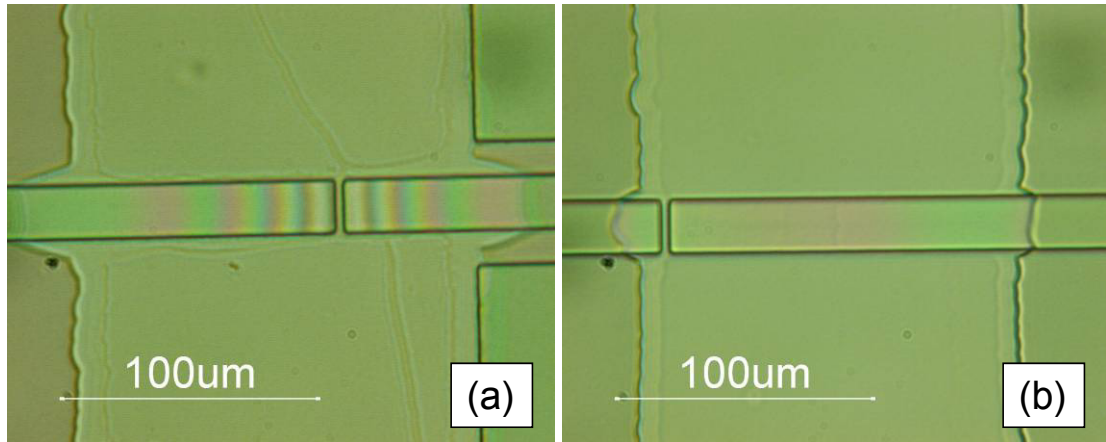


Figure 3.6: Microscope images of cantilevers fabricated by direct SU-8 exposure with the SiO₂ layer removed under the beam (imaged in water). a) Cantilever was originally coated with gold, which was removed after release. b) Cantilever was never coated with gold.

The differences between the two devices in Figure 3.6 are evidence that the gold deposition process somehow increases the residual stress gradient in the SU-8. This could be caused by X-rays or high temperatures in the e-beam evaporation chamber. The fabrication process was modified to place the gold layer on the bottom of the cantilever. The gold was deposited and patterned on the Cr release layer, and the SU-8 was deposited on top of the gold. Using this approach, the SU-8 is never exposed to the e-beam evaporation tool. Figure 3.7 shows a device with a 15 nm thick (transparent) gold layer on the bottom. The interference fringes indicate that it has downward curvature again and the tip is touching the substrate. When the gold layer was etched off, the cantilever straightened and became similar to that in Figure 3.6b. This suggests that the curvature is caused by the presence of the gold, and not by a stress gradient in the SU-8. Therefore, the direction of the curvature can be reversed if the gold is deposited on top by a method that does not affect the SU-8.

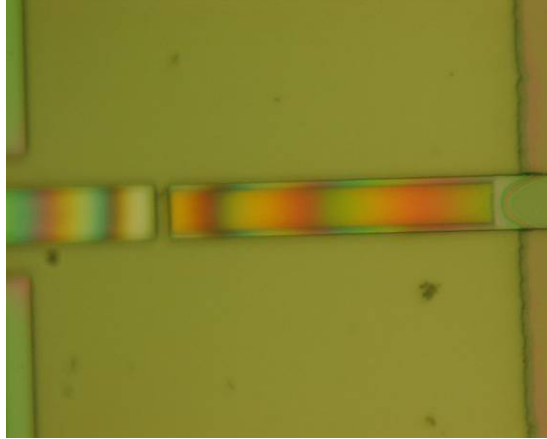


Figure 3.7: Microscope image of cantilever with gold layer on the bottom (imaged in water). The SiO₂ layer is removed under the beam.

The gold deposition up to this point was performed with e-beam evaporation due to the high quality of films produced by this method. Several experiments were carried out with thermal evaporation, which is typically considered an inferior method and results in less pure films. Interestingly, the gold-coated cantilevers produced with this approach had upward bending, as shown in Figure 3.8. This curvature is still too large (1.4 mm^{-1}), but it has the correct direction. Also, when the gold layer was etched off, the cantilever straightened and became similar to that in Figure 3.6b. This suggests that the thermal evaporation chamber does not significantly affect the SU-8 residual stress gradient, and that the curvature is caused by the presence of the metal film. For this reason, thermal evaporation was used for all subsequent fabrication runs.

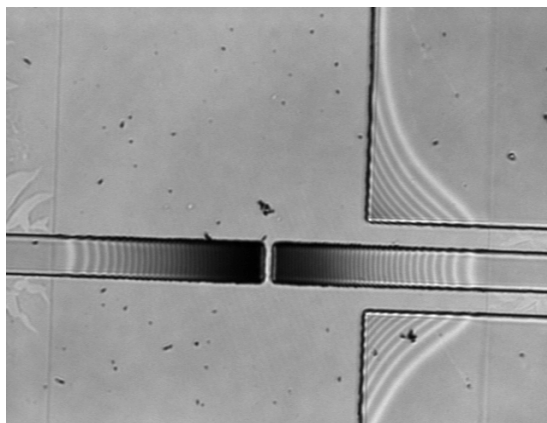


Figure 3.8: Monochromatic microscope image of 120 μm long cantilevers coated with 15 nm Au by thermal evaporation using a 15nm Cr adhesion layer (imaged in water). Both the input and output waveguides are released in this device. The cantilever tip height is estimated to be 10 μm by counting the number of interference fringes.

All gold films deposited on top of the SU-8 up to this point (both by thermal and e-beam evaporation) had a thin Cr adhesion layer. This is a standard practice since gold has poor adhesion to most materials and tends to delaminate. In attempting to reduce the residual stress of the metal layer, several experiments were performed without the use of Cr. This resulted in much lower curvature, as shown in Figure 3.9. The high stress caused by the Cr film is probably a consequence of its excellent adhesion to the surface. Although the gold film without Cr typically has poor adhesion, no delamination from the SU-8 was observed in this work even after prolonged use of the device. This may be due to the small thickness of the gold layer here (15 nm). Interestingly, the gold delaminates completely from the SiO_2 surface after the liftoff step. This is actually beneficial to the operation of the cantilever since it reduces the “parasitic” area that binds analytes without contributing to sensor response. Consequently, the final fabrication process does not include a Cr adhesion layer.

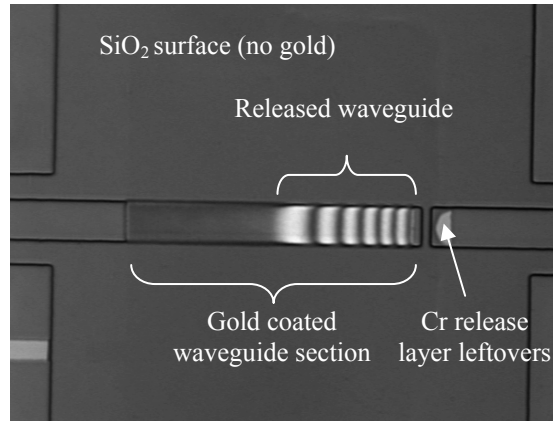


Figure 3.9: Monochromatic microscope image of 80 μm long cantilever coated with 15 nm Au by thermal evaporation without Cr adhesion layer (imaged in water). The tip height estimated by fringe counting is 1.5 μm .

The curvature of the device in Figure 3.9 is on the order of 0.4 mm^{-1} . This value is equivalent to a tip height of 2 μm for a 100 μm long beam, which is acceptable for both the waveguide and interferometric cantilever designs. If the gold is etched off, the curvature is further reduced and the beam becomes almost flat as in Figure 3.6b. Therefore, the presence of the gold still has some effect. This could be caused by two different mechanisms: residual stress of the gold and swelling of the SU-8 in water. The contribution of the former is likely minor since cantilevers that were dried were found to be very straight; the swelling effect is probably responsible for most of the curvature.

It has been observed that SU-8 swells in water [134]. In our device, the swelling is not uniform and creates a stress gradient. The top cantilever surface is blocked by metal and does not swell much, while the bottom surface is permeable to water and swells more. This results in a swelling gradient and beam bending. The swelling can be somewhat reduced by prolonged hard baking of the SU-8 but not completely eliminated. The minimal curvature achieved for Au-coated cantilevers in water was

approximately 0.23 mm^{-1} . Table 3.3 summarizes the different contributions to curvature that were discussed here.

Table 3.3: Contributions to curvature in metal coated SU-8 cantilevers.

Cause of curvature	Direction	Curvature (mm^{-1})	Method to reduce curvature
Cross-linking gradient	up	$ k < 0.1$	
- exposure dose gradient	down		Increase exposure dose
- temperature gradient	up		Bake in oven
E-beam evaporation	down	$ k > 2$	Use thermal evaporation or sputtering
Cr layer residual stress	up	$ k > 1.2$	Deposit Au without Cr layer
Swelling due to water	up	$0.23 < k < 0.37$	Increase hard bake time

The SU-8 swelling is greatly enhanced in solvents such as IPA, methanol, and acetone (it increases in that order). If the gold-coated cantilever is soaked for several minutes in one of these solvents, it becomes permanently deformed due to the large bending moment. This effect can be used for increasing the beam curvature if it is too small. As explained in Chapter 2, both the interferometric and waveguide cantilevers require some minimal curvature for proper operation. The solvents can also be used to release beams that have been stuck to the substrate (if the devices are allowed to dry, they experience stiction). When such a cantilever is exposed to the solvent, it bends up and breaks away from the substrate. However, the solvents should be used for short times since they can cause excessive deformation of the beam.

3.5 Final Fabrication Parameters

Many different fabrication conditions were tried during the process optimization described above. Table 3.4 lists the parameters that were found to satisfy both the resolution and beam curvature requirements. The fabrication results in Section 3.6 and testing results in the next two chapters are from devices fabricated using these final parameters.

Table 3.4: Summary of final fabrication parameters. The corresponding process steps from Table 3.1 and Table 3.2 are specified. All bakes are performed on a hotplate.

Release layer (steps 2, 7, 13)	
Deposition	Equipment: E-beam evaporation system (CHA Mark-40) Thickness: 30 nm
Etching	Chemical: Chrome etchant TFD (Transene Inc, USA) Nominal etch rate: 300 nm/min Etch time used: 1 min
Sacrificial release	Chemical: same as above Etch time used: 2 hrs on rocking platform
Lithography with Shipley 1813 photoresist (steps 3-6, 10)	
Vendor	MicroChem Corp, USA
Spinning	Cycle 1: 100 rpm for 1 s Cycle 2: 100 rpm for 1 s Cycle 3: 3000 rpm for 30 s (resulting thickness ~1.6 μm)
Soft bake	100°C for 60 s
Exposure	150 mJ/cm ² (measured at 405 nm wavelength)
Development	Developer: Microposit 352 Time: 30 s with manual agitation
Lithography with SU-8 (steps 8, 9)	
Vendor	MicroChem Corp, USA
Formulation used	SU-8 5 (5 μm nominal thickness)
Spinning	Cycle 1: 100 rpm for 2 s Cycle 2: 500 rpm for 5 s Ramp: 500 rpm to 5200 rpm in 10 s Cycle 3: 5200 rpm for 30 s (resulting thickness ~ 2.2 μm)
Soft bake	Ramp up: 50°C to 95°C at 300°C/hr Bake: 95°C for 16 min Cool: natural cooldown to 50°C before removing from hotplate
Exposure	200 mJ/cm ² (measured at 365 nm wavelength)
Post-exposure bake	Same as soft bake
Development	2 min in SU-8 developer (MicroChem) with manual agitation
Hard bake	Ramp up: 50°C to 190°C at 500°C/hr Bake: 190°C for 45 min Cool: natural cooldown to 50°C before removing from hotplate
Gold layer (steps 11, 12)	
Deposition	Equipment: Thermal evaporation system (Metra TEBC-22-26) Thickness: 15 nm (no adhesion layer)
Liftoff	2 min in acetone with manual agitation

3.6 Fabrication Results

As explained in Section 3.4, the main considerations in the process development were good resolution of the SU-8 pattern and low cantilever curvature. Here, we show that the fabricated devices meet both of these requirements. Figure 3.10 consists of top-down SEM images of an unreleased cantilever covered by 15 nm of Au. The propagation gap is clearly resolved; it is measured to be 3.5 μm , and it is quite uniform across the waveguide width (a). Furthermore, the edge roughness is relatively small and only visible at high magnification (b). These results are satisfactory, considering that they were obtained with contact lithography.

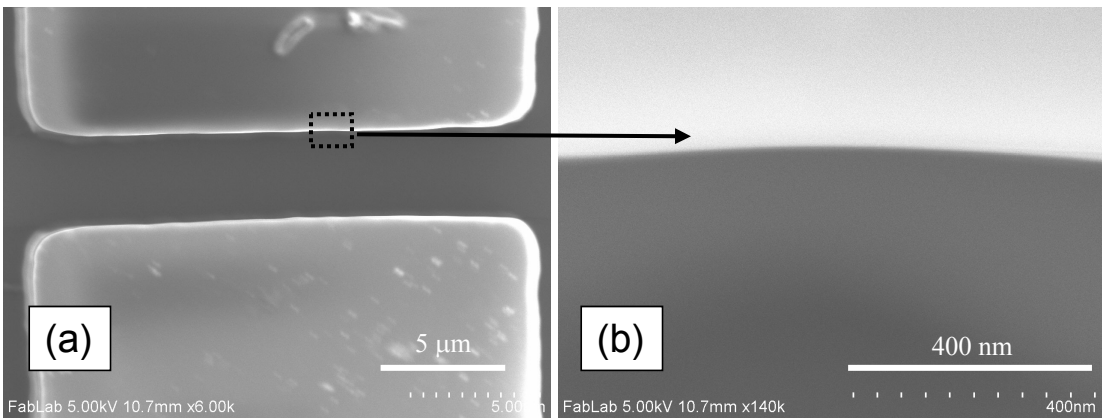


Figure 3.10: a) SEM (Scanning Electron Microscope) image of propagation gap between cantilever and output waveguide. b) SEM image zoomed in on cantilever tip.

Figure 3.11 shows two representative devices that are fully fabricated devices and ready for packaging⁵. Both cantilevers are approximately 110 μm long. Note that the waveguide cantilever in (a) has an area free of gold at the tip. As discussed previously (Section 3.3), this feature guarantees that there is no metal covering the waveguide

⁵ The brightness and contrast of the images in the figure are slightly different since they are obtained with different microscopes.

facet and blocking the light propagation. In contrast, the interferometric cantilever in (b) is completely covered with gold (including the tip) to facilitate tracking of the topmost fringe. The tip height of the device in (a) is estimated to be $1.7 \mu\text{m}$ by the fringe counting method. This value is appropriate for operation with high signal-to-noise ratio as discussed in Section 2.2.3. The corresponding beam curvature is 0.28 mm^{-1} . The estimated tip height of the device in (b) is $1.5 \mu\text{m}$, which translates to a curvature of 0.25 mm^{-1} and tip slope of 0.027. This slope value is within the desirable range for the interferometric cantilever discussed in Section 2.3.5.

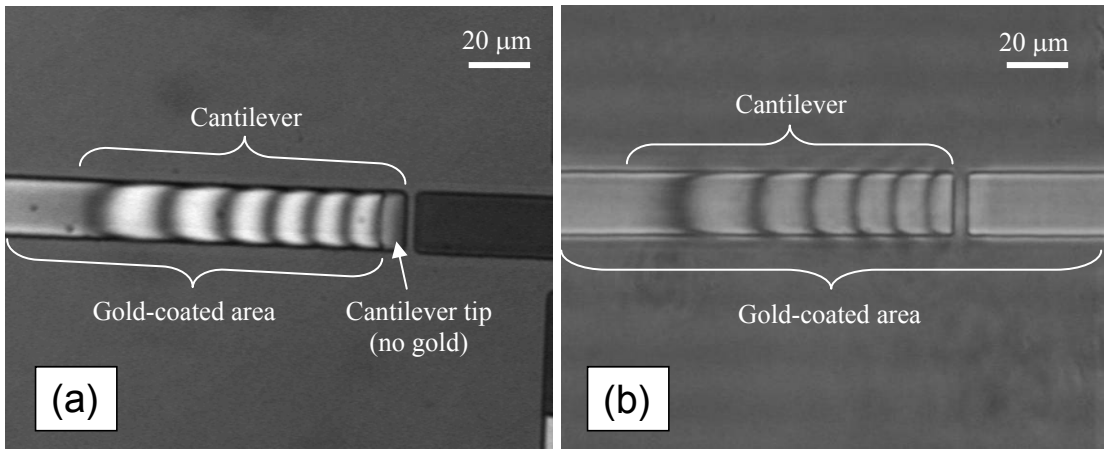


Figure 3.11: Monochromatic optical microscope images of fabricated devices (imaged in water). a) Waveguide cantilever b) Interferometric cantilever.

As expected, the curvature varies slightly between wafers and between cantilevers on the same wafer due to subtle differences in SU-8 thickness and processing conditions. This has negligible effect on the interferometric displacement measurements since each interferometric cantilever is referenced to its own initial position. However, it significantly affects the waveguide-based displacement measurements. In this case, the sensitivity varies from device to device due to the different tip heights, and the optical responses cannot be directly compared. This

issue will be addressed in Chapter 4 by using the theoretical model for optical transmission as a function of cantilever displacement.

3.7 Packaging

The microfluidic package enables the devices to measure liquid samples with very small sample volumes. As discussed in Chapter 1, the previous demonstration of waveguide cantilever sensors in literature were incapable of operating in liquids and did not include fluidic channels. The packaging process here consists of fabricating a molded PDMS layer and fixing it on top of the Si chip. As a result, the cantilevers are embedded inside sealed microfluidic channels. The PDMS fabrication procedures are the same for the waveguide-based and interferometric devices, but the channel layouts are different (these were shown in Figure 2.2 and Figure 2.15 respectively). Also, the two types of devices use different fixtures for securing the PDMS layer in place.

3.7.1 PDMS Layer Fabrication

First, a Si wafer is patterned with thick SU-8 to serve as a mold for forming channels in the PDMS. The lithography here is performed with a low-cost, low-resolution transparency mask since the fluidic channel dimensions are sufficiently large (Table 2.3). Two molds are prepared with the same SU-8 but different patterns: one of for the waveguide cantilever and one for the interferometric cantilever. The recipe for SU-8 fabrication is summarized in Table 3.5

Table 3.5: SU-8 process parameters for mold wafer fabrication.

Vendor	MicroChem Corp, USA
Formulation used	SU-8 50 (50 μm nominal thickness)
Spinning	Cycle 1: 240 rpm for 3 s Cycle 2: 500 rpm for 7 s Cycle 3: 1200 rpm for 20 s (resulting thickness $\sim 100 \mu\text{m}$)
Soft bake	Ramp up: RT (room temperature) to 95°C at 300°C/hr Bake: 95°C for 30 min Cool: natural cooldown to RT before removing from hotplate
Exposure	2250 mJ/cm^2 (measured at 405 nm wavelength)
Post-exposure bake	Same as soft bake
Development	25 min in SU-8 developer (MicroChem) with manual agitation
Hard bake	None

Next, a PDMS mixture is prepared with 10:1 ratio of resin to curing agent (Sylgard 184, Dow Corning, USA). The mixture is degassed in a vacuum dessicator until it contains no visible air bubbles. The SU-8 mold is placed in a 5 mm deep dish, which is then filled with the PDMS mixture. The dish is placed in a box furnace at 80°C for 1 hr to cure the mixture. Finally, the PDMS layer is peeled off the mold and cut to a size somewhat smaller than that of the cantilever chips. The depth of the resulting fluidic channels equals the thickness of the SU-8 on the mold. The thickness of the PDMS is roughly equal to the depth of the dish minus the combined thickness of the mold wafer and any spacer wafers placed under it. The target PDMS thickness was 4 mm and 2 mm for the waveguide-based and interferometric devices respectively (the latter benefits from lower thickness due to the need for microscope imaging).

3.7.2 Package Assembly

PDMS can be reversibly bonded to the SU-8 surface by wetting it, bringing it in contact, and allowing it to dry. This approach is commonly used in the fabrication of PDMS microfluidics [135]. However, as discussed previously, the drying of the cantilevers leads to stiction problems. For this reason, external fixtures were designed to hold the PDMS in place without drying the chip. The package is assembled while the cantilever is still wet, and the fluidic channel is filled with water to keep it wet after packaging. The fixtures for the two types of devices are different due to their specific testing requirements. In the case of the waveguide cantilever, the package must be compact enough to be placed on the XYZ optical stage, and it must allow access to the waveguide facets with external optical fibers. In the case of the interferometric cantilever, the packaging material on top must be transparent and thin enough to allow for high-resolution microscope imaging; also, individual connections must be made to the 8 parallel fluidic channels.

3.7.2.1 Waveguide Cantilever

The PDMS layer for the waveguide cantilever contains a single channel common to all 8 cantilevers on the Si chip. Since the optical testing setup allows for coupling light to only one device at a time, there is no need for a multiple parallel configuration. The channel is oriented perpendicular to the waveguides. The complete package is shown schematically in Figure 3.12, and the assembly procedure is described below.

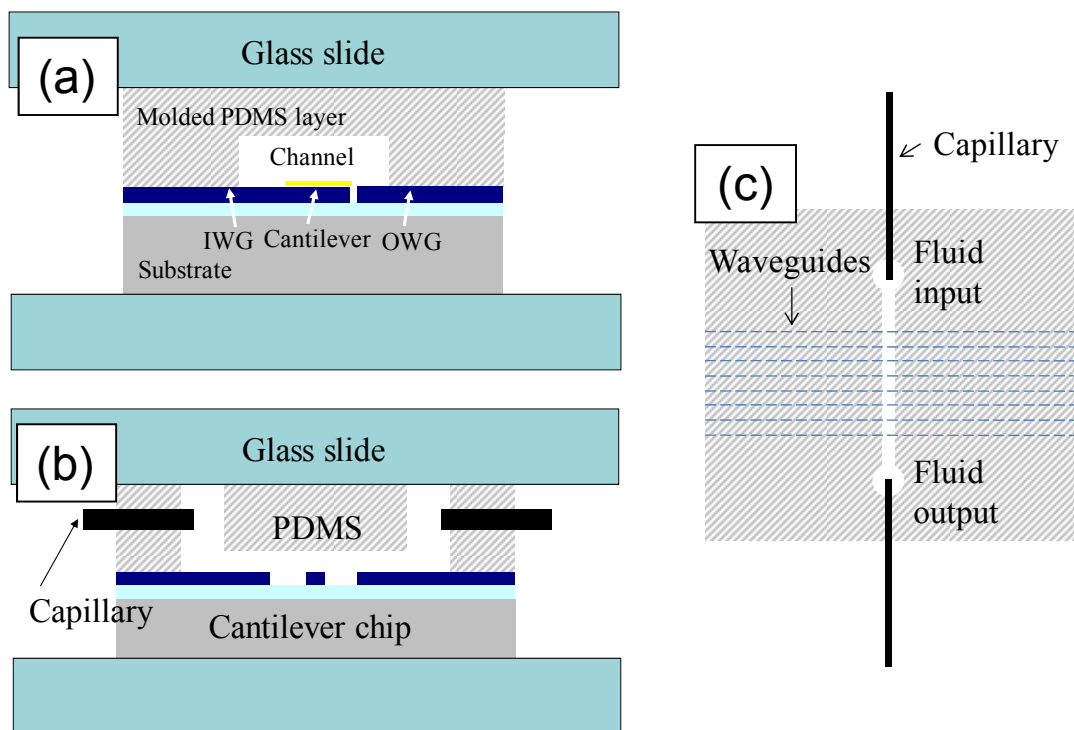


Figure 3.12: a) Cross section schematic of packaged cantilever chip along waveguide. b) Cross section schematic of packaged cantilever chip along fluidic channel. c) Top-down schematic of PDMS layer.

First, vertical holes are made in the PDMS at the ends of the channel with a 2 mm diameter hole punch. Then, steel capillaries (ID 200 μm , OD 400 μm) are inserted into the PDMS horizontally to meet these holes (Figure 3.12b). Next, the PDMS layer with the capillaries is aligned on top of the cantilever chip while still wet, observing the alignment under a microscope. The chip and the PDMS are placed between two vertically stacked glass slides, which are compressed with screw clamps. The resulting spacing between the glass slides is approximately 5 mm; this allows external optical fibers to be inserted near the waveguide facets on the edge of the cantilever chip. The capillaries are connected to Tygon flexible tubing (ID 380 μm , OD 2.3 mm), which is connected to a syringe pump for sample injection. Figure 3.13 shows a

photograph of a fully assembled fluidic package and a micrograph of a packaged cantilever.

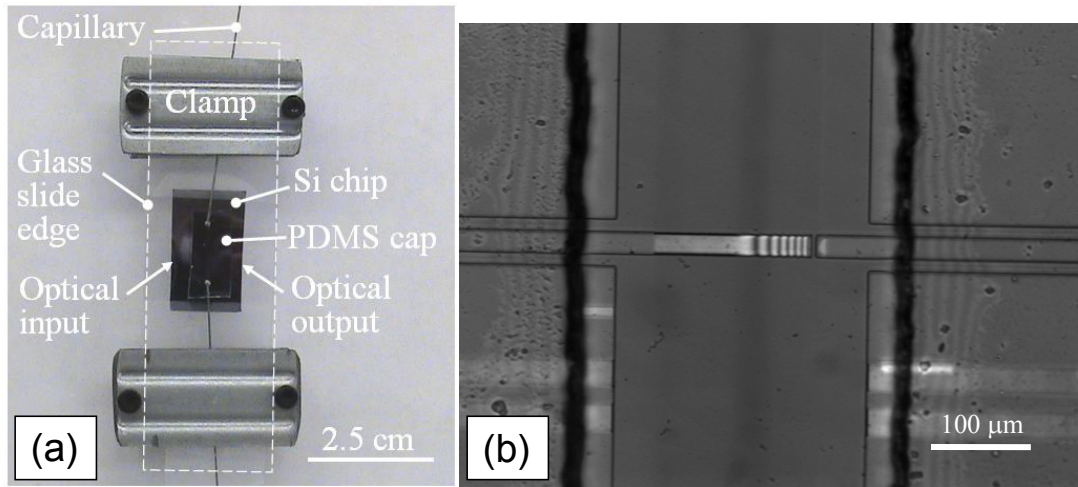


Figure 3.13: a) Photograph of fully packaged waveguide cantilever chip (top down view). b) Monochromatic microscope image of cantilever inside micro fluidic channel filled with water (top down view). The image was taken through the packaging materials.

3.7.2.2 *Interferometric Cantilever*

The interferometric readout can be used for monitoring the response of multiple devices to different samples concurrently. To take advantage of this, the PDMS layer here contains 8 channels (Figure 3.14a), one for each cantilever on the chip. The channels are oriented parallel to the cantilevers. Instead of fixing the PDMS layer in place with glass slides and mechanical clamps, magnetic force is used as illustrated in Figure 3.14b,c and further described below.

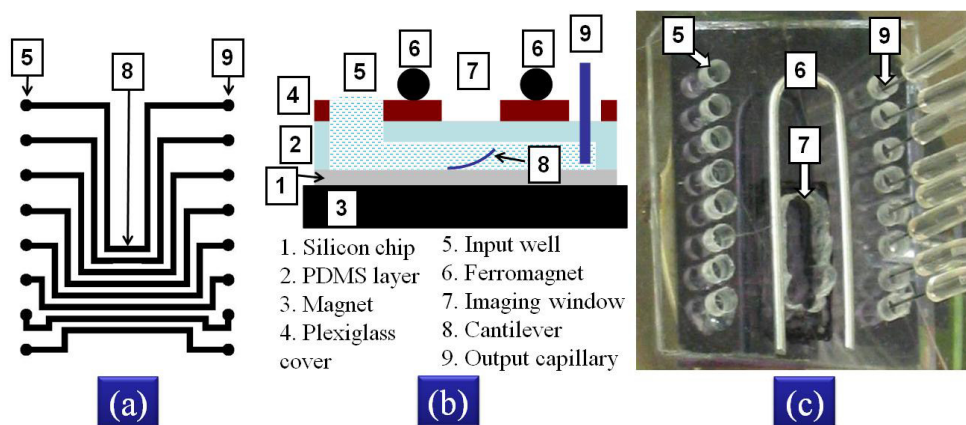


Figure 3.14: a) Layout of fluidic channels. b) Cross section schematic of packaged device along a channel. c) Top down photograph of fully packaged chip (width is 2.5 cm).

The silicon chip is set on top of a flat permanent magnet. The PDMS slab is aligned on the chip while observing it with an optical microscope. The PDMS is then fixed in place with a piece of ferromagnetic material on top (Figure 3.14b). A rigid plexiglass cover (3 mm thick) is inserted between the PDMS and the ferromagnet in order to distribute the compression force over the soft PDMS. The bottom PDMS surface makes conformal contact with the chip, creating 8 leak-tight fluidic channels. Throughout the packaging procedure, the surface of the chip is kept wet. This prevents stiction of the cantilevers to the substrate and also facilitates the alignment.

All channels are 100 μm deep and 500 μm wide. The channel pitch at the center of the chip is 1 mm, which is equal to the cantilever pitch. The channel pitch on both the input and output sides increases to 3 mm. The input of each channel consists of a 2 mm diameter well that serves as a sample container (Figure 3.14b,c). The volume of the well is $\sim 15\mu\text{L}$. The output of each channel consists of a steel capillary (ID 200 μm , OD 400 μm) connected to Tygon flexible tubing (ID 380 μm , OD 2.3 mm). The sample is sucked from the input well into the channel by applying vacuum on the Tygon tubing with a syringe. The plexiglass cover has holes allowing access to the

inputs and outputs and a window for observation of the cantilevers with the microscope. The window is necessary because the plexiglass blurs the image at high magnification. Figure 3.15 shows micrographs of fully packaged cantilevers taken through the window. In (a), several of the parallel fluidic channels are visible.

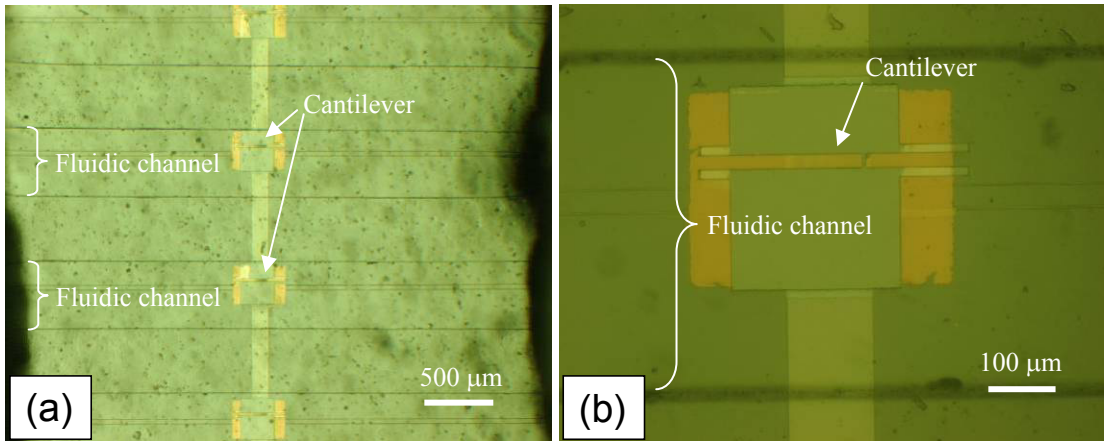


Figure 3.15: Microscope images of cantilevers inside fluidic channels taken at a) low and b) high magnification.

Before package assembly, holes with diameter 2 mm are punched through the PDMS to form the input wells. Smaller holes with diameter 300 μm are made on the output sides of the channels for the steel capillaries. The capillaries are inserted in the holes after the PDMS is aligned to the chip and secured in place with the plexiglass and ferromagnet.

The package for interferometric cantilever is easier to align and assemble than the one for the waveguide-based device described previously. The use of the magnet results in a more distributed compression force than the clamping approach, and it allows the I/O connections to be made directly on the top instead of the sides. Furthermore, the use of input wells and suction reduces the number of required connections to one per channel and facilitates the sample injection. However, this packaging approach could not be used for the waveguide cantilever because the

magnet spontaneously snaps to the steel components in the optical table setup. If optomechanics made of non-ferromagnetic materials are available, this problem can be resolved.

3.8 Summary

This chapter described the fabrication of both the waveguide and interferometric cantilevers. The differences and similarities between the two types of devices were highlighted throughout the text. In addition to presenting the detailed process flow and the final recipes, the choice of materials and the optimization of fabrication parameters were discussed. The main goals during process development were to resolve the gap between cantilever and output waveguide and to maintain a small upward cantilever curvature. These goals were successfully met after a number of improvements. Finally, the packaging procedures for the two devices were presented in detail.

Chapter 4: Waveguide Cantilever Testing

4.1 Introduction

This chapter presents the characterization of the waveguide cantilever sensor and its use for detection of homocysteine. First, the experimental setup is described, and the testing procedures are explained. Next, several optical characteristics of the device are measured, including the propagation loss of the waveguides, the power change due to optical stage drift, and the power change as a function of cantilever displacement. Then, two different types of homocysteine detection experiments are performed. The first type uses a sample obtained from dissolving commercially available homocysteine powder. For the second type of experiments, the homocysteine sample is synthesized by the bacterial quorum sensing enzymes immobilized in the microfluidics. In some of the tests, interferometric measurements are used to measure the cantilever displacement independently and verify the theoretical coupling function. Finally, the detection results from the different experiments are compared and discussed.

4.2 Experimental Setup

The packaged device is mounted on a fixed stage under an optical microscope (Leica MZ 12.5) with a digital camera. A lensed 9 μm core fiber (Corning OptiFocus) is used to couple light from a 635 nm pigtailed laser diode (Newport LD-635-21B) to the input waveguide. Light from the output waveguide is collected by a 62.5 μm core fiber and guided to a computer-controlled optical power meter (Newport 818-SL).

The signal from the power meter is acquired and logged by a PC at a sampling rate of 1Hz. Both the input and output fibers are mounted on XYZ precision positioning stages (Newport Ultralign 561D). The fluidic input is connected to a syringe pump via Tygon flexible tubing, and the fluidic output is routed to a waste beaker. Figure 4.2 and Figure 4.2 illustrate the setup with a block diagram and photographs.

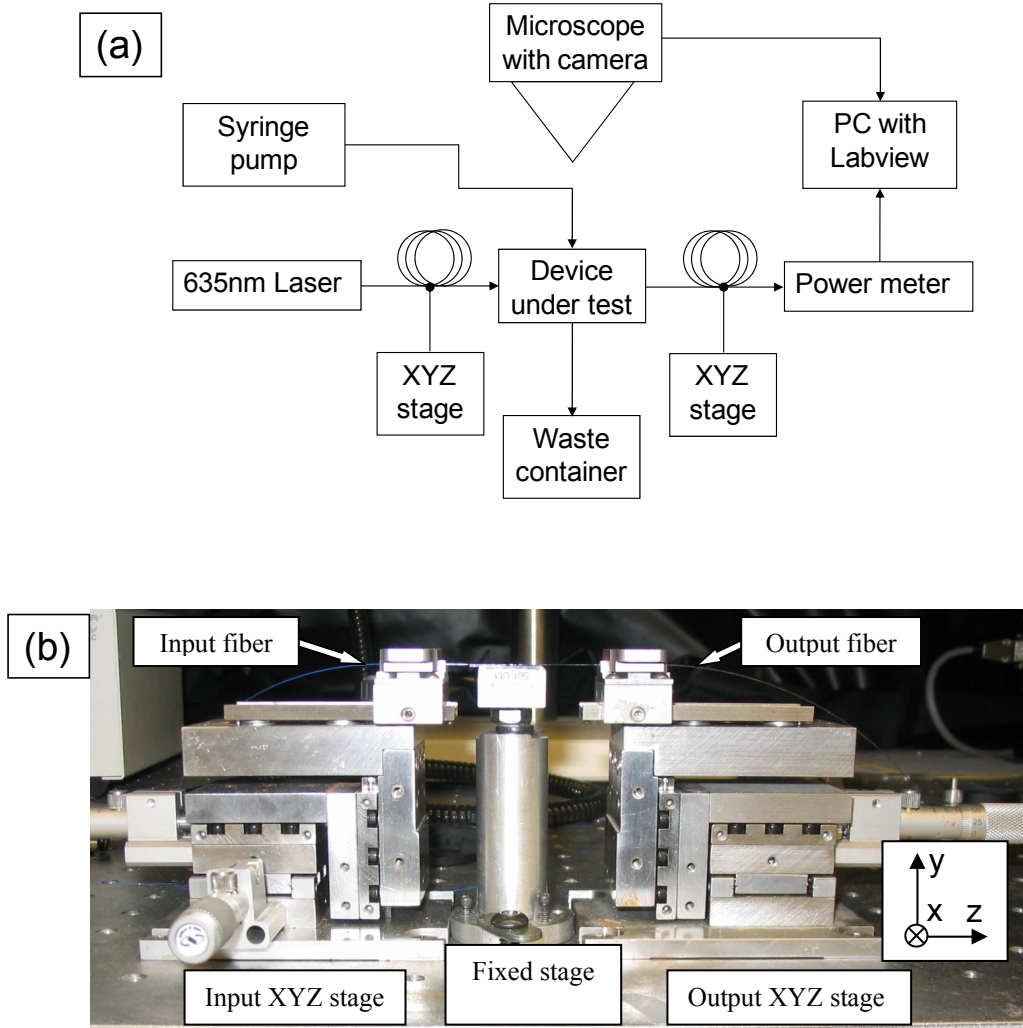


Figure 4.1: a) Block diagram of testing setup. b) Side view photograph of XYZ stages (without a device under test).

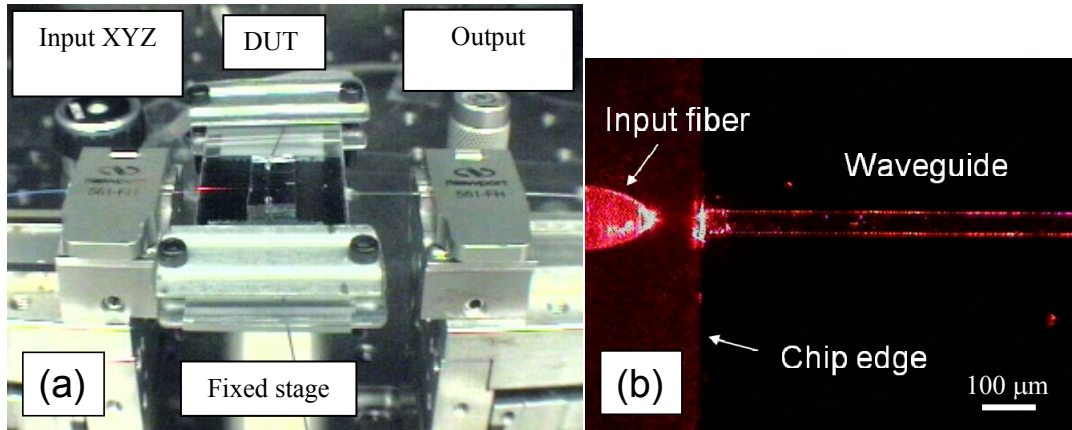


Figure 4.2: a) Perspective view photograph of XYZ stages with device under test (DUT). b) Microscope image of laser light coupled from input fiber into on-chip waveguide.

4.3 Optical Characterization

4.3.1 Loss Measurements

The optical power arriving at the output of the device is essential to its operation. The received signal must be much larger than the photodetector noise, which is on the order of 1 pW. If this condition is fulfilled, the signal to noise ratio is limited only by the drift of the XYZ stages discussed in Section 4.3.2 and not by the photodetector. The maximum input laser power available is approximately 300 μW (measured at the end of the lensed fiber). The main losses along the device are labeled in Figure 4.3. The insertion loss is caused by the modal mismatch between the optical fibers and the on-chip waveguides (1). There is also slight modal mismatch between the waveguide and the cantilever (3), but that should be negligible compared to the insertion loss.

The propagation loss results from scattering by waveguide defects and material absorbance (2). The gold-coated section of the waveguide has an additional loss component due to the metal absorbance (4). The cantilever coupling loss is caused by the divergence of the cantilever mode in the unguided medium and by the variable vertical offset of the cantilever from the output waveguide (5).

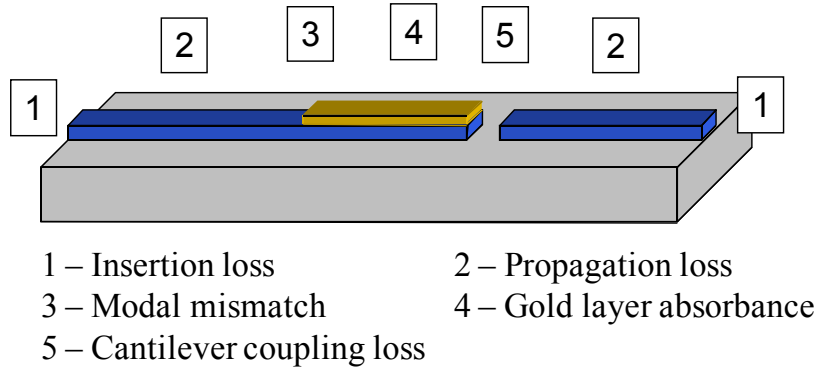


Figure 4.3: Optical loss mechanisms in waveguide cantilever sensor.

The total loss for a cantilever with 0 offset (stuck to the substrate) was measured to be approximately 25 dB. This value was obtained by dividing the output power (300 nW) by the input power (90 μ W). Finding the contributions of each mechanism shown in Figure 4.3 is difficult and not necessary in this case. For example, one could compare the total loss of devices with and without gold in an attempt to isolate loss component 4. However, the insertion loss varies considerably between devices and even between measurements of the same device. This variability prevents the extraction of individual loss components from the total loss values.

Only the propagation loss (2) was measured independently from the other losses. For this, the scattered light intensity method was used [136]. The scattered light intensity along the waveguide was acquired from a digital image and plotted on a logarithmic scale as shown in Figure 4.4. The image is similar to that in Figure 4.2d but taken at lower magnification over a larger area. It is assumed that the local intensity of the scattered light is proportional to the local power carried by the waveguide; therefore, the decay in intensity represents the propagation loss. The slope of the fitted line in the figure is 0.14 dB/pixel. Using the scaling factor of 50 pixels/cm, this corresponds to a propagation loss of 7 dB/cm. The theoretical loss

found in Chapter 2 was only 0.0013 dB/cm, taking into account the substrate absorbance but ignoring waveguide imperfections. This discrepancy suggests that the bulk of the loss is caused by scattering defects such as sidewall roughness.

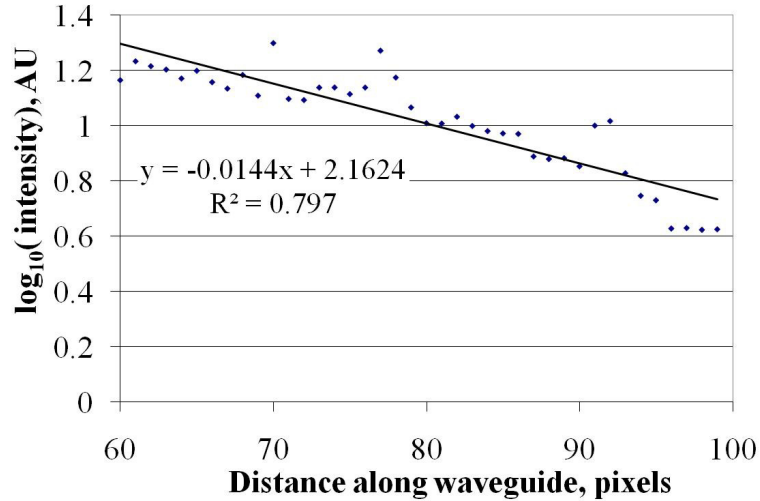


Figure 4.4: Scattered light intensity along a waveguide measured from a camera image of the waveguide.

SU-8 waveguides with much lower propagation losses have been previously reported, such as 2.5 dB/cm [112] or even 1.75 dB/cm [64]. The reason for the higher loss in the present work is the smaller waveguide thickness (2.2 μm compared to 10 μm and 130 μm respectively). Since the energy in a thin waveguide is on average closer to the surface, the roughness has a more detrimental effect than in thick structures. The propagation loss can potentially be reduced by improving the sidewall quality of the SU-8. This can be accomplished, for example, by using projection instead of contact lithography. In spite of the high loss, the output power was found sufficient for the purposes of this work and further fabrication improvements were not pursued.

As explained previously, the total loss for a device with 0 vertical cantilever offset is approximately 25 dB. Roughly 11 dB of that is due to propagation loss (using a cumulative waveguide length of 1.5 cm), and the rest is dominated by insertion loss. Offsetting the cantilever from the output waveguide considerably increases the loss, but it improves the signal-to-noise ratio as discussed in Section 2.2.3.7. This offset is set by cantilever curvature and length. The devices that were fabricated and tested had a wide range of offsets and resulting output powers; however, in all cases the output power was at least 10 pW to ensure that it is well above the noise floor of the photodetector. The loss for increasing cantilever offsets is measured in Section 4.3.3 and compared to theoretical values.

4.3.2 Power Drift

As discussed in Section 2.2.3.7, the main source of noise in the output signal is due to the mechanical drift of the XYZ positioning stages. The input and output fibers move relative to the chip slightly (on the order of nm), causing a gradual power change over time. Since this power change can be misinterpreted as cantilever response, it limits the minimal detectable cantilever displacement. The drift was measured over a period of 1000 s for several different conditions described below. This length of time was chosen since it is expected to be sufficient for a homocysteine detection event. To isolate the stage drift effect from possible cantilever motion, a device with unreleased cantilevers was used for these experiments.

In the initial tests, the set screws on the XYZ stages were not tightened (for convenience), and the optical fibers were brought very close the waveguide facets in order to achieve maximal power coupling. Figure 4.5 shows that the measured power

drift over 1000s in this case is almost 70%, which is unacceptably high. The drift is not always upward; it changes direction, depending on the initial position of the XYZ stage. However, it was found that the percentage power change in several different experiments was on the order of the value shown here.

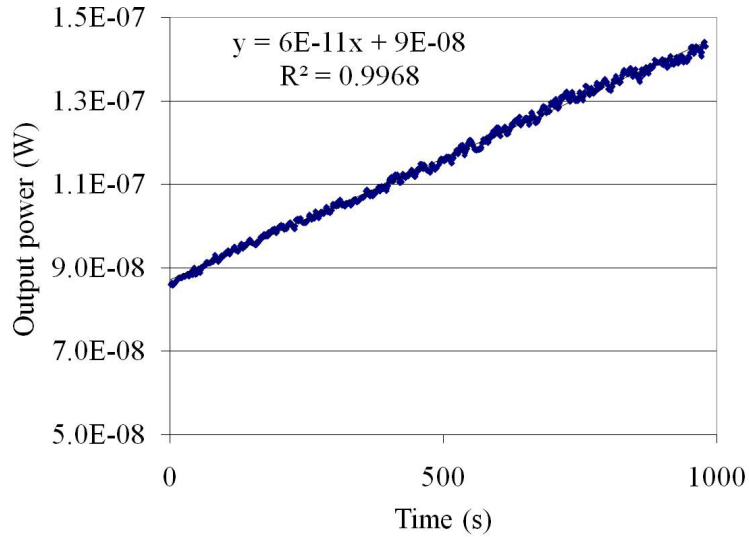


Figure 4.5: Optical power drift of XYZ stages with set screws left untightened and fibers positioned at a minimal distance ($\sim 5 \mu\text{m}$) from the waveguide facets. Regression trendline and equation included.

Tightening the set screws on the XYZ stages reduced the drift to approximately 20%. A further, more significant improvement was gained by increasing the distance between the input optical fiber and the waveguide facet in the z-direction. The coupling coefficient between the fiber and on-chip waveguide has a similar functional form as the cantilever coupling coefficient (Equation 2.7 and Equation 2.13). The output power is most sensitive to stage drift in the y-direction (vertical). This sensitivity can be reduced by broadening the input beam waist and thereby broadening the coupling function. When the fiber-to-waveguide distance is increased, the input beam is broadened due to divergence and the optical drift is reduced

(although the mechanical drift remains the same). Figure 4.6 shows that the resulting drift is less than 3%.

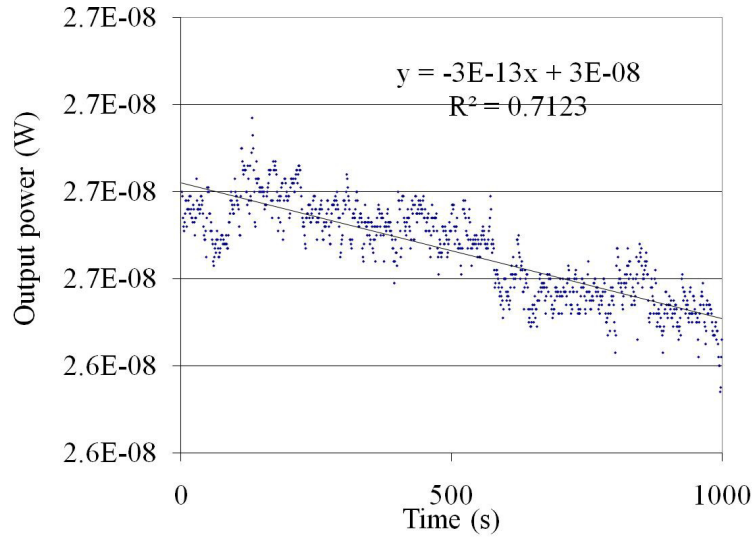


Figure 4.6: Optical power drift of XYZ stages with set screws tightened and input fiber positioned far ($\sim 30 \mu\text{m}$) from the waveguide facet. Regression trendline and equation included.

This approach was not used for the output fiber because it has a much larger core diameter ($62.5 \mu\text{m}$) and is less susceptible to the drift effect. The penalty for increasing the fiber-to-waveguide distance at the input is the reduced optical power coupled to the device and ultimately to the detector. However, this tradeoff is acceptable considering that the detector can measure very low power (Section 4.3.1).

In the control experiments, the input fiber was directly routed to the detector without passing through a device under test. The measured power drifted by only 0.3% over 1000s. This verifies that the laser and the detector are quite stable, and the observed power variations in the previous experiments are indeed due to stage drift.

4.3.3 Optical Power vs. Tip Deflection

The next step in the optical characterization of the waveguide cantilever was to measure the change in output power as a function of displacement and to compare it

to the theoretical model. This was performed by drying an unpackaged cantilever and moving its tip vertically with a microprobe needle while recording the optical output power. The resulting cantilever offset was estimated by counting the number of interference fringes in the microscope image as described in Section 2.3.2. Figure 4.7 shows the measured power at each offset for a 140 μm long device with cantilever-to-waveguide-gap of 4 μm . The theoretical power based on the coupling function in Equation 2.13 is plotted for comparison (the coupling function is scaled, making its peak equal to the maximum measured output power).

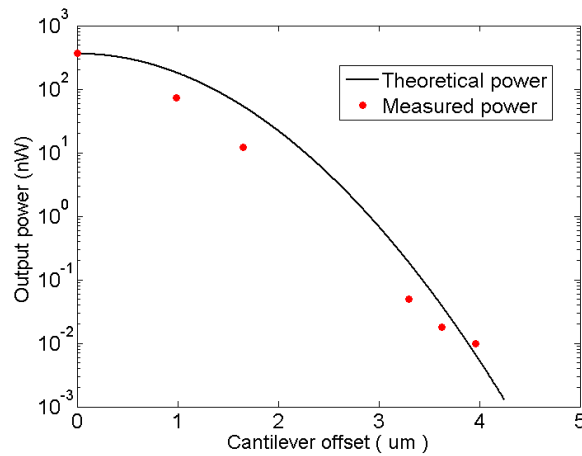


Figure 4.7: Measured and theoretical output power as a function of cantilever vertical offset from output waveguide. The cantilever is 140 μm long and it is measured in air after drying.

Overall, the measured data points agree reasonably well with the theoretical curve in the figure. The discrepancies are most likely due to cantilever torsion. The microprobe needle used to move the cantilever vertically also twists it slightly; this makes the measured output power lower than the theoretical value. It should be noted that these results are coarse and are aimed at showing the output power variations for large cantilever displacements. In the experiments described next, the cantilever is moved more precisely over short ranges by means of chemical samples.

4.4 Detection of Homocysteine from Powder

As explained previously, homocysteine is a byproduct of the bacterial signaling pathway of AI-2, and the capability to detect it in a microfluidic device will be useful for antibacterial drug discovery. The waveguide cantilever sensor developed in this dissertation is aimed at detection of homocysteine produced by the bacterial enzymes. For the initial testing, however, homocysteine from commercially available powder was used to verify the sensor response rather than enzymatic homocysteine. This eliminated the need for immobilizing the enzymes and significantly simplified the experimental procedures.

4.4.1 Procedures

Unless otherwise mentioned, a fully packaged microfluidic device (Section 3.7.2.1) was used for each detection experiment presented below. Liquids were injected in the device by the external syringe pump at rates ranging from 2 $\mu\text{L}/\text{min}$ to 10 $\mu\text{L}/\text{min}$. Before each experiment, the device was cleaned by flowing dilute HCl (1% w/w) for 5 min, followed by a DI water rinse for 5 min. Homocysteine samples were introduced in the device after flowing pure DI water to establish a baseline signal. The samples were prepared by dissolving homocysteine powder (Sigma Aldrich, USA) in DI water to the specified concentrations. Since the homocysteine solution is unstable, a fresh sample was prepared for each experiment. The optical fibers were initially aligned to the input and output waveguides by adjusting the XYZ stages and were left in the same position for the entire duration of the measurement. The output of the optical power meter was continuously logged by a computer.

The tested cantilevers had varying dimensions and curvatures. For this reason, the following parameters are listed for each presented experiment: cantilever length, propagation gap between cantilever and output waveguide, and initial tip height of cantilever (estimated by the fringe counting method).

4.4.2 Detection Results

The first experiment was performed with a device that was packaged differently than described in Section 3.7.2.1. Instead of using the molded microfluidic layer, a simplified PDMS layer was fabricated to form a well over the cantilever. The well had lateral dimensions of approximately 1 cm by 1 cm, and depth equal to the PDMS thickness (~5 mm). The well was created by cutting out a piece of the PDMS. In this experiment, there were no fluidic connections; instead, the liquids were introduced into and removed from the well with a pipette. The sample concentration was 10 mM.

Figure 4.8 shows the measured response of the waveguide cantilever. The coupled power increases by a factor of 12 over a period of 2000 s after sample introduction due to gradual binding of homocysteine to the gold surface via its thiol group. The shape of the coupling function (Figure 2.13) suggests that the increase in output power in Figure 4.8 was caused by downward cantilever displacement. This was confirmed by counting the number of interference fringes in the microscope image of the cantilever before and after sample introduction. Downward displacement means that the homocysteine creates compressive stress on the gold surface. This conclusion is consistent with reports of the stress generated by other thiol compounds [86, 137].

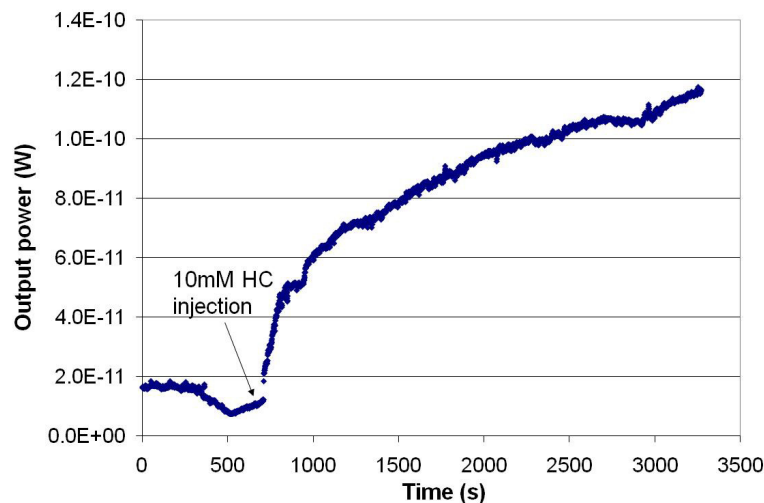


Figure 4.8: Response of a waveguide cantilever to 10 mM homocysteine sample. The cantilever length, initial tip height, and propagation gap are 140 μm , 2.2 μm , and 4 μm respectively.

Although this result clearly shows detection of homocysteine, the PDMS-well packaging approach was found to be unsatisfactory. The sample concentration could not be accurately controlled; when injecting a new liquid in the well, the old liquid could not be completely removed with the pipette. Also, the variations in liquid level in the well somewhat influence the optical output power (as evidenced by the drop in power in Figure 4.8 just before sample injection). For these reasons, the microfluidic packaging approach described in Section 3.7.2.1 was developed and used for all subsequent experiments. It resulted in more stable and repeatable sensor response.

Figure 4.9 shows the response of a cantilever using the improved packaging method. Note that in this case the optical power remains stable before the sample injection point. The 5 mM homocysteine solution causes the power to increase by a factor of 9. The sample is followed by DI water, which does not appreciably change the output power. Ideally, no change in power is expected here since the thiol group of homocysteine should be covalently bound to the gold surface and should not be removed by water rinsing. The small decrease in power may be the result of some

physically adsorbed homocysteine molecules being removed. Importantly, the DI water flowing before and after the homocysteine sample introduction has exactly the same optical properties. This verifies that the large change in output power is caused by cantilever bending and not by a change in the optical properties of the medium.

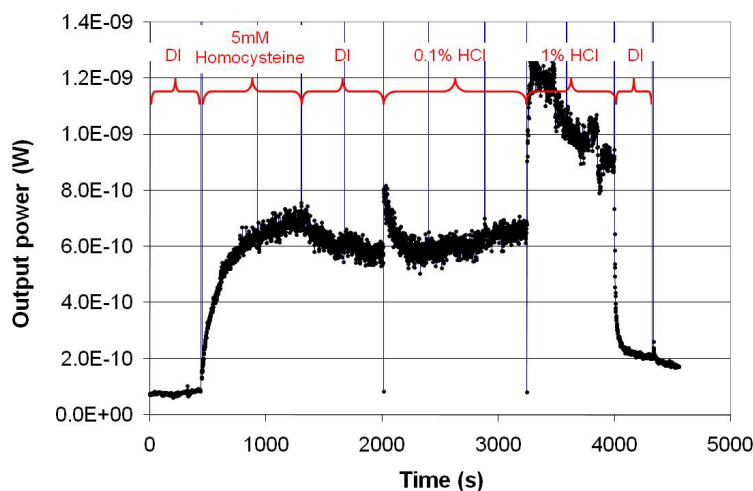


Figure 4.9: Response of a waveguide cantilever to 5mM homocysteine sample followed by DI water and hydrochloric acid. The cantilever length, initial tip height, and propagation gap are 110 μm , 2.2 μm , and 2 μm respectively.

The DI water is followed by dilute hydrochloric acid (0.1% and then 1% w/w) in an attempt to clean the cantilever. It has been shown that thiol compounds can be removed with acidic solutions [138]. The HCl causes the cantilever to bend further down (power goes up) while it is present; when it is rinsed with DI, the cantilever returns close to its initial position, indicating that the majority of homocysteine molecules have been removed from the gold.

The cleaning with HCl was investigated further. Figure 4.10 shows the results from repeated cleaning and reuse attempts. After each clean step, the cantilever returns close to its initial position. However, the response to subsequent homocysteine samples decreases. This may be due to increasing contamination of the gold surface, leaving less area available for homocysteine binding. The dilute

hydrochloric acid wash is not enough to remove the contaminants. The preferred methods for cleaning gold surfaces for assembly of thiol compounds (oxygen plasma or piranha solution) are not compatible with the sealed fluidic device. The oxygen plasma requires top-down access to the surface being cleaned, and piranha etches polymers, including SU-8 and PDMS. Therefore, no method was found to clean the device thoroughly and reuse it multiple times. Nevertheless, it should be noted that the cantilever is compatible with MEMS batch microfabrication and is extremely low-cost. For this reason, even a single-use, disposable sensor would be acceptable.

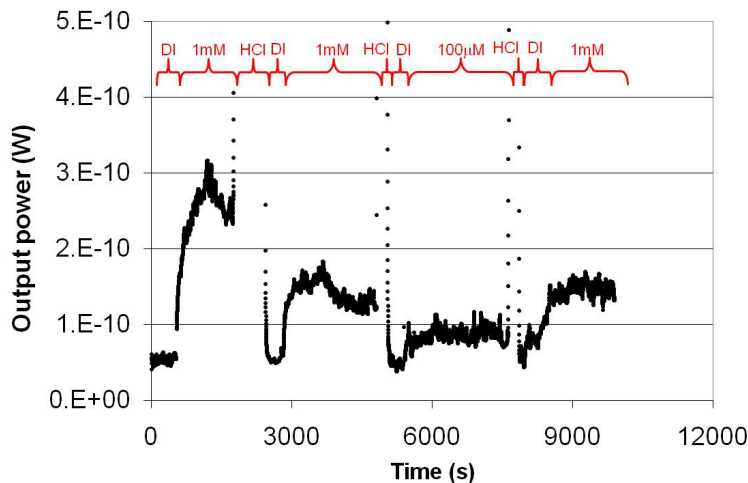


Figure 4.10: Response of a waveguide cantilever to homocysteine samples followed by cleaning with 1% w/w hydrochloric acid. The cantilever length, initial tip height, and propagation gap are 110 μm , 2.2 μm , and 4 μm respectively.

Figure 4.11 shows the response of an optical cantilever to increasing concentrations of homocysteine. Solutions with concentration from 1 μM to 10 mM were introduced sequentially. The lowest concentration does not produce a measurable change in optical power, but the second lowest (10 μM) causes a clear response. The optical power changes further by introducing 100 μM and 1 mM

solutions, although the relative changes become smaller. Finally, the transition to 10 mM does not produce any measurable response.

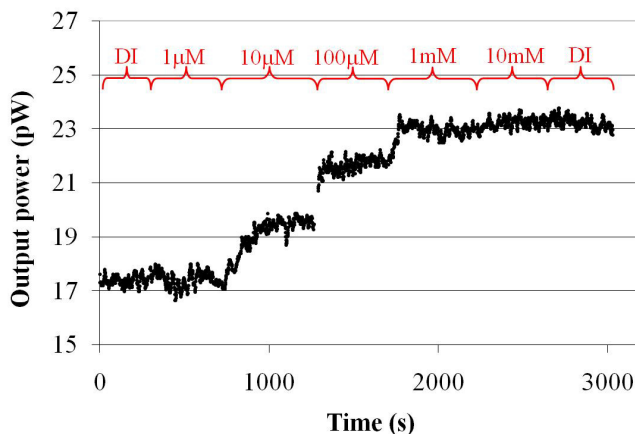


Figure 4.11: Response of a waveguide cantilever to increasing concentrations of homocysteine. The cantilever length, initial tip height, and propagation gap are 70 μm , 0.75 μm , and 2 μm respectively.

These results are consistent with the first order kinetics model of thiol assembly to gold surfaces [139]. According to the model, the final surface density of thiols is independent of the solution concentration, and the binding rate is proportional to the solution concentration and the vacant surface area. In the 1 μM region in Figure 4.11, the solution concentration is the limiting factor to binding rate. In the 10 mM region, the surface is already covered with thiols by the previous samples, and the vacant surface area becomes the limiting factor. This explains why the binding rate in both of these regions is low and the change of optical power is unmeasurable. However, the first order thiol assembly model is a crude approximation. After the initial binding, the thiol layers undergo several phase transitions that are not completely understood [140]. For this reason, more quantitative analysis of the cantilever response as a function of homocysteine concentration could not be performed here.

As discussed previously (Section 2.3.2), the cantilever displacement during homocysteine binding can be estimated by counting the number of interference fringes in the microscope image. Figure 4.12 shows three estimated displacements versus the measured relative power increase (increase in power divided by initial power) for a 140 μm long cantilever in response to 5 mM homocysteine. The three data points were obtained at different times after sample introduction. The vertical error bars are due to the resolution limit of the fringe counting measurement (~ 120 nm in this case).

The figure also shows the theoretical relative power increase based on the coupling function given by Equation 2.13. The curve was obtained by dividing the theoretical increase in coupling coefficient at varying displacements by the coupling coefficient at the initial offset. The initial cantilever tip height used in this calculation was estimated by the fringe counting method. The measured data agrees reasonably well with the coupling model. This suggests that the model can be used to translate changes of output power into cantilever displacement. For small displacement, the change in power is approximately linear with displacement. The slope near the origin of the plot is 1.52; therefore, each nanometer of displacement corresponds to 0.66% change in power (reciprocal of the slope). The coupling model can readily be extended to cantilevers with different initial offsets.

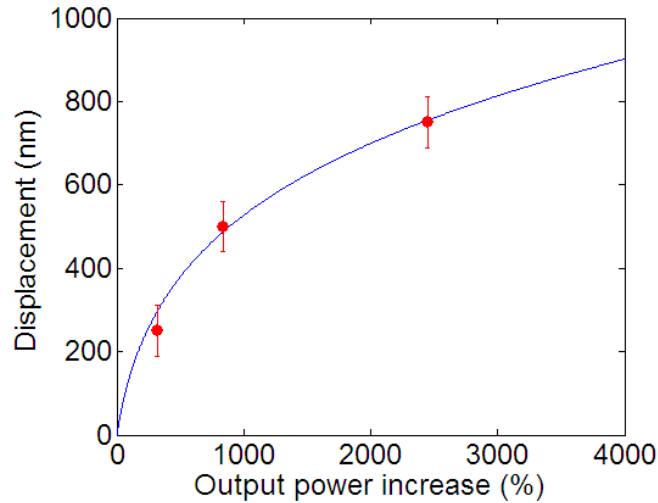


Figure 4.12: Measured (dots) and theoretical (line) displacement of a cantilever vs. relative increase in optical power. The cantilever length, initial tip height, and propagation gap are 140 μm , 2.2 μm , and 2 μm respectively. It is tested in 5 mM homocysteine solution.

4.4.3 Interferometric Measurements

The waveguide cantilever also forms an interference pattern very similar to that of the interferometric cantilever. The pattern was used in the previous section to roughly estimate the tip height and differential displacement by counting the number of fringes. However, this method has poor resolution limited by the user's ability to recognize changes of less than one fringe. As discussed in Section 2.3, the interferometric cantilever relies on image processing software to determine the fringe shift and displacement more precisely. The same software was used here to analyze the waveguide cantilever while measuring its output power. This allows the theoretical coupling model to be verified with more precise displacement values than the ones in Figure 4.12.

The microscope images of the waveguide cantilever have lower quality than those of the interferometric cantilever, and the resulting measurement error is larger. The interferometric device was tested with a high-magnification microscope (Chapter 5).

This tool could not be used for the waveguide device due to the constraints of the optical testing setup, which includes XYZ positioning stages. Instead, a low-magnification, long-working distance microscope was selected, and the quality of the images was lower. Nevertheless, the image processing software greatly improved the precision of the displacement measurements compared to the simple fringe counting approach. The procedure for interferometric image analysis is not described here to avoid repetition; it is discussed in detail in Chapter 5.

Figure 4.13 shows the output power from a waveguide cantilever along with the displacement measured by analyzing the interferometric images. The image acquisition was synchronized with the recording of optical power. The vertical dashed lines represent the times at which each image was acquired. Overall, the optical power and displacement seem well correlated. The shapes of the curves differ, but that is because the theoretical output power is not a linear function of displacement; rather, it is a Gaussian as described in Chapter 2.

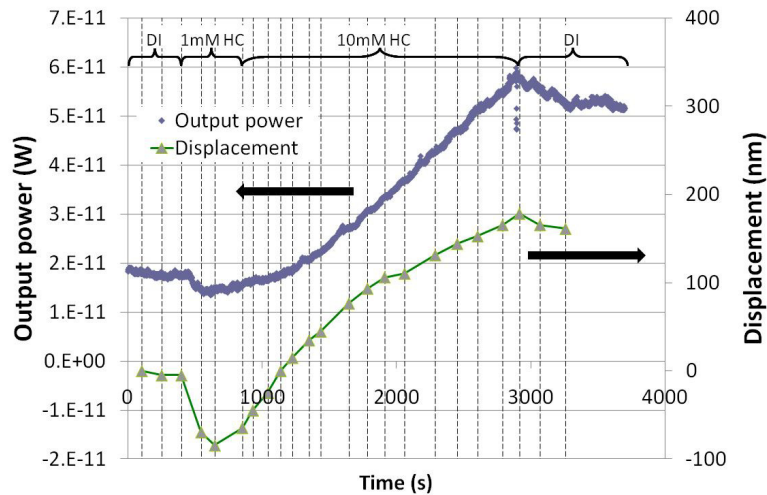


Figure 4.13: Optical output power of a waveguide cantilever and displacement measured by interferometry in response to homocysteine samples. The cantilever length, initial tip height, and propagation gap are 120 μm , 2.48 μm , and 2 μm respectively.

It was shown in Figure 4.10 that hydrochloric acid solutions cause the cantilever to bend down, possibly due to shrinking of the SU-8 in low pH. This effect was used to move the cantilever reversibly over a larger range of displacements than what was demonstrated with homocysteine samples. The displacement was again measured by interferometry while the output power was being recorded. Figure 4.14 shows the results of one such experiment. Here, HCl solutions with concentration ranging from from 70 mM to 1.37 M were introduced sequentially into the device following a DI water baseline measurement. The HCl concentration as a function of time is also plotted in the figure. Again, the displacement and optical power have different shapes but are correlated well.

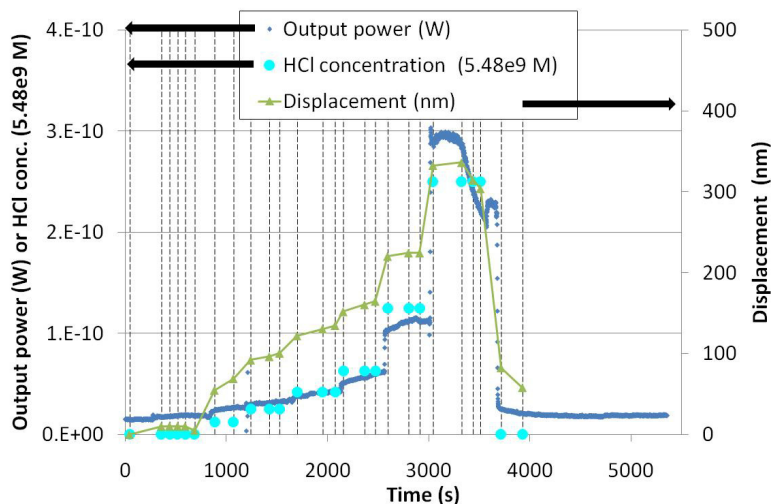


Figure 4.14: Optical output power of a waveguide cantilever and displacement measured by interferometry in response to dilute hydrochloric acid samples. The cantilever length, initial tip height, and propagation gap are 120 μm , 2.48 μm , and 2 μm respectively.

The measured power at the time of each image acquisition (i.e. the dashed line crossings) was extracted from Figure 4.13 and Figure 4.14. The percentage power increase was calculated from these data by dividing each power value by the initial

power. The resulting power increase was plotted versus the corresponding displacement measured by interferometry as shown in Figure 4.15. The theoretical curve in the figure is obtained from coupling function given by Equation 2.13.

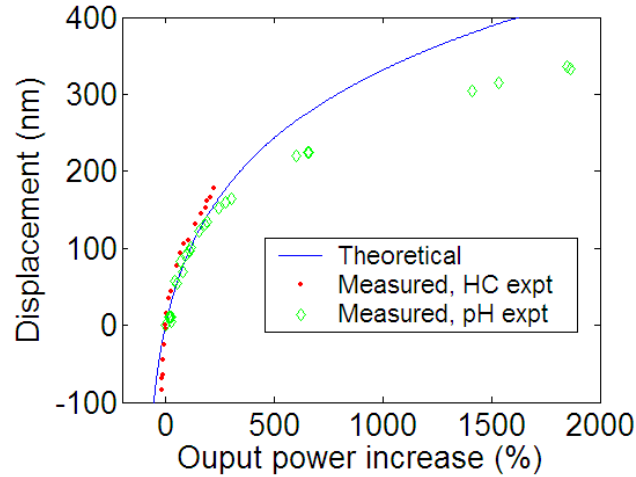


Figure 4.15: Measured and theoretical displacement versus relative power increase of a waveguide cantilever. The measured values are obtained from the homocysteine (HC) and pH experiment data shown in Figure 4.13 and Figure 4.14.

The measured data agree very well with the model for small displacements of < 200 nm. For larger displacements, there is an increased discrepancy. This is likely due to effects which the model fails to take into account (e.g. higher order modes, sidewall angle and roughness of the waveguide facet). Some error in the interferometric displacement measurements and drift in the power coupling may also contribute to the discrepancy. Nevertheless, the agreement throughout the displacement range is reasonably close. In particular, note that the measured data for the pH and HC experiments almost overlap over their common displacement range. These results further support the claim made with Figure 4.12 that the power changes can be translated into displacement.

4.5 Detection of Enzymatically Produced Homocysteine

The biosynthetic pathway of the bacterial quorum signaling molecule AI-2 was described in detail in Section 1.3.1. It consists of the enzymes Pfs and LuxS. The former converts the precursor SAH into SRH and adenine; the latter converts SRH into AI-2 and homocysteine. The sensors developed in this dissertation are aimed at detecting homocysteine, thereby indirectly assaying the activity of the AI-2 synthesis pathway. The previous section described the detection of homocysteine samples obtained by dissolving commercially available powder. In the present section, it is demonstrated that the waveguide cantilever sensor can detect homocysteine produced by the bacterial enzymes as well.

4.5.1 External Enzymatic Synthesis

For the first enzymatic experiment, the homocysteine/AI-2 sample was synthesized externally by my collaborator Dr. Rohan Fernandes as described in detail in elsewhere [45]. Briefly, the enzymes Pfs and LuxS were isolated from genetically modified *E. Coli* bacteria. The enzymes are actually combined in one large module, including a Histidine tag, LuxS, Pfs, and a Tyrosine tag (hence the name HLPT). The enzymatic module is assembled on chitosan-coated magnetic nanoparticles (also called chitosan-mag or CM). The resulting enzymatic nanoparticles (HLPT-CM) were then added to a 1 mM solution of the precursor SAH in 10 mM phosphate buffer (PB) with pH 6, and the mixture was allowed to react. Next, the nanoparticles were precipitated out of the solution using a permanent magnet. The supernatant was extracted and used as the sample for cantilever detection. Therefore, the sample contains a mixture of SAH, adenine, SRH, AI-2, and homocysteine dissolved in PB.

The resulting homocysteine concentration is unknown, but it is certainly less than 1 mM (the starting concentration of SAH).

The response of the waveguide cantilever sensor to the sample described above is shown in Figure 4.16. The SAH solution in PB may have a slightly different refractive index than water. Therefore, this solution was introduced into the device as a control liquid rather than DI water to obtain the baseline reading. The sample causes a power increase of approximately 150%. It is followed by the control solution, which does not cause any appreciable change in power output. This confirms that the measured response is due to permanent cantilever bending, and it is not the result of a refractive index change.

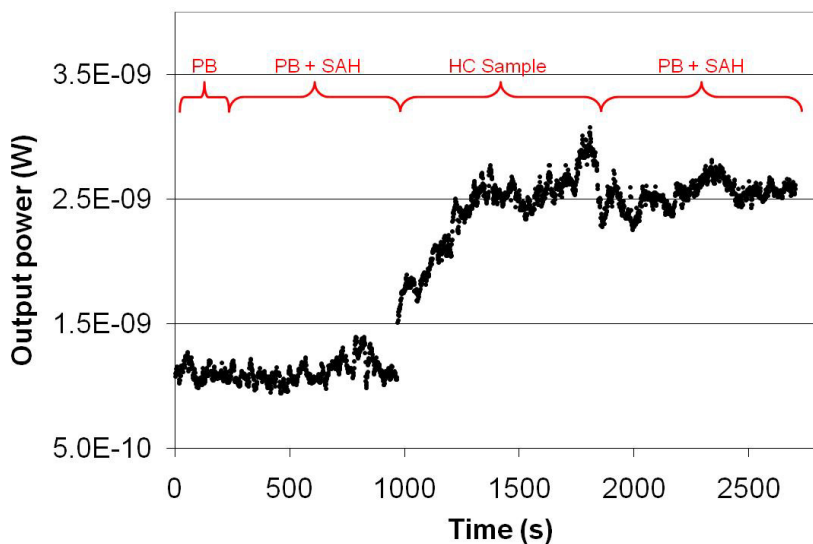


Figure 4.16: Response of a waveguide cantilever to a homocysteine sample synthesized by the bacterial quorum sensing enzymes. The sample was prepared externally to the device. The cantilever length, initial tip height, and propagation gap are 110 μm , 2.2 μm , and 4 μm respectively.

4.5.2 Enzymatic Synthesis in Microfluidics

For the second enzymatic experiment, Pfs and LuxS were immobilized in the Tygon microfluidic tubing at the input of the packaged device. SAH solutions

entering the device are converted into homocysteine, which is detected downstream by the cantilever. The same enzymatic magnetic nanoparticles (HLPT-CM) were used as before, but the experimental procedure was different.

HLPT and CM solutions were prepared by Dr. Rohan Fernandes as described in detail elsewhere [45] with concentration of 4.84 mg/mL and 3.86 mg/mL respectively. The solutions were mixed in a ratio of 1:23.5 and diluted with 10 mM phosphate buffer (pH 6). The resulting concentrations of HLPT and CM were 0.053 mg/mL and 1 mg/mL respectively. The mixture was incubated at room temperature for 1 hr; this step allows the HLPT enzyme module to attach to the chitosan-coated magnetic nanoparticles.

The HLPT-CM solution was injected into a 10 cm long piece of the Tygon tubing used for fluidic input to the device. A magnetic field was applied perpendicular to the tube with a permanent magnet for ~5 min. The field causes some HLPT-CM to migrate to the wall of the tubing and adsorb there physically, forming a visible film of nanoparticles (Figure 4.17). The magnet is removed and the HLPT-CM solution is flushed from the tubing with clean buffer solution and DI water to remove any loosely bound particles from the walls. A visible film of adsorbed particles remained even after extensive rinsing. The functionalized tube was attached to the input capillary of the waveguide cantilever package. This method enables assembly of the enzyme in the microfluidic path while preventing the HLPT-CM solution from contacting the sensitive cantilever surface and possibly contaminating it.

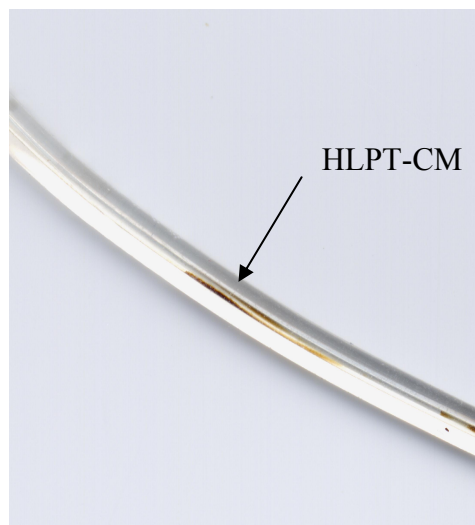


Figure 4.17: Photograph showing HLPT-CM enzymatic nanoparticles adsorbed on Tygon tubing inner wall. The tubing has inner diameter of 380 μm and outer diameter of 2.31 mm.

An SAH solution was prepared by dissolving SAH powder (Sigma Aldrich, USA) in 10 mM sodium phosphate buffer (PB) with pH 6. The solution was introduced into the device after flowing PB for 10 min to establish a baseline signal. Figure 4.18 shows the optical response of the cantilever to the SAH for two different concentration and flow rate conditions. The concentration of homocysteine near the cantilever depends on the SAH concentration and the residence time of SAH at the enzymes, which is inversely proportional to flow rate. In Figure 4.18, the cantilever response to 100 μM SAH flowing at 10 $\mu\text{L}/\text{min}$ is undetectable. However, increasing the concentration to 1 mM and reducing the flow rate to 2 $\mu\text{L}/\text{min}$ causes a measurable change in power by approximately 360%. The SAH sample is followed by phosphate buffer, which does not appreciably change the output power. This verifies that the response is caused by permanent cantilever bending and not by a temporary refractive index change.

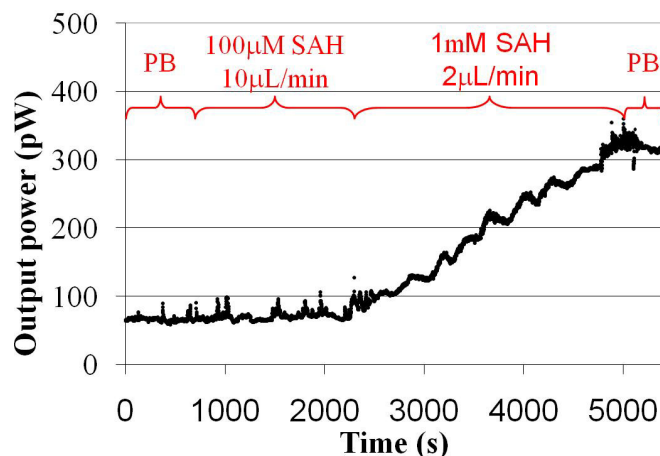


Figure 4.18: Response of a waveguide cantilever to SAH introduction; the input tubing is functionalized with Pfs and LuxS enzymes. The cantilever length, initial tip height, and propagation gap are 110 μm , 2.2 μm , and 2 μm respectively.

The curve in Figure 4.18 generally looks noisier than the responses measured before for homocysteine obtained from powder. It also has a different shape (ramp instead of exponential rise to max). One possible reason for this is that the enzymatic capacity and resulting homocysteine concentration may be changing over time. On one hand, the enzymes may become less active due to denaturation; on the other hand, more enzyme area may become exposed to the solution due to continuous washing. These factors may cause fluctuations in the homocysteine concentration over time even though the incoming SAH concentration is kept constant. In addition, some of the nanoparticles adsorbed on in the tubing may gradually detach and flow into the chip, contaminating the cantilever surface and interfering with the propagating light.

A control SAH experiment was performed using a device whose microfluidic input tubing was not functionalized with enzymatic particles. Figure 4.19 shows the optical response of this cantilever to 1 mM SAH flowing at 2 $\mu\text{L}/\text{min}$. There is a slight downward trend in the power, probably caused by XYZ stage drift; however,

there are no major changes upon the injection of SAH. Therefore, the cantilever bending shown previously in Figure 4.18 was not caused by the SAH itself, and it must have been caused by an enzymatic product. This result is expected since SAH does not have free thiol groups that could bind to the cantilever surface.

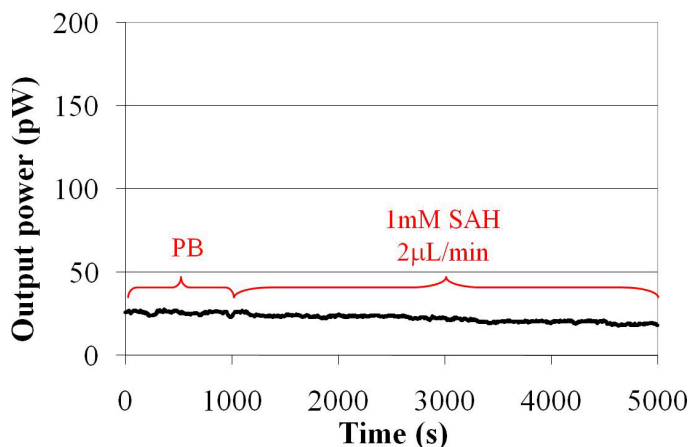


Figure 4.19: Response of an optical cantilever to SAH introduction; there are no enzymes in the tubing. The cantilever length, initial tip height, and propagation gap are 110 μm , 2.2 μm , and 2 μm respectively.

4.6 Discussion

The cantilever displacement in each experiment can be estimated from the measured power change using the theoretical coupling function. The results shown in Figure 4.12 and Figure 4.15 earlier confirmed that the displacement obtained by this method is in good agreement with the displacement measured by fringe counting. Table 4.1 summarizes the results from the previously described homocysteine detection experiments. Each row lists the figure in which the result was presented, the sample concentration, the characteristics of the cantilever, the maximum measured power increase, the calculated displacement, and the calculated surface stress. The homocysteine concentration in the case of the enzymatically produced samples is not known, and its upper bound is given instead (bottom two rows). The gap value listed

in column 3 refers to the gap between the cantilever and the output waveguide. The initial offset is the height of the cantilever above the substrate estimated by the fringe counting method. The displacement in column 8 is calculated from the optical power increase using the theoretical coupling function (Equation 2.13) and the measured initial offset. The stress value in column 9 follows from the mechanical sensitivity of each cantilever (Equation 2.1).

Table 4.1: Summary of results from homocysteine detection experiments and estimated surface stress.

Figure	HC conc. (mM)	Gap (μm)	Length (μm)	Offset (μm)	Curvature (mm^{-1})	Power increase (%)	Displacement (nm)	Surface stress (N/m)
4.7	10	4	140	2.2	0.22	1150	698	0.15
4.8	5	2	110	2.2	0.36	800	480	0.16
4.9	1	4	110	2.2	0.36	400	413	0.14
4.10	10	2	70	0.75	0.31	30	170	0.14
4.11	5	2	140	2.2	0.22	2400	750	0.16
4.12	10	2	120	2.48	0.34	230	178	0.05
4.15	< 1	4	110	2.2	0.36	150	225	0.08
4.16	< 1	2	110	2.2	0.36	360	318	0.11

As discussed in Section 4.4.2, the final surface stress caused by homocysteine assembly should not depend on the solution concentration (only the rate of assembly depends on it). The surface stress values in Table 4.1 are in reasonable agreement. Some variation between devices is to be expected since the thiol layer density depends on gold surface properties [140]. Interestingly, stresses in the range of 0.08 N/m to 0.25 N/m have been reported for several thiol compounds with varying chain lengths [137]. The measured values for homocysteine here are on the same order of magnitude. The only value that is considerably lower than the rest is that for Figure 4.13 in row 6 in the table. This may be due to contamination of the gold layer.

The theoretical mechanical and optical sensitivity of the cantilevers may be inexact due to deviations of the actual device dimensions and material properties from

the assumed values. As a result, the calculated cantilever displacements and surface stresses are only approximate. For typical detection applications, however, finding the exact cantilever displacement or surface stress is not needed. It is only necessary to compare the results of different experiments; these results can be given in terms of relative power change. All cantilevers can be fabricated to have the same mechanical and optical sensitivities. Therefore, comparisons in terms of optical power change can be made, although the exact conversion to surface stress is not known. Note that the conventional cantilever readout method based on position sensitive detectors [86, 137] also gives the results in terms of another parameter (detector voltage). In that case, the conversion to cantilever displacements is also not exact.

The concentration-dependent response in Figure 4.11 suggests that the device can be calibrated to measure concentrations of homocysteine quantitatively. However, it was found that the concentration dependence is not repeatable and cannot be reliably used to determine concentration. Although the rate of binding depends on the concentration, the final thiol surface density is almost independent of concentration [139]. The rate of binding is influenced by random phase transitions [140] that occur after the initial binding, and its concentration dependence varies considerably between experiments. Importantly, the study of bacterial quorum sensing that this device is developed for does not require concentration measurements. For this application, it is sufficient to detect only the presence of homocysteine.

The minimal detectable displacement of the cantilever depends on the noise power. As explained previously (Section 2.2.3), the main source of noise here is the drift of the XYZ positioning stages, and it causes power variations on the order of 3%

over a period of 1000 s. Therefore, the minimal measurable power change is approximately 3% for an experiment of that duration. This translates to a minimal detectable displacement of 6 nm by using the theoretical coupling model plotted in Figure 4.12 for a cantilever with initial offset of 2.2 μm . The corresponding minimal surface stress is 1.3 mN/m. In comparison, the minimal detectable stress for the waveguide cantilever reported by Nordstorm *et al.* is 200 mN/m [33, 108].

Clearly, the homocysteine detection results show more power variations in addition to the slow stage drift. This could be caused by fluctuations in the liquid flow, particles passing through the fluidic channel, or detachment of homocysteine molecules from the cantilever surface. However, these variations occur over a timescale of several seconds and can be filtered out by averaging. The stage drift occurs on a timescale similar to that of the cantilever response, and therefore it is the determining factor of the detection limit.

4.7 Summary

This chapter described the testing procedures and results for the waveguide cantilever sensor. The device was first characterized optically and then used to detect homocysteine samples. The total measured optical loss was 25 dB, while the propagation loss in the waveguide was 7 dB/cm. The typical power variation due to the XYZ stage drift was found to be on the order of 3% over a period of 1000 s. The cantilever coupling function was tested over a large displacement range by pushing the device with a microprobe. The result was in reasonable agreement with the theoretical coupling model. The device was used for detection of homocysteine prepared from commercially available powder and also for enzymatically produced

homocysteine. The estimated surface stress in all experiments was similar, and it was close to values reported in literature for other types of thiol compounds. A minimal homocysteine concentration of 10 μM was detected. Interferometric displacement measurements were also performed in conjunction with recording of the output power. These results verified the theoretical coupling model over small displacement ranges. It was shown that for the representative cantilever geometry, 1 nm of displacement causes 0.66% change in optical power. The minimum detectable displacement and surface stress were estimated to be 6 nm and 1.3 mN/m, respectively.

Chapter 5: Interferometric Cantilever Testing

5.1 Introduction

This chapter presents the characterization of the interferometric cantilever sensor and its use for detection of homocysteine. The testing setup and image acquisition procedures are explained first. In particular, the effect of different light sources on the interference pattern contrast is studied. The random error in the measurements is tested under different experimental conditions. Next, solutions with varying pH are used to induce reversible cantilever displacement. The responses of multiple devices to pH are measured in parallel. Next, two types of homocysteine detection experiments are performed: using samples from commercially available powder or using enzymatically produced samples. These experiments are similar to the ones described in Chapter 4 for the waveguide cantilever but are performed with several devices in parallel. In addition, it is demonstrated that enzyme denaturation significantly alters the sensor response.

5.2 Experimental Setup

Unless otherwise noted, the measurements were performed with fully packaged devices as described in Section 3.7.2.2. The testing setup is illustrated in Figure 5.1. First, DI water is pipetted in the input wells and sucked into the microfluidic channels with a manually operated syringe connected to the output tubing. Initial images of each cantilever are taken with the microscope by translating the stage. Then, the samples are pipetted in each input well and sucked into the respective channel. Care is taken to avoid overfilling the wells and cross-contaminating the samples. Next,

images of the displaced cantilevers are taken and saved. The initial and final images are analyzed by the method described in Section 2.3.2 to extract the displacement.

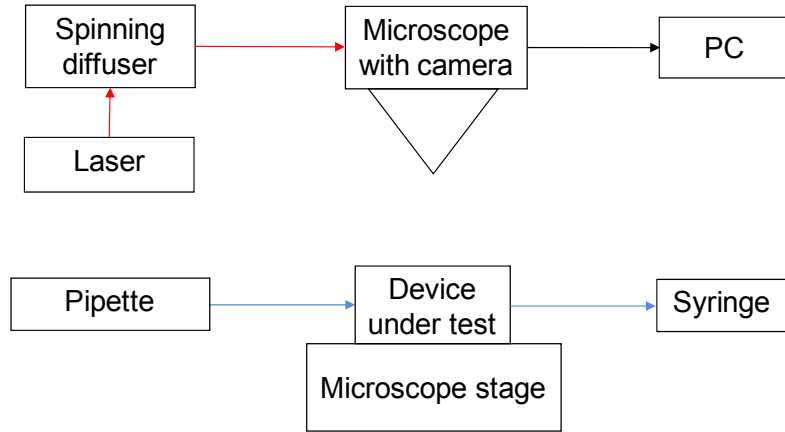


Figure 5.1: Block diagram of testing setup used to characterize interferometric cantilever sensor.

All images are acquired at either 20X or 40X optical magnification using a microscope with a manual X-Y stage (Mitutoyo FS70). The camera has 3840 by 3072 pixels (Nikon DXM1200). The resulting image resolution is either 9 or 18 pixels/ μm . The microscope's incandescent light source was replaced with a 660 nm diode laser. The laser beam is fed through a spinning diffuser to reduce its spatial coherence and guided into the microscope port with a fiber optic bundle. The advantages of this custom-made light source are explained in the next section.

5.3 Microscope Light Source

The spectral width of the microscope light source significantly affects the characteristics of the interference pattern. The expression given by Equation 2.21 assumes a light source with a single wavelength (i.e. perfectly monochromatic).

However, practical light sources have a range of wavelengths. The intensity of the interference pattern resulting from light with arbitrary spectral width is given by Equation 5.1. Here, τ is the time difference between the beams reflecting off the

cantilever and off the substrate as illustrated in Figure 2.16; where $g(\tau)$ is the autocorrelation function. For spectrally narrow sources bandwidth much smaller than the central frequency ($\Delta\nu \ll \nu_0$), the interference pattern can be approximated with Equation 5.2 [121].

$$\text{Equation 5.1} \quad I_{refl} = I_1 + I_2 + 2\sqrt{I_1 I_2} \operatorname{Re}\{g(\tau)\}$$

$$\text{Equation 5.2} \quad I_{refl} \approx I_1 + I_2 + 2\sqrt{I_1 I_2} |g(\tau)| \cos(2\pi\nu_0\tau)$$

In the case of monochromatic light, the autocorrelation function is $g(\tau) = \exp(i2\pi\nu\tau)$ and the intensity reduces to the expression in Equation 2.21. However, in the general case, $g(\tau)$ is a decreasing function with maximal value at $\tau = 0$ and negligible value for $\tau > \tau_c$ [121]. Here, τ_c is the coherence time, which is related to the bandwidth of the light source by $\tau_c \approx 1/\Delta\nu$; the corresponding coherence length is $l_c = c\tau_c$. If the optical path difference (OPD) between the interfering beams increases beyond the coherence length, the third term in Equation 5.2 goes to 0 and the interference pattern vanishes. To obtain a high-contrast interference pattern, the coherence length must be much larger than the OPD.

As shown in Figure 2.16, the optical path difference between the interfering beams is twice the cantilever-to-substrate distance. Table 5.1 lists estimated coherence lengths for several different light sources along with the maximum cantilever tip height that results in visible interference fringes. The first entry is for an incandescent light bulb, which is the standard light source for most microscopes. Cantilever tip heights of approximately 500 nm are sufficient to wash out the interference pattern in this case. The second entry in the table is for a red light emitting diode (LED) that was used to replace the original source. This resulted in

visible fringes for large cantilever offsets, but the interference contrast was low. Therefore, a source with even higher coherence length is needed. The third entry in Table 5.1 is an example of a typical laser source. The given linewidth of 1 pm is achievable even by low-cost semiconductor lasers [141]. This should result in sufficiently coherent illumination for any practical cantilever offset.

Table 5.1: Coherence characteristics of different light sources that can be used for microscope illumination. The coherence lengths are adjusted for the refractive index of water (1.33).

Light source	Linewidth (m)	Bandwidth (Hz)	Coherence time (s)	Coherence length (m)	Cantilever max tip height (m)
Incandescent	300E-9	2.07E+14	4.84E-15	1.09E-06	5.46E-07
LED	40E-9	2.75E+13	3.63E-14	8.19E-06	4.09E-06
Laser diode (typical)	1E-12	6.89E+08	1.45E-09	3.28E-01	1.64E-01

Lasers have the unique capability of outputting high intensities over very narrow linewidths. However, laser beams are both spatially and temporally coherent. The spatial coherence is highly undesirable for this application because it results in a speckled image. As a coherent wavefront scatters off the sample surface, secondary wavefronts are generated that have a constant phase relationship with each other. They interfere and create a random-looking interference pattern known as speckle. This pattern severely degrades the sample image and prevents any interferometric measurements of heights.

Several methods have been demonstrated to reduce the speckle. Some authors have used optical feedback to trigger laser mode-hopping and average out the interference pattern[112]. Unfortunately, this approach greatly reduces the temporal coherence of the light and would be counterproductive for our application. Others have demonstrated the use of mechanical motion to randomize the laser beam wavefront over space and time [142, 143]. For example, the light is passed through a

multimode optical fiber vibrated by a piezoelectric transducer or through a rotating ground disk. Since the frequency of mechanical motion is low, the temporal coherence of the light is not affected. Although these methods for speckle reduction have been reported in literature, there are no commercially available instruments that implement them. For this reason, I developed a custom device. I chose the rotating disk approach due to its simplicity.

Figure 5.2 shows the assembled light source. The laser is a 130 mW single-mode laser diode with wavelength 660 nm (Mitsubishi Electric, Cypress, CA). It is mounted on a heat sink and cooled by a fan. The laser output is collimated by a lens and passed through a diffusive plastic disk mounted on a 2000 rpm electric motor. The light is then collected by a fiber bundle and guided to an illumination port of the Mitutoyo FS70 microscope. Approximately 90% of the laser light is lost in this setup due to scattering by the rotating disk. However, the coupled light is still sufficient for imaging at any magnification, and the laser diode is run well below its peak power.

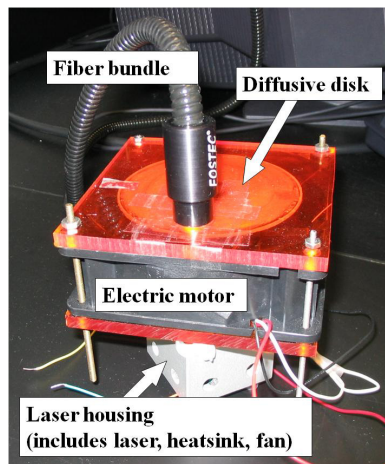


Figure 5.2: Custom-made laser illumination source with rotating diffusive disk.

The frequency of random modulation of the light by the disk depends on the roughness profile of the disk and the rotation speed. We estimate that this frequency

is less than 1 MHz, which would limit coherence time to 1 μ s and coherence length to 300 m. Since our application requires coherence length only on the order of several μ m, any limitation of temporal coherence by the spinning disk is insignificant. At the same time, the 1 μ s period of the random modulation is much shorter than the exposure time of the camera (several seconds). Therefore, the speckle pattern appears averaged out in the acquired image. Figure 5.3 shows images of a sample illuminated by the laser with the disk rotation off or on. In the first case, the speckle degrades the image severely; in the second case, the speckle is eliminated, allowing the sample features to be clearly resolved. These images were acquired with an interferometric optical profiler (Veeco NT1100) rather than the microscope described previously; they are used here only to illustrate the speckle problem and its solution.

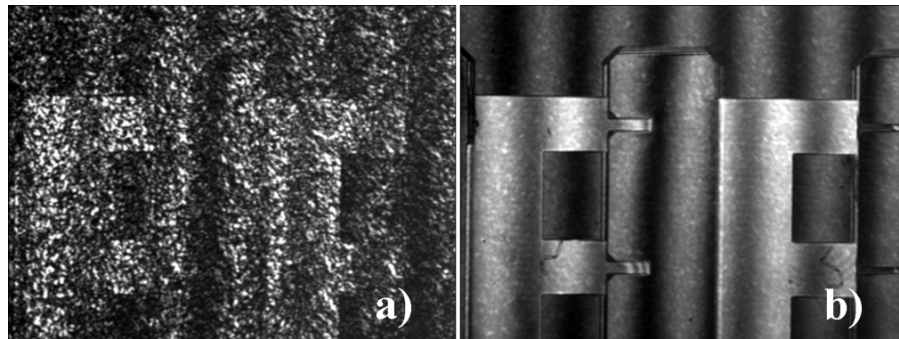


Figure 5.3: Image of a MEMS sample taken with laser illumination. a) The light is temporally and spatially coherent. b) The light is decohered spatially by passing it through the rotating disk.

The spatially decohered laser source resulted in much better contrast in images of the interferometric cantilever than the LED described in Table 5.1. The improvement is evident from the intensity shown in Figure 5.4. The higher fringe modulation increases the precision of fringe shift measurement and the resulting cantilever displacement estimate. For this reason, the laser illumination was used for all subsequent interference cantilever testing.

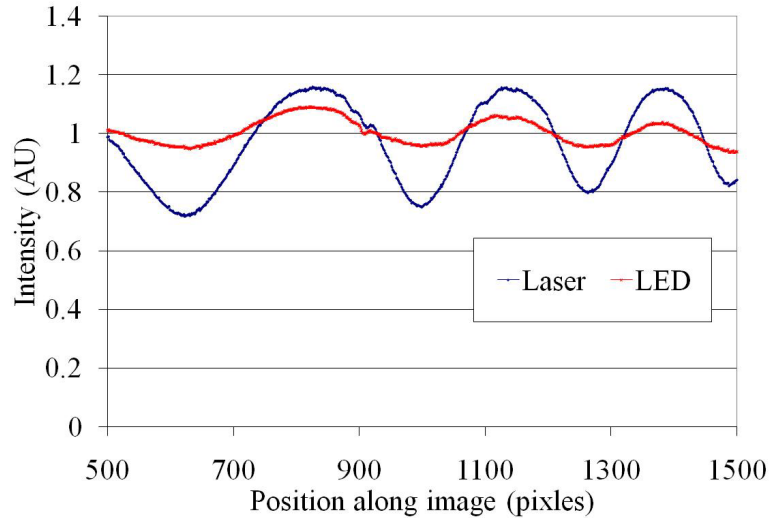


Figure 5.4: Measured intensity profile from cantilever images obtained with laser or LED illumination at 40X optical magnification.

The interference contrast is also affected by the aperture diaphragm setting of the microscope. This setting controls the range of angles over which the sample is illuminated. The simplified schematic in Figure 2.16 suggests that the incident beams are normal to the sample. In reality, they have a range of angles depending on the numerical aperture of the microscope. A slightly different interference pattern is formed for each angle; the resultant pattern is the sum of these contributions and therefore has reduced contrast. Since decreasing the aperture setting minimizes the range of illumination angles, it should enhance the interference contrast. This effect is confirmed by the data in Figure 5.5. The main disadvantage of a small aperture is that it considerably decreases the illumination intensity. However, the laser used in this work provides sufficient power and allowed me to use very small aperture settings.

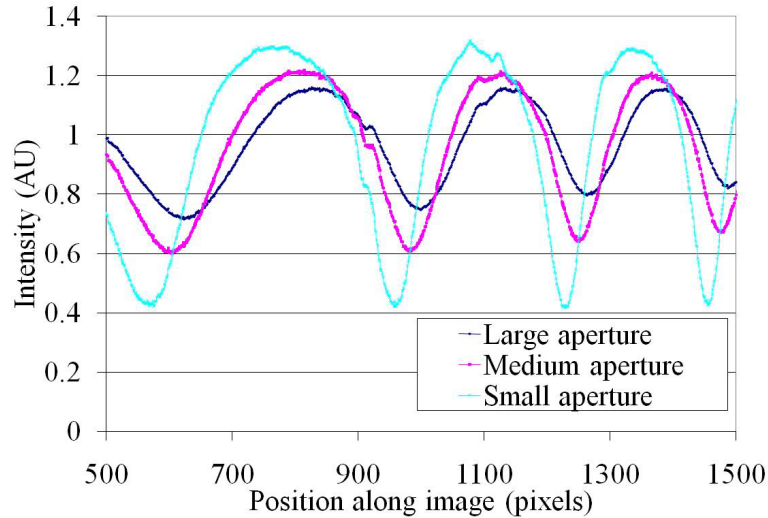


Figure 5.5: Measured intensity profiles from cantilever images obtained with different settings of the microscope’s aperture diaphragm at 40X optical magnification.

The results in Figure 5.5 also show that changing the aperture shifts the interference fringes laterally. This shift could be misinterpreted as being caused by cantilever displacement. Therefore, it is important to use exactly the same aperture setting for the initial and final images of the cantilever.

5.4 Measurement Precision

It was explained in Section 2.3.4 that the main source of random displacement error is the fringe shift measurement error. The latter is caused by quantization of the image, changes in microscope focus, and translation of the microscope stage combined with nonuniform illumination. The quantization error was theoretically estimated to be ± 0.5 pixels (Section 2.3.4). The other two contributions are characterized below.

Table 5.2 shows the typical random error caused by microscope refocusing and stage translation. Three types of measurements were performed: no motion, refocusing, and refocusing with stage translation. In each case, 10 images of the same

cantilever in DI are taken at 40x magnification, and the fringe shift Δz is extracted by the algorithm described previously (Section 2.3.3). The first column in the table is the average of the measurements, and the second is the standard deviation. The third column is the standard deviation of vertical displacement Δd calculated from the fringe shift (Equation 2.23) using a cantilever slope of 0.02 and image resolution of 18 pixels/ μm . The fourth and fifth columns show the average values of normalized cross-correlation maxima, which are calculated to register the image and find fringe shift as discussed in Section 2.3.3. These values serve as figures of merit, indicating the quality of the image alignment (cross-correlation of 1 would mean perfect alignment).

Table 5.2: Average and standard deviation of 10 fringe shift measurements performed with and without microscope refocusing and stage motion.

	Mean Δz (pixels)	Std. Dev. Δz (pixels)	Std. Dev. Δd (nm)	Max cross-corr. alignment	Max cross-corr. fringe
No motion	0	0	0	0.9795	0.9895
Refocusing of microscope	-0.4	0.52	0.58	0.9791	0.9877
Stage translation and refocusing	0.2	0.79	0.89	0.9562	0.9828

In the no-motion case, all 10 images are taken without touching the microscope or the chip. The measured fringe shift for every image is 0. This means that the random error is below the camera resolution. Therefore, the errors due to laser wavelength fluctuation and camera noise are negligible compared to the quantization error. For the refocusing measurements, the microscope focus is adjusted before every image acquisition without translating the stage. Some error is observed, as indicated by both the average fringe shift and the standard deviation. For the third type of measurements, the microscope is refocused and the stage is moved so that the cantilever position in the image changes. This procedure emulates actual detection

experiments, in which the stage is translated in order to image multiple cantilevers. Here, the fringe shift error increases further, and the standard deviation becomes ~ 0.8 pixels. Based on this, it can be concluded that the minimal detectable fringe shift is 0.8 pixels. This corresponds to approximately 1nm detectable cantilever displacement and ± 1 nm random displacement error. Table 5.2 also shows that the cross-correlation quality slightly decreases as more variability is introduced to the measurements by refocusing and stage translation. This trend is expected and agrees with the increased error.

As discussed in detail in Section 2.3.4, the other source of measurement error is the systematic error caused by approximating the curved cantilever with a straight line. That error is less than $\pm 6\%$ of cantilever displacement for the slope approximation method used in all experiments here (the more accurate slope approximation method can reduce the error further at the expense of slower image analysis). Therefore, the total error is dominated by the systematic error for large displacements and by the random error described above (± 1 nm) for small displacements. Accordingly, error bars of $\pm 6\%$ are added to all displacement plots in this chapter.

5.5 Response to pH Variation

It was shown previously in Figure 4.10 and Figure 4.14 that the gold coated SU-8 cantilever bends down in response to acidic solutions. This effect is probably due to deswelling of the polymer in low pH. The bottom of the cantilever is directly exposed to the solution and deswells more than the top, which is protected by the metal layer. This pH dependent behavior is used here to emulate the cantilever displacement that

would occur upon detection of a chemical or biological sample. Hydrochloric acid was dissolved in DI water to make solutions with a range of pH values from 0.86 to 4.16. Conveniently, the pH-induced bending is reversible, and the same device can be used for multiple samples without significant changes in response. In contrast, it was shown previously (Section 4.4.2) that the response of the cantilever to homocysteine samples is affected by contamination and decays considerably after several each use.

Three neighboring cantilevers were imaged in DI and then in samples with decreasing pH. There was period of 5 min between injecting the sample and acquiring the image in order to allow the cantilevers to reach equilibrium. For this experiment, a modified version of the PDMS layer was used such that all cantilevers are in the same fluidic channel. This reduced the number of sample injections needed by a factor of 3. The measured displacements are shown in Figure 5.6 (labeled as single-channel experiments). The error bars are based on the worst-case systematic error, which is 6% of the displacement as discussed in the previous section. The responses of the 3 devices are quite similar. The observed variations in pH sensitivity are probably due to slight differences in cantilever dimensions and material properties.

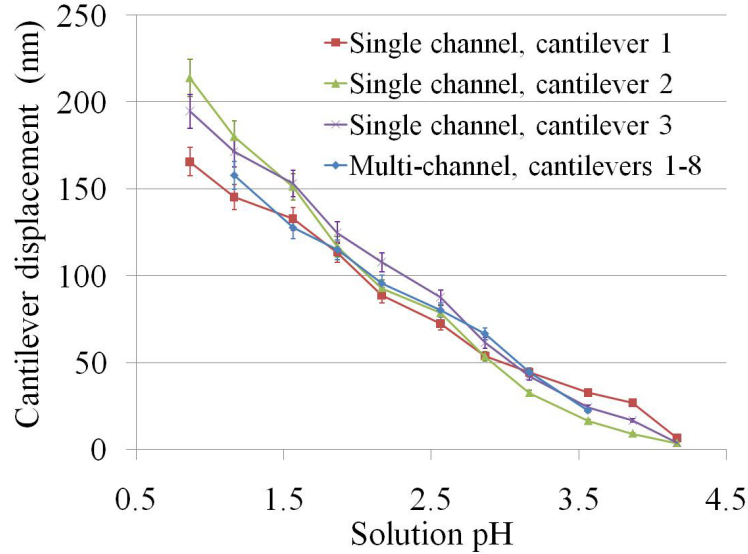


Figure 5.6: Measured displacements of cantilevers exposed to samples with different pH. All devices have a nominal length of 120 μm .

Next, a chip with 8 cantilevers was tested over the same range of pH values. In this case, each device was in a separate fluidic channel and was exposed to a single sample. In other words, the pH sweep was performed spatially instead of temporally. The measured displacements are also shown in Figure 5.6 (labeled as multi-channel experiment), and they agree reasonably well with the results from the single-channel test.

The refractive index of HCl is slightly higher than that of DI water, and it may introduce some error in the measurements. The highest refractive index here is that of the highest HCl concentration, which is 0.137M (pH 0.86). I found a reported value of 1.33502 for 0.239M HCl [144] and 1.33302 for water [144, 145]. This difference would cause an error of -3 nm in the displacement measurement (in our convention, downward displacement is positive). Therefore, the error due to the refractive index change is negligible in this case. However, it should be taken into account when measuring small cantilever displacements in highly concentrated samples.

To demonstrate the ability of the interferometric readout to measure larger numbers of cantilevers, I tested the response of 30 devices to a 2.74 mM HCl sample (pH 2.56). In this case, the chip was a large piece of wafer containing multiple dies, and it was used without PDMS packaging. The chip was placed in a Petri dish with DI to acquire the initial images; then it was transferred to a similar dish containing the sample to acquire the final images (after waiting at least 5 min for equilibration). Figure 5.7 shows the measured displacements. As in the case of Figure 5.6, the variation between devices is probably caused by differences in dimensions and material properties. The total measurement time for this experiment was approximately 20 min: 10 min for acquiring initial and final images and 10 min for image processing.

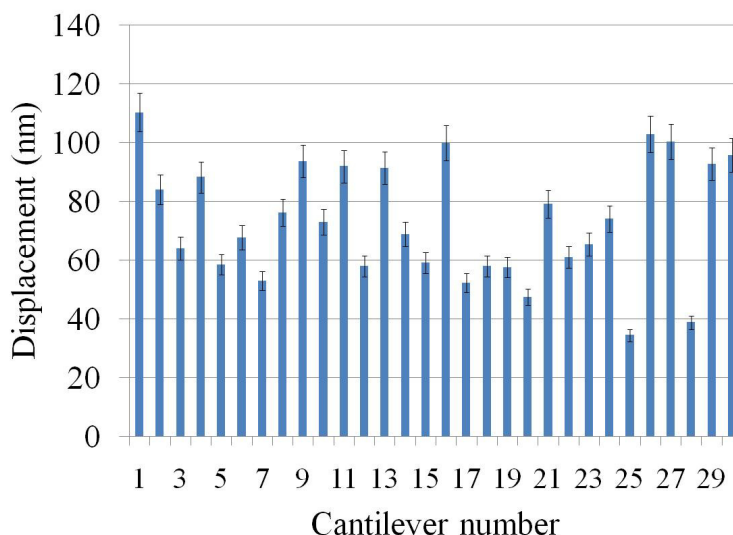


Figure 5.7: Measured displacements of 30 cantilevers exposed to a pH of 2.56 (unpackaged device). All devices have a nominal length of 110 μm .

5.6 Detection of Homocysteine from Powder

The interferometric cantilever was tested with solutions of varying pH in order to demonstrate the feasibility of measuring multiple devices in parallel in a reversible

manner. However, the actual application of the sensor is to detect homocysteine from the bacterial synthetic pathway of AI-2. As in the case of the waveguide based device described in Chapter 4, the interferometric cantilever was tested first with homocysteine samples prepared from commercially available powder. These results are presented in the current section. The next section will describe the testing with enzymatically produced homocysteine. All cantilevers used here have a nominal length of 110 μm .

5.6.1 Procedures

The samples were prepared as described in Section 4.4 for the waveguide cantilever. Briefly, homocysteine powder (Sigma Aldrich, USA) was dissolved in DI water to the desired concentration. Beyond the principle of displacement measurement, there are two notable differences in the testing of the interferometric and waveguide cantilevers. First, they have different packages. As discussed in Chapter 2, the waveguide device has one fluidic channel common to 8 cantilevers; the standard interferometric device has 8 channels in parallel, and each cantilever is in its own channel. Second, the sample flow conditions are different. The waveguide device is tested with continuous flow driven by a syringe pump. The interferometric device is tested with a stagnant sample; the liquid is sucked from the input well into the channel with a syringe and then left there for the duration of the experiment. This method greatly facilitates the injection of multiple samples in parallel compared to the continuous flow scenario.

5.6.2 Detection Results

A single cantilever was tested first to estimate the characteristic timescale of the detection. Figure 5.8 shows the measured response to 1 mM solution (the displacement is downward). It has the form of exponential rise to max, which is consistent with the first order kinetics model of the thiol assembly [139]. This response has a similar shape to the ones measured with the waveguide cantilever in Chapter 4. Approximately 32 min after the sample injection, the sample was flushed and replaced with DI water. Note that there is no abrupt change in displacement at that point, verifying that the difference in refractive index between DI and homocysteine solution is negligible. The displacement decreases gradually after that, probably due to some detachment of homocysteine from the gold surface.

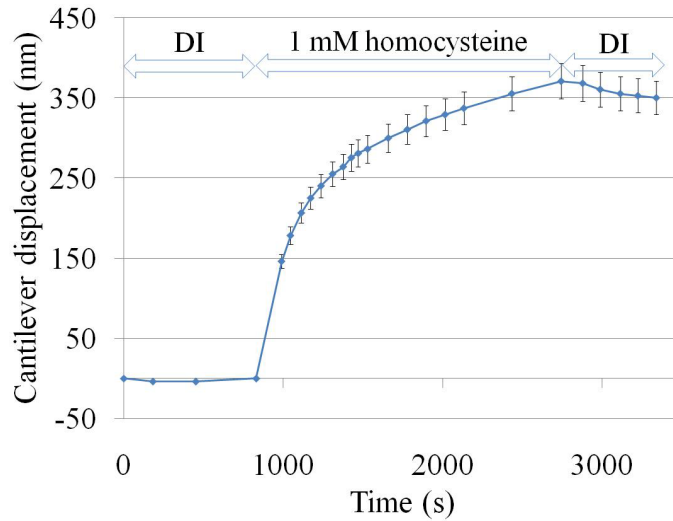


Figure 5.8: Response of an interferometric cantilever to 1mM homocysteine sample.

The measured max displacement is 370 nm. Using Equation 2.1 with our cantilever dimensions and the mechanical properties of SU-8 (Table 2.2), we estimate a surface stress of 0.13 N/m due to homocysteine assembly. This value is within the

range 0.08-0.25 N/m, which has been reported in literature for thiol compounds with varying chain lengths [137].

Next, 5 cantilevers on a single chip were tested with the same sample concentration (1mM) as shown in Figure 5.9. The responses are overall very similar, and the variations can be attributed to small differences in cantilever stiffness and gold surface properties. It has been shown that the density of thiol monolayers is greatly affected by defects and contamination of the gold layer [140]. Even larger variations in response were observed when using cantilevers with different cleaning histories (not shown here).

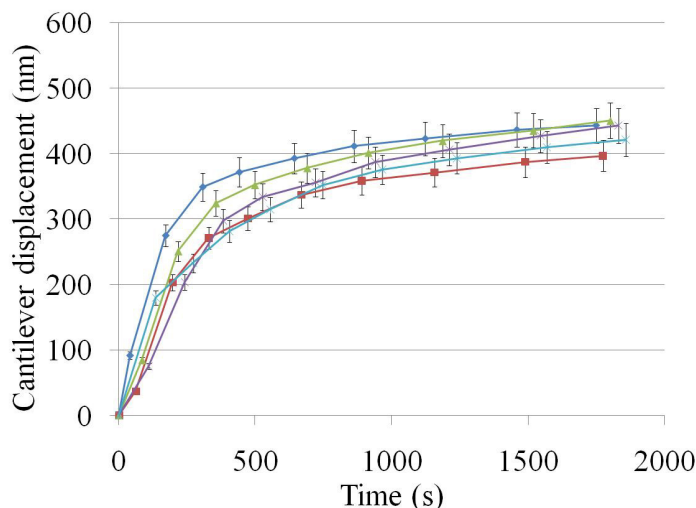


Figure 5.9: Responses of 5 identical interferometric cantilevers to 1mM homocysteine solutions. The samples are introduced at time 0.

The responses of multiple cantilevers on a single chip to different homocysteine concentrations were also tested. There is a clear trend of increasing displacement with concentration (Figure 5.10). This kind of behavior is expected based on the first order kinetics model of thiol assembly [139], which predicts that the rate of surface binding increases with concentration. Therefore, the cantilever response can potentially be used to roughly estimate homocysteine concentration if the measurement time is kept

constant. The variability between devices evident in Figure 5.9 ultimately limits the resolution of concentration measurements. As mentioned previously in Section 4.4.2, the study of bacterial quorum sensing does not require concentration measurement. For this application, it is sufficient to detect the presence of homocysteine.

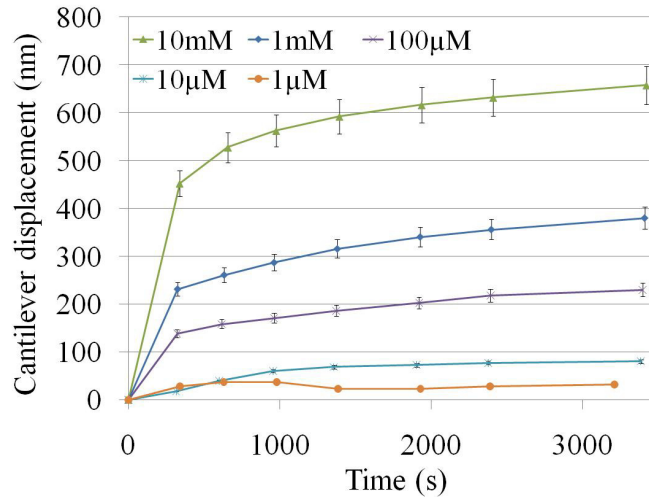


Figure 5.10: Responses of 5 identical interferometric cantilevers to homocysteine solutions with varying concentrations. The samples are introduced at time 0.

Chapter 4 described attempts of cleaning and reusing the waveguide cantilever sensors with dilute hydrochloric acid. The conclusion there was that the homocysteine is partially removed by cleaning, but the device becomes contaminated and its response decays after each use. A similar behavior was observed in the case of the interferometric device. Figure 5.11 shows responses of an interferometric cantilever to a 1 mM homocysteine sample after repeated cleaning with 1% w/w HCl for at least 5 min. The displacement becomes significantly lower with each use. Therefore, the sensor is not reusable. As in the case of the waveguide cantilever, this limitation is acceptable since the device is compatible with MEMS batch microfabrication and can be made at extremely low cost.

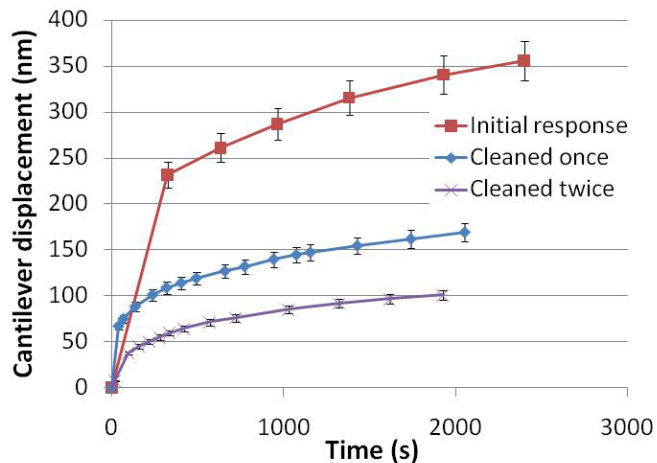


Figure 5.11: Responses of an interferometric cantilever to 1 mM homocysteine solution after repeated cleaning. The sample is introduced at time 0.

5.7 Detection of Enzymatically Produced Homocysteine

Finally, the interferometric cantilever was demonstrated for its intended application (detecting homocysteine from the bacterial synthetic pathway of AI-2). This pathway was described in detail in Section 1.3.1, and its output was detected with the waveguide cantilever in Section 4.5. Here, samples produced by the pathway are tested with the interferometric cantilever. The samples were prepared by two different approaches: a batch reactor and a continuous flow reactor. In each case, the same enzymatic nanoparticles were used as described in Section 4.5.2. Briefly, solutions of the enzyme module (HLPT) and chitosan magnetic nanoparticles (CM) were obtained from Dr. Rohan Fernandes. The solutions were mixed and diluted with 10 mM phosphate buffer (pH 6) to obtain a final concentration of 0.053 mg/mL and 1 mg/mL for HLPT and CM respectively. The resulting mixture was incubated at room temperature for 1 hr and used to synthesize AI-2 in each of the two reactors described below.

5.7.1 Batch Reactor Samples

The first enzymatic reactor was of the batch type, and it was prepared as follows. A 1.5 mL test tube was filled with the HLPT-CM mixture, and the nanoparticles were precipitated with a permanent magnet. The supernatant was removed and discarded. Then, 500 μ L of 1 mM SAH solution in phosphate buffer was added to the same tube, and the nanoparticles were stirred in order to dissolve again. After allowing the solution to react for 1 hr at room temperature, the particles were precipitated with a magnet. The supernatant was extracted and used as a sample for the cantilever sensor. Another batch reactor tube was prepared in the same manner, but it was immersed in a 95°C water bath before introducing the SAH solution in order to denature the enzymes. The reacted SAH sample from this tube was also used as a sample for the cantilever sensor.

5.7.2 Flow Reactor Samples

The second enzymatic reactor was of the continuous flow type, and it consisted of a piece of Tygon fluidic tubing (ID 380 μ m) with enzymatic nanoparticles adsorbed on the inner walls. The tubing was prepared by the same procedures described in Section 4.5.2. Briefly, the HLPT-CM mixture was injected, and a magnetic field was applied for 5 min; then, the mixture was flushed with clean buffer solution to remove unbound particles.

As discussed previously, the interferometric cantilever makes use of input wells that are filled with a pipette in order to facilitate injection of multiple samples. For this reason, the functionalized tubing cannot be connected directly to the input as in

the case of the waveguide cantilever. Instead, samples are collected from the output of the tubing in containers and then pipetted into the wells of the cantilever sensor.

To synthesize the samples, SAH solutions (1 mM concentration in phosphate buffer) were injected into the functionalized tubing with a syringe pump at a flow rate of 1 $\mu\text{L}/\text{min}$ or 10 $\mu\text{L}/\text{min}$. After samples were obtained with the functioning enzyme, the enzyme was purposely denatured. For this, a 5% w/v NaOH solution was flowed in the tubing for 5 min followed by rinsing with PB (phosphate buffer). Then, another 1mM SAH sample was processed with the denatured reactor at a flow rate of 1 $\mu\text{L}/\text{min}$, and the output was collected for testing with the cantilever sensor.

5.7.3 Detection Results

In addition to the 5 samples obtained with the two types of reactors, several control samples were prepared: 1 mM and 100 μM homocysteine solutions from powder and an unreacted 1 mM SAH solution. In all cases, the solvent was PB.

The 8 samples were introduced into the 8 input wells of an interferometric cantilever chip after taking initial (baseline) images in PB. The liquids were sucked into the parallel channels consecutively with a syringe connected to the output tubing. Then, each cantilever was imaged again 5 min and 10 min after the sample injection, and the displacement was extracted from the images. The results are shown in Figure 5.12. The values from the flow reactor are labeled with the respective flow rate, and those from the control samples are labeled with their content and concentration.

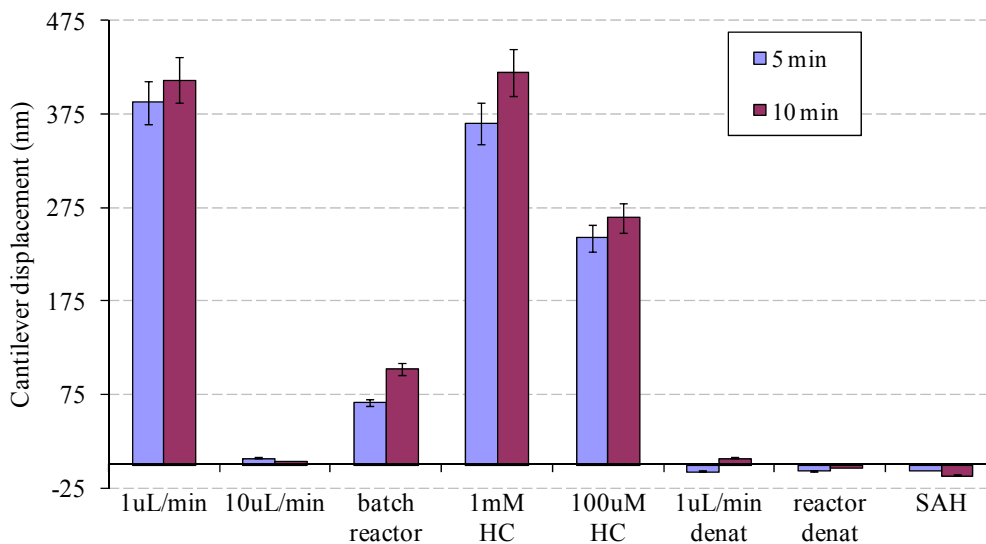


Figure 5.12: Interferometric cantilever displacement measured in response to different samples either 5 or 10 min after sample injection. Large displacement signifies high homocysteine concentration.

These results confirm that the enzymatically produced homocysteine is successfully detected. In the case of the flow reactor at 1 $\mu\text{L}/\text{min}$, the signal is close to that of the 1mM homocysteine control sample; this suggests that full enzymatic conversion occurred. The signal from the batch reactor is much lower, indicating incomplete conversion. This may be due to insufficient enzyme residence time in this case. The same explanation can be applied to the 10 $\mu\text{L}/\text{min}$ flow reactor, where the conversion is even lower (essentially 0). The samples from the denatured reactors, both batch and flow at 1 $\mu\text{L}/\text{min}$, do not elicit any significant response. The slight negative displacement in these cases can be attributed to thermal drift of the cantilever or nonspecific interaction with the sample. The slight response to unreacted SAH is presumably due to the same causes.

Figure 5.12 essentially shows that the sensor can distinguish between active and inactive enzymes. The inhibition of the bacterial enzymes with drugs would have the same effect as denaturation: stopping the production of homocysteine. Therefore, the

cantilever sensor can be used for screening candidate drugs aimed at suppressing bacterial quorum sensing.

5.8 Discussion

Table 5.3 compares the results from the homocysteine detection experiments described in this chapter. Each row lists the figure in which the result was presented, the maximum measured displacement of the cantilever, and the surface stress calculated from the mechanical sensitivity (Equation 2.1). The stress values are consistent with each other and with the results from the waveguide cantilever presented in Table 4.1. As discussed previously, some variation between devices is normal since the density of thiol monolayers greatly depends on gold surface properties [140]. Note that the variation in stress here is smaller than in the case of the waveguide cantilever. This may be due to the fact that the waveguide devices also have another source of variability: the conversion of optical power into displacement (i.e. the optical sensitivity). In comparison, the interferometric measurements are more repeatable from device to device since they do not depend on the optical sensitivity.

Table 5.3: Summary of results from homocysteine detection experiments performed with interferometric cantilever.

Figure	HC conc. (mM)	Length (μm)	Displacement (nm)	Surface stress (N/m)
5.8	1	110	371	0.13
5.9	1	110	450	0.15
5.10	1	110	380	0.13
5.11	1	110	356	0.12
5.12 (from powder)	1	110	419	0.14
5.12 (enzymatic)	< 1	110	411	0.14

The detection results from both the homocysteine and pH experiments demonstrate the ability of the interferometric readout method to measure multiple

cantilevers in parallel. For example, if the experiment in Figure 5.10 was performed with the conventional PSD method (Section 1.3.4.2), the reader would have to capture the entire response of one cantilever (~1 hour) before moving to another due to the tight alignment tolerances. Therefore, the total experimental time would be 5 hours. Using our interferometric method, the responses of all 5 cantilevers are captured in one hour because the alignment is not critical and the reader can be moved between devices that are simultaneously exposed to samples. Clearly, the ability for parallel measurements would be even more beneficial for larger numbers of cantilevers or longer sample exposure times. The results in Figure 5.7 demonstrate that relatively large numbers of devices can be measured if their displacement does not need to be tracked continuously.

The main limitation of the interferometric method is its limited temporal resolution due to the slow acquisition of digital images. It is only eligible for static mode detection. In addition, it is better suited for measuring the final cantilever displacement rather than the evolution of displacement over time. However, the results in Figure 5.12 show that only one displacement value is sufficient for detection. The continuous tracking of displacement in the rest of the experiments (Figure 5.8 through Figure 5.11) was performed here for characterization purposes but would not be needed in a drug screening application.

5.9 Summary

This chapter described the testing procedures and results for the interferometric cantilever sensor. The experimental setup and methodology were presented first, followed by a characterization of the effect of the microscope light source on the

interference pattern contrast. The random measurement error was found to be on the order of ± 1 nm, leading to a minimal detectable displacement of 1 nm and corresponding minimal surface stress of 340 $\mu\text{N/m}$ for a 110 μm long cantilever. The systematic measurement error with the image analysis procedure in use is less than 6% of displacement; it can be reduced further by a more detailed analysis at the expense of increased measurement time. The capability of the interferometric method to measure multiple devices in parallel was demonstrated by detecting both samples with varying pH and homocysteine samples. The homocysteine was obtained by dissolving commercially available powder or synthesized by the quorum sensing enzymes. The minimal detected homocysteine concentration was 1 μM . In addition, enzyme denaturation events were successfully observed due to the reduced sensor response.

Chapter 6: Conclusion

6.1 Summary

This dissertation has presented the design, fabrication, and testing of two types of microcantilever sensors for monitoring bacterial quorum sensing. Bacterial infections are a major healthcare problem, and the resistance of bacteria to conventional antibiotics is increasing. For this reason, new approaches to drug discovery are badly needed. One such approach is the inhibition of bacterial communications (also called quorum sensing) in order to suppress the formation of biofilms and reduce their pathogenicity. The sensors developed in this dissertation indirectly monitor the activity of the bacterial enzymes that synthesize signaling molecules. This is accomplished by detecting the compound homocysteine, which is a byproduct in the enzymatic pathway. Since the sensors are based on MEMS technology, they use small sample volumes and can be fabricated with large density at low cost. Therefore, these devices are a significant step toward high-throughput screening of candidate drugs that inhibit bacterial quorum sensing.

The main advantages of the microcantilever over competing sensor technologies are its small footprint and its label-free principle of operation. However its readout, i.e. the measurement of beam displacement, remains challenging. The traditional readout methods involve elaborate free-space optics, and can normally acquire the response of only one device at a time due to the strict alignment tolerances. This limitation prevents the use of cantilever sensors in array format for high-throughput screening. The two types of cantilevers developed in this dissertation employ new

readout schemes that overcome the deficiencies of the traditional displacement measurement methods.

6.1.1 Waveguide Cantilever

This device operates on the principle of variable optical coupling. The cantilever is a section of an on-chip waveguide that is released from the substrate. It couples light to an output waveguide across a short gap. As the cantilever moves up or down, the power of light measured at the output is varied, and it serves as an indication of beam displacement. This design considerably simplifies the off-chip measurement setup. Although several demonstrations of the waveguide cantilever approach were previously reported in literature, none of them were performed in liquid. The device in this work was embedded in a microfluidic channel and used for detecting liquid samples of homocysteine from the bacterial quorum sensing pathway. Since the majority of chemical and biological samples occur in solution state, the capability of the sensor to operate in liquid is a significant benefit. Also, the customized fabrication process developed here allowed us to control beam curvature and improve the sensitivity of the presented device over previous demonstrations. The curvature control was achieved through stress engineering of the SU-8 material.

6.1.2 Interferometric Cantilever

The second type of cantilever forms an interference pattern when imaged with an optical microscope with sufficiently narrow illumination spectral width. This pattern is the result of mixing light beams reflected off the cantilever and off the substrate underneath. As the cantilever moves up or down, the interference fringes move laterally; accordingly, the vertical displacement is calculated from the cantilever slope

and the lateral fringe shift. Although this measurement method uses external instrumentation, the microscope is a standard laboratory tool and the experimental setup is relatively simple. The alignment of the chip to the microscope is not critical, and it was shown that multiple cantilever experiments can be tracked in parallel by translating the stage. To speed up the measurements, an automated software algorithm was developed for analyzing the cantilever images and extracting the lateral fringe shift.

The fabrication process of the interferometric device is very similar to that of the waveguide cantilever, and the same curvature control strategies were used to obtain a favorable beam slope. The device was also embedded in a microfluidics channel and used for detecting multiple liquid homocysteine samples from the bacterial synthetic pathway simultaneously. Importantly, the interferometric readout method presented here is a new invention that has not been previously reported in literature.

6.1.3 Comparison of Devices

The two types of microcantilever sensors developed in this dissertation are complementary to one another, and each of them has unique advantages. The waveguide cantilever allows for faster displacement measurements than the interferometric device and enables continuous data acquisition. This capability may be needed in applications where the transient displacement must be captured rather than the final value. The waveguide cantilever also requires less external instrumentation and can be adapted for portable operation. Although a benchtop laser and photodetector were used to test the device here, these components can be miniaturized and integrated with the chip as discussed in Section 6.2. Portability is

not required for the screening of bacterial quorum sensing inhibitors, but it may be needed for some of the other applications envisioned in Section 6.2.3.

The interferometric readout is inherently a benchtop method. It is not eligible for portable use due to the requirement of a microscope. Also, the interferometric measurements are relatively slow due to the limited imaging speed. Therefore, this method is better suited to situations where a single cantilever displacement value is needed rather than the transient response. There are many such applications, including the screening of bacterial quorum sensing inhibitors. The main advantage of the interferometric approach is that it is capable of multiple measurements in parallel. Each cantilever is interrogated by simply imaging it, and there is no need to interface the chip with lasers or photodetectors. Since no waveguides are required, the cantilever density can be made much higher than in the case of the waveguide-based approach. In addition, the interferometric device is more accurate and sensitive. It has a minimal detectable displacement of 1 nm compared to 6 nm for the waveguide cantilever. Finally, the interferometric device has better long-term stability since it is immune to light intensity fluctuations.

6.2 Future Work

6.2.1 Microfluidic System

As explained in Chapter 1, the cantilever sensors presented in this dissertation are part of a larger project at the University of Maryland aimed at studying bacterial quorum sensing. Other members of the project team are focused on developing optimized microfluidic devices which perform the enzymatic conversion in a more controlled manner [46, 47]. In that work, the bacterial enzymes are immobilized on

chitosan-coated electrodes with well-defined area, and the dead volume in the channel is minimized. These optimized microfluidic reactors can be combined with the sensors developed in this dissertation in order to perform synthesis and analysis on the same chip. The cantilevers presented here were already embedded in microfluidic channels; therefore, it would only be necessary to change the geometry of the channels and add gold electrodes for chitosan electro-deposition. Furthermore, the microfluidic design can be readily enhanced to include on-chip valves and pumps [113, 114]. This would allow for a large degree of automation of liquid handling and would facilitate the high-throughput screening of quorum sensing inhibitors.

6.2.2 Applications beyond Quorum Sensing

Although the devices in this dissertation are developed for detecting the output of bacterial quorum sensing enzymes, they can be used for other purposes. It has already been shown that cantilevers in the static mode are excellent tools for many biochemical applications. For example, they can detect DNA hybridization [81, 82, 92-94], binding of antigens to antibodies [30, 95-97], and binding of substrates to enzymes [98, 99]. The only modification required for these studies is to coat the cantilever with a particular selective layer of probe biomolecules. The displacements observed in these experiments (10s of nm) are well above the detection limit of the methods presented here (6 nm or 1 nm) and occur over relatively slow timescales (10s of min). The cantilever position is usually measured continuously, but the initial and final displacement values are sufficient to indicate a binding event. Therefore, both the waveguide and interferometric cantilevers can be used to perform a variety of biochemical detection experiments.

6.2.3 Integration of Optoelectronics

The waveguide cantilever sensor developed in this dissertation is a passive device, i.e. it uses an external light sources and a photodetector. These components can be implemented at the chip level in order to eliminate the need for an external optical setup and test multiple sensors in parallel. A technology for bonding lasers or photodiodes to silicon substrates (known as hybrid integration) has been developed previously for optical communications applications [146, 147]. The same approach can be used here to couple light to and from the on-chip waveguides permanently without the need for XYZ stages. This would also decrease the power drift and improve the minimal detectable displacement.

A possible hybrid integration scheme is shown in Figure 6.1. Here, the output is detected by a p-n photodiode formed directly on the Si substrate by doping. As the light reaches the end of the output waveguide, it diverges, and part of it is captured by the photodiode. Since light generation is incompatible with the Si material system, a laser diode chip can be purchased separately and bonded to the substrate near the input waveguide facet. Unpackaged laser chips are commercially available at a relatively low cost (~\$0.30 each)⁶. Their typical size is approximately $300\ \mu\text{m} \times 300\ \mu\text{m}$, and their thickness is $100\ \mu\text{m}$. The emitting aperture is approximately $1\ \mu\text{m}$ high by $3\ \mu\text{m}$ wide. Therefore, light can be efficiently coupled into the on-chip waveguide, whose cross sectional dimensions are much larger ($2.2\ \mu\text{m}$ by $20\ \mu\text{m}$). The laser die

⁶ One of the companies that sells unpackaged laser dies is Roithner Lasertechnik (www.roithner-laser.com)

can be placed with a precision positioning arm and soldered as described by Hashimoto *et al.* [146].

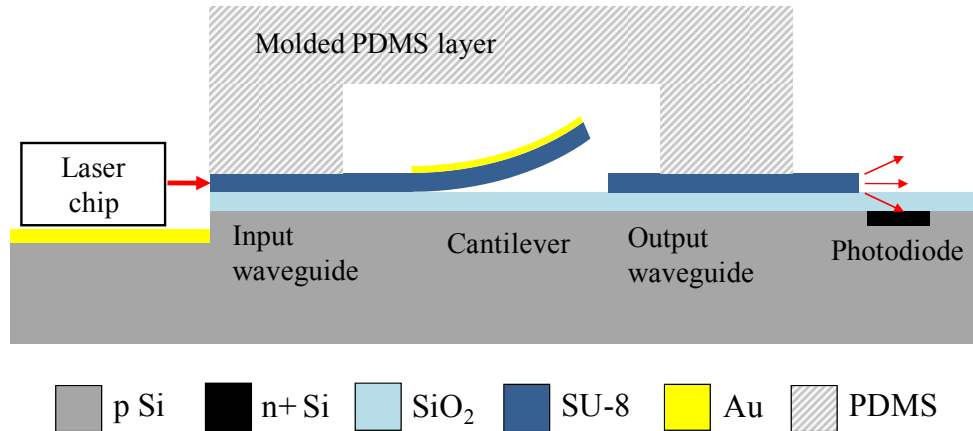


Figure 6.1: Possible scheme for integration of optical source and detector with the waveguide cantilever sensor at the chip level.

The optoelectronic components can also be added at the package level instead of the chip level. This concept is illustrated in Figure 6.2. Here, a reusable handheld package contains laser diodes and photodiodes; the waveguide cantilever chip is placed into the package and aligned to achieve sufficient optical coupling. A precision alignment mechanism will likely be required for this purpose. The coupling is particularly sensitive to misalignment at the input due to the small cross-section of the waveguides. Note that splitters can be built into the input waveguides, allowing a single laser to be shared between multiple cantilevers. After the chip is used for detection, it is discarded, and a fresh chip is inserted into the same package. This type of chips can have much lower cost than the proposed hybrid-integrated devices (Figure 6.1) since they are passive.

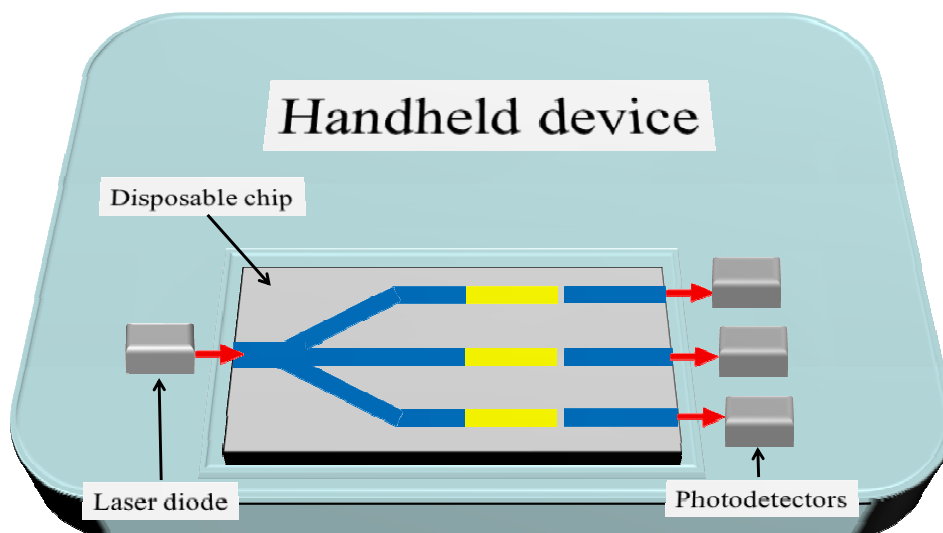


Figure 6.2: Possible scheme for providing optical sources and detectors for the waveguide cantilever sensor at the package level.

6.2.4 Interferometric Cantilever Arrays

The interferometric cantilever does not require any optoelectronic components at either the chip level or package level; therefore, it can be scaled to large arrays. When discussing the potential for sensor arrays, it is instructive to consider the fluorescent DNA microarray [148], which is the workhorse of modern molecular biology. This device is based on a simple, disposable chip with thousands of sites and an external scanner that sequentially images all the sites. One scan is sufficient to detect the binding events at each site. Hence, the scan time is not critical and the array can be made very large, leading to massively parallel experiments. The interferometric readout method developed here can be used to measure cantilever arrays in a similar manner. Although the fluorescent microarray is an extremely successful technology, it has one major flaw: the target molecules must be fluorescently labeled. This complicates sample preparation. Moreover, in the case of protein microarrays, the label can modify the properties of the target protein and reduce detection specificity

[66]. Cantilever arrays would overcome that problem since they do not require labeling.

Figure 6.3 illustrates the potential transition from fluorescent arrays to interferometric cantilever arrays. Each site in (a) and each cantilever in (b) are functionalized with particular probe biomolecules. The sample detection in (a) is performed by measuring the fluorescent image intensity at each site. In (b), the sample detection would be performed by measuring the fringe shift for each cantilever. Clearly, the image analysis in (b) would be more challenging, but the sample in that case does not need to be fluorescently labeled. The added complexity in interferometric image analysis would likely be insignificant, considering the capabilities of modern digital image processing techniques.

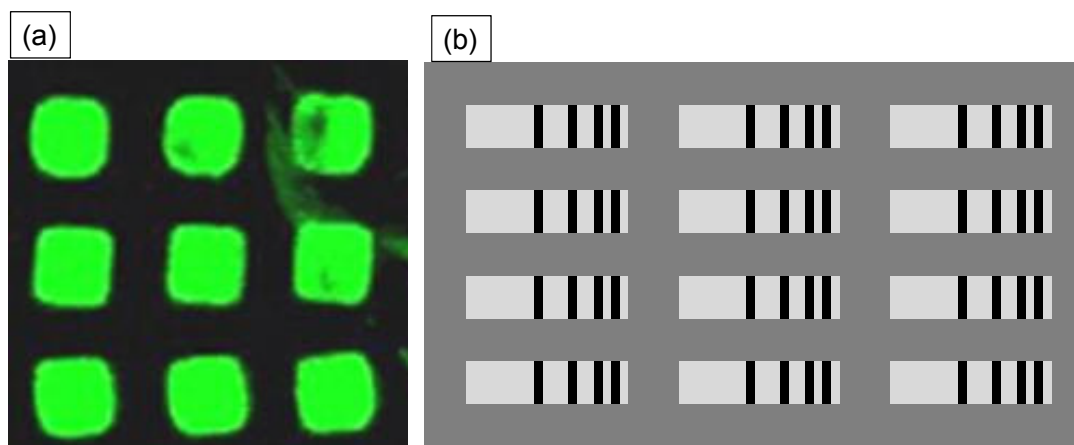


Figure 6.3: a) Fluorescent micrograph of a conventional protein microarray (source: www.arrayit.com). b) Hypothetical bright-field micrograph of a future interferometric cantilever array.

The maximum number of interferometric cantilevers scanned in this dissertation was 30 (Figure 5.7) and the total scan time (including image processing) was 20 min. Although this is a modest demonstration, there is considerable room for

improvement. The image acquisition can be made much faster by using a microscope with a motorized stage and automatic focus adjustment. It can also be accelerated by placing the cantilevers close to each other on the chip so that multiple devices fit in the same image. Moreover, the need for taking initial images of each device would be eliminated if the cantilevers are made more similar to each other by improved fabrication process control. Finally, the image processing algorithm can also be automated further to reduce the amount of user input required.

6.2.5 Sensitivity Enhancement

As discussed previously in Section 6.2.2, both the interferometric cantilever and the waveguide cantilever demonstrated here have sufficient sensitivity for a variety of biochemical detection applications. However, if necessary, their sensitivity can be improved even further through several modifications of the design and experimental setup.

6.2.5.1 Waveguide Cantilever

Reducing the thickness of the waveguide cantilever can improve both its mechanical and optical sensitivity. This can be achieved though exploring other formulations of SU-8 with higher solvent content. The reduced thickness will likely require decreasing the gap between the cantilever and output waveguide. The reason for this is that the divergence in the gap will become more significant as the mode waist is reduced.

The minimal detectable cantilever displacement can be lowered by improving the stability of input light power. The hybrid integration of a laser diode proposed in Section 6.2.3 should significantly reduce the power drift. Another method for

stabilizing the power could be the use of a reference waveguide without a cantilever adjacent to the waveguide being tested. Part of the input power can be diverted to this reference waveguide through a coupler and collected at its output with a second photodetector. The output from the cantilever can be divided by the output from the reference to account for any fluctuations in input power.

6.2.5.2 Interferometric Cantilever

The interferometric cantilever would also benefit from a reduction in thickness due the increase of its mechanical sensitivity. Although this would not affect the minimal detectable displacement appreciably, it would reduce the minimal detectable surface stress. Further gains can be accomplished by improving the instrumentation and image analysis procedures. More uniform microscope illumination and automatic focus adjustment would reduce the variability due to sample repositioning and refocusing. Higher optical magnification and higher resolution cameras would reduce the quantization error. Alternatively, more advanced image processing algorithms can be employed to detect sub-pixel fringe shifts [149]. The use of compensated microscope objectives would reduce aberration effects caused by packaging materials and improve the image quality.

6.3 Conclusion

This dissertation is the first demonstration of MEMS sensors used for the study of bacterial quorum sensing. The devices described here will serve as building blocks in future systems for high-throughput screening of drugs that inhibit quorum sensing. This could accelerate the discovery of new antimicrobials. In addition, the two displacement measurement methods developed here are significant contributions to

the field of cantilever sensors in general. They reduce the complexity of the measurement setups and enable parallel operation of multiple sensors. I hope that these improvements will be utilized for a variety of applications such as environmental monitoring, biohazard detection, and clinical diagnostics.

Appendix A: MATLAB Script for Fringe Shift Measurement

Section 2.3.2 describes in detail the principle of operation of the interferometric cantilever. Briefly, the displacement of the beam is found by multiplying the lateral shift of an interference fringe by the cantilever slope and a scaling factor (Equation 2.23). The algorithm for extracting the fringe shift from microscope images of the cantilever is described conceptually in Section 2.3.3. The MATLAB source code used to implement this algorithm is included below.

```
%-----  
% Filename: Fringe_shift.m  
% Author: Stephan Koev  
% Date of last revision: 12/1/2008  
% Description:  
% This program inputs two images of a cantilever interferometer. One image  
% is "before" a biological or chemical sample is introduced. The other  
% image is "after" the sample is introduced. First, the program aligns the  
% two images using features away from the interference pattern. Next, the  
% program finds the distance of an interference fringe in the "after" image  
% from the corresponding fringe in the "before" image. This fringe shift can  
% be used to calculate the cantilever displacement due to the sample. The  
% current image alignment algorithm can handle translation but not  
% rotation. In other words, the cantilever may be vertically or  
% horizontally moved relative to the camera between taking "before" and  
% "after" images; however, it must not be rotated.  
%-----  
  
close all  
clear all  
before = imread('before.jpg'); % read in initial image of cantilever  
after = imread('after.jpg'); % read in image of displaced cantilever  
  
% By cropping the images interactively, select features away from the  
% interference pattern to be used for alignment.  
[large_im, rect_large] = imcrop(before); % crop "before" interactively  
[small_im, rect_small] = imcrop(after); % crop "after" interactively  
% Note: during cropping, make sure that cropped "before" image is larger  
% than cropped "after" image. This is required by the cross-correlation  
% function later.  
close all  
% calculate cross-correlation of sub-images used for alignment  
c = normxcorr2(small_im(:, :, 1), large_im(:, :, 1));  
% find maximum of cross-correlation. This corresponds to optimal alignment.  
[max_c, imax] = max(abs(c(:)));  
% find the coordinates of the cross-correlation maximum.
```



```

[ypeak, xpeak] = ind2sub(size(c),imax(1));
% find the horizontal and vertical misalignment between the sub-images
corr_offset = [(xpeak-size(small_im,2))
               (ypeak-size(small_im,1))];
% find the misalignment between the uncropped "before" and "after" images,
% taking into account the cropping coordinates. This is the misalignment
% caused by movement of the cantilever relative to the camera.
rect_offset = [(rect_large(1)-rect_small(1))
               (rect_large(2)-rect_small(2))];
fov_offset = - corr_offset - rect_offset;
% print to screen the horizontal misalignment, vertical misalignment, and
% peak cross-correlation
fov_offset_x = fov_offset(1);
fov_offset_y = fov_offset(2);
max_c1 = max_c;
% By cropping the "before" and "after" images interactively, select an
% interference fringe whose shift needs to be found
% Note: during cropping, make sure that cropped "before" image is larger
% than cropped "after" image. This is required by the cross-correlation
% function later.
[large_im, rect_large] = imcrop(before); % select fringe on "before" image
imshow(large_im) % display fringe sub-image
figure, imshow(after)
[small_im, rect_small] = imcrop(after); % select fringe on "after" image
imshow(small_im) % display fringe sub-image
clear before after % discard uncropped images
% calculate cross-correlation of fringe sub-images
c = normxcorr2(small_im(:,:,1), large_im(:,:,1));
% find maximum of cross-correlation. This corresponds to optimal alignment.
[max_c, imax] = max(abs(c(:)));
% find the coordinates of the cross-correlation maximum
[ypeak, xpeak] = ind2sub(size(c),imax(1));
figure, surf(c), shading flat % plot the cross-correlation
% find the horizontal and vertical misalignment between the fringe sub-images
corr_offset = [(xpeak-size(small_im,2))
               (ypeak-size(small_im,1))];
% find the misalignemnt due to cropping
rect_offset = [(rect_large(1)-rect_small(1))
               (rect_large(2)-rect_small(2))];
% find the shift of the fringe, taking into account the misalignment due to
% cropping and the movement of the cantilever relative to the camera.
fringe_offset = -corr_offset - rect_offset + (-1*fov_offset);
% print to screen the horizontal fringe shift, the vertical fringe shift,
% and the peak cross-correlation

[xoffset yoffset fov_offset_x fov_offset_y max_c max_c1]'

```

References

- [1] K. C. Cheung and P. Renaud, "BioMEMS for medicine: On-chip cell characterization and implantable microelectrodes," *Solid-State Electronics*, vol. 50, pp. 551-557, 2006.
- [2] A. C. R. Grayson, R. S. Shawgo, A. M. Johnson, N. T. Flynn, Y. Li, M. J. Cima, and R. Langer, "A BioMEMS Review: MEMS Technology for Physiologically Integrated Devices," *Proceedings of the IEEE*, vol. 92, pp. 6-21, 2004.
- [3] S. Bhattacharya, J. Jang, L. Yang, D. Akin, and R. Bashir, "BioMEMS and Nanotechnology-Based Approaches for Rapid Detection of Biological Entities," *Journal of Rapid Methods & Automation in Microbiology 15 (2007) 1-32.*, vol. 15, pp. 1-32, 2007.
- [4] I. Giouroudi, J. Kosel, and C. Scheffer, "BioMEMS in Diagnostics: A Review and Recent Developments," *Recent Patents on Engineering*, vol. 2, pp. 114-121, 2008.
- [5] C. D. Chin, V. Linder, and S. K. Sia, "Lab-on-a-chip devices for global health: Past studies and future opportunities," *Lab Chip*, vol. 7, pp. 41-57, 2007.
- [6] S. Haeberle and R. Zengerle, "Microfluidic platforms for lab-on-a-chip applications," *Lab Chip*, vol. 7, pp. 1094-1110, 2007.
- [7] B. H. Weigl, R. L. Bardell, and C. R. Cabrera, "Lab-on-a-chip for drug development," *Advanced Drug Delivery Reviews*, vol. 55, pp. 349-377, 2003.
- [8] P.-A. Auroux, D. Iossifidis, D. R. Reyes, and A. Manz, "Micro total analysis systems. 2. Analytical standard operations and applications," *Anal. Chem.*, vol. 74, pp. 2637-2652, 2002.
- [9] D. R. Reyes, D. Iossifidis, P.-A. Auroux, and A. Manz., "Micro total analysis systems. 1. Introduction, theory, and technology," *Anal. Chem.*, vol. 74, pp. 2623-2636, 2002.
- [10] T. Vilckner, D. Janasek, and A. Manz, "Micro Total Analysis Systems. Recent Developments," *Anal. Chem.*, vol. 76, pp. 3373-3386, 2004.
- [11] P. S. Dittrich and A. Manz, "Lab-on-a-chip: microfluidics in drug discovery," *Nat. Rev. Drug Disc.*, vol. 5, pp. 210-218, 2006.
- [12] G. M. Whitesides, "The origins and the future of microfluidics," *Nature*, vol. 442, pp. 368-373, 2006.
- [13] J. Pihl, M. Karlsson, and D. T. Chiu, "Microfluidic technologies in drug discovery," *Drug Discovery Today*, vol. 10, pp. 1377-1383, 2005.
- [14] D. Hogan and R. Kolter, "Why are bacteria refractory to antimicrobials?" *Current Opinion in Microbiology*, vol. 5, pp. 472-477, 2002.
- [15] S. J. Projan and P. J. Youngman, "Antimicrobials: New solutions badly needed," *Current Opinion in Microbiology*, vol. 5, pp. 463-465, 2002.
- [16] J. A. DiMasi, R. W. Hansen, and H. G. Grabowski, "The price of innovation: new estimates of drug development costs," *Journal of Health Economics*, vol. 22, pp. 151-185, 2003.
- [17] M. B. Schmid, "Do targets limit antibiotic discovery?" *Nature Biotechnology*, vol. 24, pp. 419-420, 2006.

- [18] K. H. Bleicher, H.-J. Böhm, K. Müller, and A. I. Alanine, "Hit and Lead Generation: Beyond High-Throughput Screening," *Nature Reviews Drug Discovery*, vol. 2, pp. 369-378, 2003.
- [19] J. Drews, "Drug Discovery: A Historical Perspective," *Science*, vol. 287, pp. 1960-1964, 2000.
- [20] M. S. Lesney, "The Microfluidic Milieu," *Mod. Drug Disc.*, vol. 5, pp. 37-41, 2002.
- [21] J. C. March and W. E. Bentley, "Quorum Sensing and Bacterial Cross-talk in Biotechnology," *Curr. Opin. Biotechnol.*, vol. 15, pp. 495-502, 2004.
- [22] U. H. Strocher, A. W. Paton, A. D. Ogunniyi, and J. C. Paton, "Mutation of luxS of *Streptococcus pneumoniae* Affects Virulence in a Mouse Model," *Infection and Immunity*, vol. 71, pp. 3206-3212, 2003.
- [23] M. Hentzer and M. Givskov, "Pharmacological inhibition of quorum sensing for the treatment of chronic bacterial infections," *J Clin Invest*, vol. 112, pp. 1300-1307, 2003.
- [24] A. Vendeville, K. Winzer, K. Heurlier, C. M. Tang, and K. R. Hardie, "Making 'Sense' of Metabolism: Autoinducer-2, LuxS and Pathogenic Bacteria," *Nat. Rev. Microbiol.*, vol. 3, pp. 383-396, 2005.
- [25] A. F. Gonzalez-Barrios, R. Zuo, Y. Hashimoto, L. Yang, W. E. Bentley, and T. K. Wood, "Autoinducer 2 Controls Biofilm Formation in *Escherichia coli* through a Novel Motility Quorum-Sensing Regulator (MqsR, B3022)," *J Bacteriol*, vol. 188, pp. 305-316, 2006.
- [26] R. Fernandes, C. Y. Tsao, Y. Hashimoto, L. Wang, T. K. Wood, G. F. Payne, and W. E. Bentley, "Magnetic Nanofactories: Localized Synthesis and Delivery of Quorum-Sensing Signaling Molecule Autoinducer-2 to Bacterial Cell Surfaces," *Metab. Eng.*, vol. 9, pp. 228-239, 2007.
- [27] N. V. Lavrik, M. J. Sepniak, and P. G. Datskos, "Cantilever Transducers as a Platform for Chemical and Biological Sensors," *Rev. Sci. Instrum.*, vol. 75, pp. 2229-2253, 2004.
- [28] H. P. Lang, M. Hegner, E. Meyer, and C. Gerber, "Nanomechanics from atomic resolution to molecular recognition based on atomic force microscopy technology," *Nanotechnology*, vol. 13, pp. R29-R36, 2002.
- [29] L. G. Carrascosa, M. Moreno, M. Alvarez, and L. M. Lechuga, "Nanomechanical biosensors: a new sensing tool," *TrAC, Trends Anal. Chem.*, vol. 25, pp. 196-206, 2006.
- [30] R. Raiteri, M. Grattarola, H.-J. Butt, and P. Skladal, "Micromechanical cantilever-based biosensors," *Sens. Actuators, B*, vol. 79, pp. 115-126, 2001.
- [31] M. W. Pruessner, N. Siwak, K. Amarnath, S. Kanakaraju, W.-H. Chuang, and R. Ghodssi, "End-coupled Optical Waveguide MEMS Devices in the Indium Phosphide Material System," *J. Micromech. Microeng.*, vol. 16, pp. 832-842, 2006.
- [32] K. Zinoviev, C. Dominguez, J. A. Plaza, V. J. C. Busto, and L. M. Lechuga, "A Novel Optical Waveguide Microcantilever Sensor for the Detection of Nanomechanical Forces," *J. Lightwave Technol.*, vol. 24, pp. 2132-2138, 2006.

- [33] M. Nordström, D. A. Zauner, M. Calleja, J. Hübner, and A. Boisen, "Integrated Optical Readout for Miniaturization of Cantilever-based Sensor System," *Appl. Phys. Lett.*, vol. 91, pp. 103512, 2007.
- [34] J. W. Costerton, "A short history of the development of the biofilm concept," in *Microbial Biofilms*, M. Ghannoum and G. A. O'Toole, Eds. Washington, DC: ASM Press, 2004, pp. 4-19.
- [35] D. J. Musk, Jr. and P. J. Hergenrother, "Chemical countermeasures for the control of bacterial biofilms: Effective compounds and promising targets.," *Curr. Med. Chem.*, vol. 13, pp. 2163-2177, 2006.
- [36] P. S. Stewart, P. K. Mukherjee, and M. A. Ghannoum, "Biofilm Antimicrobial Resistance," in *Microbial Biofilms*, M. Ghannoum and G. A. O'Toole, Eds. Washington, DC: ASM Press, 2004, pp. 250-268.
- [37] K. B. Xavier and B. L. Bassler, "LuxS quorum sensing: more than just a numbers game," *Curr Opin Microbiol*, vol. 6, pp. 191-197, 2003.
- [38] D. Davies, "Understanding biofilm resistance to antimicrobial agents," *Nat. Rev. Drug Discov.*, vol. 2, pp. 114-122, 2003.
- [39] R. M. Donlan, "Biofilms and device-associated infections.," *Emerging Infect. Dis.*, vol. 7, pp. 277-281, 2001.
- [40] W. G. Characklis, "Microbial fouling," in *Biofilms*, W. G. C. a. K. C. Marshall., Ed. New York: John Wiley & Sons, Inc., 1990, pp. 523-584.
- [41] T. B. Rasmussen and M. Givskov, "Quorum-sensing inhibitors as anti-pathogenic drugs," *International Journal of Medical Microbiology*, vol. 296, pp. 149-161, 2006.
- [42] M. J. Federle and B. L. Bassler, " Interspecies communication in bacteria," *Journal of Clinical Investigation*, vol. 112, pp. 1291-1299, 2003.
- [43] A. T. Lewandowski, "Assembly of Quorum Sensing Pathway Enzymes onto Patterned Microfabricated Devices," Ph.D. Dissertation, University of Maryland, College Park, MD, USA, 2007.
- [44] A. T. Lewandowski, H. Yi, G. F. Payne, R. Ghodssi, G. W. Rubloff, and W. E. Bentley, "Towards Area-Based In Vitro Metabolic Engineering: Assembly of Pfs Enzyme onto Patterned Microfabricated Chips," *Biotechnol. Prog.* 2008, 24, vol. 24, pp. 1042-1051, 2008.
- [45] R. Fernandes and W. E. Bentley, "AI-2 Biosynthesis Module in a Magnetic Nanofactory Alters Bacterial Response via Localized Synthesis and Delivery," *Biotechnol. Bioeng.*, vol. 102, pp. 390-399, 2009.
- [46] X. Luo, D. L. Berlin, S. Buckhout-White, W. Bentley, G. Payne, R. Ghodssi, and G. Rubloff, "Design optimization for bioMEMS studies of enzyme-controlled metabolic pathways," *Biomed Microdevices*, vol. 10, pp. 899-908, 2008.
- [47] X. Luo, A. T. Lewandowski, H. Yi, G. F. Payne, R. Ghodssi, W. E. Bentley, and G. W. Rubloff, "Programmable assembly of a metabolic pathway enzyme in a pre-packaged reusable bioMEMS device," *Lab Chip*, vol. 8, pp. 420-430, 2008.
- [48] G. D. Ehrlich, F. Z. Hu, Q. Lin, J. W. Costerton, and J. C. Post, "Intelligent Implants to Battle Biofilms," *ASM News*, vol. 70, 2004.

- [49] G. D. Ehrlich, P. Stoodley, S. Kathju, Y. Zhao, B. R. McLeod, N. Balaban, F. Z. Hu, N. G. Sotereanos, J. W. Costerton, P. S. Stewart, J. C. Post, and Q. Lin, "Engineering Approaches for the Detection and Control of Orthopaedic Biofilm Infections," *Clin Orthop Relat Res.*, vol. 437, pp. 59-66, 2005.
- [50] Y. Kikutani, T. Horiuchi, K. Uchiyama, H. Hisamoto, M. Tokeshi, and T. Kitamori, "Glass microchip with three-dimensional microchannel network for 2 X 2 parallel synthesis," *Lab on a Chip*, vol. 2, pp. 188-192, 2002.
- [51] E. Garcia-Egido, V. Spikmans, S. Y. F. Wong, and B. H. Warrington, "Synthesis and analysis of combinatorial libraries performed in an automated micro reactor system," *Lab on a Chip*, vol. 3, pp. 73-76, 2003.
- [52] J. Pihl, J. Sinclair, E. Sahlin, M. Karlsson, F. Petterson, J. Olofsson, and O. Orwar, "Microfluidic Gradient-Generating Device for Pharmacological Profiling," *Anal. Chem.*, vol. 77, pp. 3897-3903, 2005.
- [53] P. S. Dittrich and P. Schuille, "An Integrated Microfluidic System for Reaction, High-Sensitivity Detection, and Sorting of Fluorescent Cells and Particles," *Anal. Chem.*, vol. 75, pp. 5767-5774, 2003.
- [54] S. B. Cheng, C. D. Skinner, J. Taylor, S. Attiya, W. E. Lee, G. Picelli, and D. J. Harrison, "Development of a Multichannel Microfluidic Analysis System Employing Affinity Capillary Electrophoresis for Immunoassay," *Anal. Chem.*, vol. 73, pp. 1472-1479, 2001.
- [55] Y. Rondelez, G. Tresset, K. V. Tabata, H. Arata, H. Fujita, S. Takeuchi, and H. Noji, "Microfabricated arrays of femtoliter chambers allow single molecule enzymology," *Nature Biotechnology*, vol. 23, pp. 361-365, 2005.
- [56] M. R. Chatni, "The onset of a revolution in drug discovery," *Trends in Biotechnology*, vol. 25, pp. 142-144, 2007.
- [57] J. M. Cooper and A. E. G. Cass, "Miniaturized screening technologies for drug discovery," *Biochemical Society Transactions*, vol. 30, pp. 802-806, 2002.
- [58] D. G. Myszka and R. L. Rich, "Implementing surface plasmon resonance biosensors in drug discovery," *Pharmaceutical Science & Technology Today*, vol. 3, pp. 310-317, 2000.
- [59] M. Keusgen, "Biosensors: new approaches in drug discovery," *Naturwissenschaften*, vol. 89, pp. 433-444, 2002.
- [60] E. Verpoorte, "Chip vision – optics for microchips," *Lab on a Chip*, vol. 3, pp. 42N-52N, 2003.
- [61] M. Dandin, P. Abshire, and E. Smela, "Optical filtering technologies for integrated fluorescence sensors," *Lab Chip*, vol. 7, pp. 955-977, 2007.
- [62] J. Hubner, K. B. Morgensen, A. M. Jorgensen, P. Friis, P. Tellman, and J. P. Kutter, "Integrated optical measurement system for fluorescence spectroscopy in microfluidic channels," *Review of Scientific Instruments*, vol. 72, 2001.
- [63] S. Balslev, B. Bilenberg, O. Geschke, A. M. Jorgensen, A. Kristensen, J. P. Kutter, K. B. Mogensen, and D. Snakenborg, "Fully Integrated Optical System for Lab-on-a-Chip Applications," *Proceeding of the 17th IEEE International Conference on Micro Electro Mechanical Systems*, pp. 89-92, Maastricht, The Netherlands, 2004.

- [64] M. A. Powers, S. T. Koev, A. Schleunitz, H. Yi, V. Hodzic, W. E. Bentley, G. F. Payne, G. W. Rubloff, and R. Ghodssi, "A Fabrication Platform for Electrically Mediated Optically Active Biofunctionalized Sites in BioMEMS," *Lab on a Chip*, vol. 5, pp. 583-586, 2005.
- [65] L.-Q. Li and L. M. Davis, "Single photon avalanche diode for single molecule detection," *Review of Scientific Instruments*, vol. 64, pp. 1524-1529, 1993.
- [66] P. Mitchell, "A perspective on protein microarrays," *Nature Biotechnology*, vol. 20, pp. 225-229, 2002.
- [67] R. Wang, M. Minunni, S. Tombelli, and M. Mascini, "A new approach for the detection of DNA sequences in amplified nucleic acids by a surface plasmon resonance biosensor," *Biosensors and Bioelectronics*, vol. 20, pp. 598-605, 2004.
- [68] S. Y. Wu, H. P. Ho, W. C. Law, and C. Lin, "Highly sensitive differential phase-sensitive surface plasmon resonance biosensor based on the Mach-Zehnder configuration," *Optics Letters*, vol. 29, 2004.
- [69] K. Kerman, M. Kobayashi, and E. Tamiya, "Recent trends in electrochemical DNA biosensor technology," *Measurement Science and Technology*, vol. 15, pp. R1-R11, 2004.
- [70] E. Komarova, M. Aldissi, and A. Bogomolova, "Direct electrochemical sensor for fast reagent-free DNA detection," *Biosensors and Bioelectronics*, vol. 21, pp. 182-189, 2005.
- [71] W. A. Wlassoff and G. C. King, "Ferrocene conjugates of dUTP for enzymatic redox labelling of DNA," *Nucleic Acids Research*, vol. 30, 2002.
- [72] M. Hedstrom, I. Y. Galaev, and B. Mattiasson, "Continuous measurements of a binding reaction using a capacitive biosensor," *Biosensors and Bioelectronics*, vol. 21, pp. 41-48, 2005.
- [73] M. J. Schoning, M. Arzdorf, P. Mulchandani, W. Chen, and A. Mulchandani, "A capacitive field-effect sensor for the direct determination of organophosphorus pesticides," *Sensors and Actuators B*, vol. 91, pp. 92-97, 2003.
- [74] E. A. Moschou and N. A. Chaniotakis, "Ion-Partitioning Bulk Membrane CHEMFET as Highly Sensitive Calcium Probe," *Electroanalysis*, vol. 15, 2003.
- [75] K. Lange, G. Blaess, A. Voigt, M. Rapp, E. Hansjosten, and U. Schygulla, "Packaging of Surface Acoustic Wave (SAW) based Biosensors: an Important Issue for Future Biomedical Applications," *IEEE International Ultrasonics, Ferroelectrics, and Frequency Control Joint 50th Anniversary Conference*, 2004.
- [76] G. Kim, W. Chong, S. Kim, K. Kim, S. Jeong, T. Kwon, N. Kim, and C. Hong, "Development of Biosensor Using Surface Acoustic Wave," *The 30th Annual Conference of the IEEE Industrial Electronics Society*, Busan, Korea, 2004.
- [77] F. Shen, K. H. Lee, S. J. O'Shea, P. Lu, and T. Y. Ng, "Frequency Interference Between Two Quartz Crystal Microbalances," *IEEE Sensors Journal*, vol. 3, 2003.

- [78] T. H. Ha, S. Kim, G. Lim, and K. Kim, "Influence of liquid medium and surface morphology on the response of QCM during immobilization and hybridization of short oligonucleotides," *Biosensors and Bioelectronics*, vol. 20, pp. 378-389, 2004.
- [79] Y. K. Hong, H. Park, S. Q. Lee, K. S. Moon, and M. Levy, "Fabrication of a piezoelectric biosensor based on a PZN-PT/PMN-PT single crystal thin film," *Proc. SPIE*, vol. 5602, pp. 140-147, 2004.
- [80] G. Wu, H. Ji, K. Hansen, T. Thundat, R. Datar, R. Cote, M. F. Hagan, A. K. Chakraborty, and A. Majumdar, "Origin of nanomechanical cantilever motion generated from biomolecular interactions," *PNAS*, vol. 98, 2001.
- [81] J. Fritz, M. K. Baller, H. P. Lang, H. Rothuizen, P. Vettiger, E. Meyer, H.-J. Guntherodt, C. Gerber, and J. K. Gimzewski, "Translating Biomolecular Recognition into Nanomechanics," *Science*, vol. 288, pp. 316-318, 2000.
- [82] M. Alvarez, L. G. Carrascosa, M. Moreno, A. Calle, A. Zaballos, L. M. Lechuga, C. Martinez-A, and J. Tamayo, "Nanomechanics of the Formation of DNA Self-Assembled Monolayers and Hybridization on Microcantilevers," *Langmuir*, vol. 20, pp. 9663-9668, 2004.
- [83] A. Gupta, D. Akin, and R. Bashir, "Single virus particle mass detection using microresonators with nanoscale thickness," *Applied Physics Letters*, vol. 84, 2004.
- [84] M. Su, S. Li, and V. P. Dravid, "Microcantilever resonance-based DNA detection with nanoparticle probes," *Applied Physics Letters*, vol. 82, 2003.
- [85] B. Illic, D. Czuplewski, H. G. Craighead, P. Neuzil, C. Campagnolo, and C. Batt, "Mechanical resonant immunospecific biological detector," *Applied Physics Letters*, vol. 77, 2000.
- [86] M. Calleja, J. Tamayo, A. Johansson, P. Rasmussen, L. Lechuga, and A. Boisen, "Polymeric Cantilever Arrays for Biosensing Applications," *Sens. Lett.*, vol. 1, pp. 1-5, 2003.
- [87] D. Strembeck, A. M. Robinson, F. E. Venneulen, M. Seto, and K. B. Brown, "Humidity Measurement Using Resonating CMOS Microcantilever Structures," *Proceedings of the 1999 IEEE Canadian Conference on Electrical and Computer Engineering*, Edmonton, Alberta, Canada, 1999.
- [88] N. Siwak, X. Z. Fan, D. Hines, E. Williams, N. Goldsman, and R. Ghodssi, "Chemical Sensor Utilizing Indium Phosphide Cantilevers and Pentacene as a Functionalization Layer," *Proceedings of the 20th IEEE International Conference on Micro Electro Mechanical Systems (MEMS 2007)*, pp. 489-492, Kobe, Japan, 2007.
- [89] T. Thundat, E. A. Wachter, S. L. Sharp, and R. J. Warmack, "Detection of mercury vapor using resonating microcantilevers," *Appl. Phys. Lett.*, vol. 66, 1995.
- [90] B. Rogers, L. Manning, M. Jones, T. Sulchek, K. Murray, B. Beneschott, J. D. Adams, Z. Hu, T. Thundat, H. Cavazos, and S. C. Minne, "Mercury vapor detection with a self-sensing, resonating piezoelectric cantilever," *Rev. Sci. Instrum.*, vol. 74, pp. 4899-4901, 2003.

- [91] T. H. Stievater, W. S. Rabinovich, M. S. Ferraro, N. A. Papanicolaou, R. Bass, J. B. Boos, J. L. Stepnowski, and R. A. McGill, "Photonic microharp chemical sensors," *Optics Express*, vol. 16, pp. 2423-2430, 2008.
- [92] X. R. Zhang and X. Xu, "Development of a biosensor based on laser-fabricated polymer microcantilevers," *Applied Physics Letters*, vol. 85, pp. 2423-2425, 2004.
- [93] R. McKendry, J. Zhang, Y. Arntz, T. Strunz, M. Hegner, H. P. Lang, M. K. Baller, U. Certa, E. Meyer, H.-J. Guntherodt, and C. Gerber, "Multiple label-free biodetection and quantitative DNA-binding assays on a nanomechanical cantilever array," *Proc. Nat. Acad. Sci. U.S.A.*, vol. 99, 2002.
- [94] S. T. Koev, M. A. Powers, H. Yi, L.-Q. Wu, W. E. Bentley, G. W. Rubloff, G. F. Payne, and R. Ghodssi, "Mechano-transduction of DNA hybridization and dopamine oxidation through electrodeposited chitosan network," *Lab on a Chip*, vol. 7, pp. 103-111, 2007.
- [95] G. Shekhawat, S.-H. Tark, and V. P. Dravid, "MOSFET-Embedded Microcantilevers for Measuring Deflection in Biomolecular Sensors," *Science*, vol. 311, pp. 1592-1595, 2006.
- [96] C. Grogan, R. Raiteri, G. M. O'Connor, T. J. Glynn, V. Cunningham, M. Kane, M. Charlton, and D. Leech, "Characterisation of an antibody coated microcantilever as a potential immuno-based biosensor," *Biosensors & Bioelectronics*, vol. 17, pp. 201-207, 2002.
- [97] Y. Arntz, J. D. Seelig, H. P. Lang, J. Zhang, P. Hunziker, J. P. Ramseyer, E. Meyer, M. Hegner, and C. Gerber, "Label-free protein assay based on a nanomechanical cantilever array," *Nanotechnology*, vol. 14, pp. 86-90, 2003.
- [98] A. Subramanian, P. I. Oden, S. J. Kennel, K. B. Jacobson, R. J. Warmack, T. Thundat, and M. J. Doktycz, "Glucose biosensing using an enzyme-coated microcantilever," *Appl. Phys. Lett.*, vol. 81, pp. 385-387, 2002.
- [99] X. Yan, H.-F. Ji, and Y. Lvov, "Modification of microcantilevers using layer-by-layer nanoassembly film for glucose measurement," *Chemical Physics Letters*, vol. 396, pp. 34-37, 2004.
- [100] T. Braun, V. Barwich, M. K. Ghatkesar, A. H. Bredekamp, C. Gerber, M. Hegner, and H. P. Lang, "Micromechanical mass sensors for biomolecular detection in a physiological environment," *Physical Review E*, vol. 72, 2005.
- [101] H. P. Lang, M. K. Baller, R. Berger, C. Gerber, J. K. Gimzewski, F. M. Battiston, P. Fornaro, J. P. Ramseyer, E. Meyer, and H. J. Guntherodt, "An artificial nose based on a micromechanical cantilever array," *Analytica Chimica Acta*, vol. 393, pp. 59-65, 1999.
- [102] H. P. Lang, R. Berger, F. Battiston, J.-P. Ramseyer, E. Meyer, C. Andreoli, J. Brugger, P. Vettiger, M. Despont, T. Mezzacasa, L. Scandella, H.-J. Güntherodt, C. Gerber, and J. K. Gimzewski, "A chemical sensor based on a micromechanical cantilever array for the identification of gases and vapors," *Appl. Phys A*, vol. 66, pp. S61-S64, 1998.
- [103] P. A. Rasmussen, J. Thaysen, O. Hansen, S. C. Eriksen, and A. Boisen, "Optimised cantilever biosensor with piezoresistive read-out," *Ultramicroscopy*, vol. 97, pp. 371-376, 2003.

- [104] A. Johansson, M. Calleja, P. A. Rasmussen, and A. Boisen, "SU-8 cantilever sensor system with integrated readout," *Sensors and Actuators A*, vol. 123-124, pp. 111-115, 2005.
- [105] Y. Lee, G. Lim, and W. Moon, "A self-excited micro cantilever biosensor actuated by PZT using the mass micro balancing technique," *Sensors and Actuators A*, vol. 130-131, pp. 105-110, 2006.
- [106] D. R. Baselt, B. Fruhberger, E. Klaassen, S. Cemalovic, C. L. Britton, S. V. Patel, T. E. Mlsna, D. McCorkle, and B. Warmack, "Design and performance of a microcantilever-based hydrogen sensor," *Sens. Actuators, B*, vol. 88, pp. 120-131, 2003.
- [107] J. Arcamone, G. Rius, G. Abadal, J. Teva, N. Barniol, and F. Perez-Murano, "Micro/nanomechanical resonators for distributed mass sensing with capacitive detection," *Microelectronic Engineering*, vol. 83, pp. 1216-1220, 2006.
- [108] M. Nordström, S. Keller, M. Lillemose, A. Johansson, S. Dohn, D. Haefliger, G. Blagoi, M. Havsteen-Jakobsen, and A. Boisen, "SU-8 Cantilevers for Bio/chemical Sensing; Fabrication, Characterisation and Development of Novel Read-out Methods," *Sensors*, vol. 8, pp. 1595-1612, 2008.
- [109] O. Svitelskiy, N. Liu, V. Sauer, K.-M. Cheng, E. Finley, M. Belov, M. R. Freeman, and W. K. Hiebert, "A simple cell for the analysis of nanoelectromechanical systems under gas pressure," *Rev Sci Instrum*, vol. 79, pp. 093701, 2008.
- [110] M. Helm, J. J. Servant, F. Saurenbach, and R. Berger, "Read-out of micromechanical cantilever sensors by phase shifting interferometry," *Appl. Phys. Lett.*, vol. 87, pp. 064101, 2005.
- [111] S. T. Koev and R. Ghodssi, "Advanced Interferometric Profile Measurements through Refractive Media," *Rev Sci Instrum*, vol. 79, pp. 093702, 2008.
- [112] S. Balslev, A. M. Jorgensen, B. Bilenberg, K. B. Mogensen, D. Snakenborg, O. Geschke, J. P. Kutter, and A. Kristensen, "Lab-on-a-chip with integrated optical transducers," *Lab on a Chip*, vol. 6, pp. 213-217, 2006.
- [113] M. A. Unger, H.-P. Chou, T. Thorsen, A. Scherer, and S. R. Quake, "Monolithic Microfabricated Valves and Pumps by Multilayer Soft Lithography," *Science*, vol. 288, pp. 113-116, 2000.
- [114] N. A. Cellar, S. T. Burns, J.-C. Meiners, H. Chen, and R. T. Kennedy, "Microfluidic Chip for Low-Flow Push-Pull Perfusion Sampling in Vivo with On-Line Analysis of Amino Acids," *Anal. Chem.*, vol. 77, pp. 7067-7073, 2005.
- [115] Y. Zhang, Q. Ren, and Y.-p. Zhao, "Modelling analysis of surface stress on a rectangular cantilever beam," *J. Phys. D: Appl. Phys.*, vol. 37, pp. 2140-2145, 2004.
- [116] S. A. Smee, M. Gaitan, D. B. Novotny, Y. Joshi, and D. L. Blackburn, "IC Test Structures for Multilayer Interconnect Stress Determination," *IEEE Electron Device Letters*, vol. 21, 2000.
- [117] J.-A. Schweitz and F. Ericson, "Evaluation of mechanical materials properties by means of surface micromachined structures," *Sens. Actuators, A*, vol. 74, pp. 126-133, 1999.

- [118] S. D. Senturia, *Microsystem Design*. Boston: Kluwer Academic Publishers, 2001.
- [119] J. E. Sader, "Surface stress induced deflections of cantilever plates with applications to the atomic force microscope: Rectangular plates," *Journal of Applied Physics*, vol. 89, 2001.
- [120] R. G. Hunsperger, *Integrated Optics*. Berlin: Springer-Verlag, 2002.
- [121] B. E. A. Saleh and M. C. Teich, *Fundamentals of Photonics*. New York: John Wiley & Sons, Inc., 1991.
- [122] V. Namasivayam, R. Lin, B. Johnson, S. Brahmaandra, Z. Razzacki, D. T. Burke, and M. A. Burns, "Advances in on-chip photodetection for applications in miniaturized genetic analysis systems," *J. Micromech. Microeng.*, vol. 14, pp. 81–90, 2004.
- [123] B. S. Gallardo, V. K. Gupta, F. D. Eagerton, L. I. Jong, V. S. Craig, R. R. Shah, and N. L. Abbott, "Electrochemical Principles for Active Control of Liquids on Submillimeter Scales," *Science*, vol. 283, pp. 57-60, 1999.
- [124] J. Alda, "Laser and Gaussian Beam Propagation and Transformation," in *Encyclopedia of Optical Engineering*. New York: Marcel Dekker, Inc., 2003.
- [125] C. G. Chen, P. T. Konkola, J. Ferrera, R. K. Heilmann, and M. L. Schattenburg, "Analyses of vector Gaussian beam propagation and the validity of paraxial and spherical approximations," *J. Opt. Soc. Am. A*, vol. 19, pp. 404-412, 2002.
- [126] L. G. Brown, "A Survey of Image Registration Techniques," *ACM Computing Surveys*, vol. 24, pp. 325-376, 1992.
- [127] N. Daldosso, M. Melchiorri, F. Riboli, F. Sbrana, L. Pavesi, G. Pucker, C. Kompocholis, M. Crivellari, P. Bellutti, and A. Lui, "Fabrication and optical characterization of thin two-dimensional Si₃N₄ waveguides," *Materials Science in Semiconductor Processing*, vol. 7, pp. 453–458, 2004.
- [128] W. Shi, H. Zhang, S. Wang, G. Zhang, and Z. Li, "Modifying Residual Stress and Stress Gradient in LPCVD Si₃N₄ Film with Ion Implantation," *The 13th International Conference on Solid-state Sensors, Actuators and Microsystems*, pp. 824-827, Seoul, Korea, 2005.
- [129] J. M. Olson, "Analysis of LPCVD process conditions for the deposition of low stress silicon nitride. Part I: preliminary LPCVD experiments," *Materials Science in Semiconductor Processing*, vol. 5, pp. 51-60, 2002.
- [130] V. E. Vamvakas, N. Vourdas, and S. Gardelis, "Optical characterization of Si-rich silicon nitride films prepared by low pressure chemical vapor deposition," *Microelectronics Reliability*, vol. 47, pp. 794-797, 2007.
- [131] D. Bachmann, B. Schoberle, S. Kuhne, Y. Leiner, and C. Hierold, "Fabrication and characterization of folded SU-8 suspensions for MEMS applications," *Sens. Actuators, A*, vol. 130-131, pp. 379-386, 2006.
- [132] R. Feng and R. J. Farris, "Influence of processing conditions on the thermal and mechanical properties of SU8 negative photoresist coatings," *J. Micromech. Microeng.*, vol. 13, pp. 80-88, 2003.
- [133] D. Sameoto, S.-H. Tsang, I. G. Foulds, S.-W. Lee, and M. Parameswaran, "Control of the out-of-plane curvature in SU-8 compliant microstructures by

- exposure dose and baking times," *J. Micromech. Microeng.*, vol. 17, pp. 1093–1098, 2007.
- [134] G. C. Hill, R. Melamud, F. E. Declercq, A. A. Davenport, I. H. Chan, P. G. Hartwell, and B. L. Pruitt, "SU-8 MEMS Fabry-Perot pressure sensor," *Sens. Actuators, A*, vol. 138, pp. 52-62, 2007.
- [135] J. C. McDonald and G. M. Whitesides, "Poly(dimethylsiloxane) as a Material for Fabricating Microfluidic Devices," *Accounts of Chemical Research*, vol. 35, pp. 491-499, 2002.
- [136] B. M. Foley, P. Melman, and K. T. Vo, "Novel Loss Measurement Technique for Optical Waveguides by Imaging of Scattered Light," *Electron. Lett.*, vol. 28, pp. 584-585, 1992.
- [137] R. Berger, E. Delamarche, H. P. Lang, C. Gerber, J. K. Gimzewski, E. Meyer, and H.-J. Güntherodt, "Surface Stress in the Self-assembly of Alkanethiols on Gold Probed by a Force Microscopy Technique," *Appl. Phys. A*, vol. 66, pp. S55-S59, 1998.
- [138] C. A. Canaria, J. So, J. R. Maloney, C. J. Yu, J. O. Smith, M. L. Roukes, S. E. Fraser, and R. Lansford, "Formation and removal of alkylthiolate self-assembled monolayers on gold in aqueous solutions," *Lab on a Chip*, vol. 6, pp. 289-295, 2006.
- [139] R. F. DeBono, G. D. Loucks, D. D. Manna, and U. J. Krull, "Self-assembly of short and long-chain n-alkyl thiols onto gold surfaces: A real-time study using surface plasmon resonance techniques," *Can. J. Chem.*, vol. 74, pp. 677-688, 1996.
- [140] F. Schreiber, "Self-assembled monolayers: from 'simple' model systems to biofunctionalized interfaces," *J. Phys.: Condens. Matter*, vol. 16, pp. R881-R900, 2004.
- [141] P. Goldberg, P. W. Milonni, and B. Sundaram, "Theory of the fundamental laser linewidth," *Phys. Rev. A: At. Mol. Opt. Phys.*, vol. 44, pp. 1969-1985, 1991.
- [142] T. Iwai and T. Asakura, "Speckle Reduction in Coherent Information Processing," *Proc. IEEE*, vol. 84, pp. 765-781, 1996.
- [143] L. Wang, T. Tschudi, T. Halldorsson, and P. Petursson, "Speckle reduction in laser projections with ultrasonic waves," *Opt. Eng.*, vol. 39, pp. 1659-1664, 2000.
- [144] A. L. Olsen and E. R. Washburn, "An Interpolation Table for Refractive Index-Normality Relationship for Solutions of Hydrochloric Acid and Sodium Hydroxide," *Transactions of the Kansas Academy of Science*, vol. 40, pp. 117-126, 1937.
- [145] D. R. Lide, *CRC Handbook of Chemistry and Physics*, 85th ed. Boca Raton, FL: CRC Press, 2006.
- [146] T. Hashimoto, Y. Nakasuga, Y. Yamada, H. Terui, M. Yanagisawa, Y. Akahori, Y. Tohmori, K. Kato, and Y. Suzuki, "Multichip Optical Hybrid Integration Technique with Planar Lightwave Circuit Platform," *J. Lightwave Technol.*, vol. 16, 1998.
- [147] C. A. Jones and K. Cooper, "Hybrid integration onto silicon motherboards with planar silica waveguides," *IEE Proc.: Optoelectron.*, vol. 143, 1996.

- [148] T. Joos and P. Fortina, *Microarrays in Clinical Diagnostics*. Totowa, NJ: Humana Press, 2005.
- [149] K. Takita, T. Aoki, Y. Sasaki, T. Higuchi, and K. Kobayashi, "High-Accuracy Subpixel Image Registration Based on Phase-Only Correlation," *IEICE Trans. Fundamentals*, vol. E86-A, 2003.